الجمهورية الجزائرية الديمقراطية الشعبية
People's Democratic Republic of Algeria
وزارة التعليم العالي و البحث العلمي
Ministry Of Higher Education & Scientific Research

Ibn Khaldoun University–Tiaret

Faculty of Applied Sciences

Department of Electrical Engineering

Ref :……

جامعة ابن خلدون تيارت
كلية العلوم التطبيقية
قسم الهندسة الكهربائية
المرجع:.....

A thesis submitted for the fulfillment of
the degree of

Doctorate in Electrical Engineering

Thesis has been prepared in the Electrical Engineering Laboratory of Tiaret L2GEGI

Application of intelligent control techniques for the control and the observation of an integrated PMSG in a wind system.

Presented by:

ASRI AICHA

The public thesis defense on: 28 November 2019

Board of Examiners:

M. LARBI	**Professor**	**Chairman**	**University of Tiaret**
S. HASSAINE	**Professor**	**Supervisor**	**University of Tiaret**
P. O. LOGERAIS	**Associate Professor**	**Co-Supervisor**	**University of Paris Est-Créteil**
M. SEBAA	**Associate Professor**	**Examiner**	**University of Tiaret**
B. SARI	**Associate professor**	**Examiner**	**University of Sétif**
Y. MIHOUB	**Associate professor**	**Invited**	**University of Tiaret**

Acknowledgements

This Ph.D. work was carried out in a cooperation between the laboratory of Energetic Engineering and Computer Engineering (L2GEGI) of the University Ibn Khaldoun-Tiaret, Algeria and the CERTES laboratory (Centre d'Études et de Recherche en Thermique, Environnement et Systèmes) of the University Paris-Est, Créteil, France.

First of all, I would like to thank God "Allah" the Most Gracious and the Most Merciful, for blessing me with knowledge and giving me strength, courage, patience, and serenity during all these years of study.

I would like to express my utmost gratitude and appreciation to my primary supervisor, Prof. Said HASSAINE, University of Ibn Khaldoun-Tiaret, Algeria for his guidance, support and encouragement throughout my Ph.D. studies. I am also grateful to my co-supervisors: Dr. Youcef MIHOUB, University Ibn Khaldoun-Tiaret, Algeria and Dr. Pierre Olivier LOGERAIS, University of Paris, Est Créteil, France for their comments and help on my research work.

Sincere thanks are also given to my Ph.D. committee members: Prof. M'hamed LARBI, Dr. Morsli SEBAA, University of Ibn Khaldoun-Tiaret, Algeria and Dr. Bilal SARI, University of Ferhat ABBAS-Sétif 1, Algeria for sparing their time to be my examiners.

Thanks to Prof. Tayeb ALLAOUI, Dr. Djilali TOUMI, University of Ibn Khaldoun-Tiaret, Algeria, Prof. Abdelmajid CHAOUI, University of Ferhat ABBAS-Sétif 1 and Mrs. Wilhelmina LOGERAIS, a native English speaker, for their useful help.

Last, but not least, I am grateful to my parents for their prayers, guidance, and support throughout my education. Their inspiration and encouragement have been invaluable.

Abstract

This research project deals with the development of advanced control strategies for a permanent magnet synchronous generator (PMSG) based Variable Speed Wind Turbine (VSWT). Two modes of operation have been considered: the isolated mode, and the grid-connected mode with battery energy storage. Conventional and fuzzy Maximum Power Point Tracking (MPPT) control strategies have been studied for the switch mode rectifier based standalone VSWT. A power management control strategy for a grid-connected system along with battery energy storage is developed. The main features are to catch the maximum power from the wind by generating an efficient duty cycle, ensure a constant DC-link voltage, maintain the amplitude and frequency of the grid, and balance the power flow within the system irrespective of fluctuating wind conditions and load demand. The developed control strategies have been validated via extensive computer simulations employing the Matlab Simpower Systems tool. The proposed Fuzzy Maximum Aerodynamic Power Tracking (FMAPT) control strategy has a higher overall control efficiency. The Fuzzy-PI (F-PI) controller gives more elevated output energy and presents a good transient performance and insensitivity to wind fluctuations and load variation than when considering the PI and Adaptive Fuzzy Logic Controller-PI (AFLC-PI).

Keywords: Battery storage, Fuzzy Logic Controller (FLC), Maximum Power Point Tracking (MPPT), Permanent Magnet Synchronous Generator (PMSG), Small Wind Energy Conversion System (SWECS).

Résumé

Ce projet de recherche porte sur le développement des stratégies de commandes avancées d'un système éolien à vitesse variable basé sur un générateur synchrone à aimants permanents (PMSG). Deux modes de fonctionnement ont été envisagés : le mode isolé et le mode connecté au réseau avec une batterie de stockage d'énergie. Des stratégies de contrôle conventionnelles et floues de suivi du point de puissance maximale (MPPT) ont été étudiée pour l'éolienne autonome à vitesse variable basée sur le redresseur en mode de commutation. Une stratégie de contrôle de la gestion de l'énergie pour un système connecté au réseau ainsi qu'un système de stockage d'énergie par batterie sont développés. Les principales caractéristiques consistent à capter le maximum de puissance du vent en générant un rapport cyclique efficace, maintenir la tension du bus continu constante, maintenir l'amplitude et la fréquence du réseau et équilibrer le flux de puissance du système, quelles que soient les conditions de vent et la demande de charge. Les stratégies de contrôle développées ont été validées par des simulations numériques utilisant l'outil Matlab Simpower Systems. La stratégie de contrôle de suivi du point de puissance aérodynamique maximale floue (FMAPT) proposée se caractérise par une efficacité de contrôle plus élevée. Le contrôleur Proportionnel Intégral Flou (F-PI) fournit une énergie de sortie plus élevée et présente de bonnes performances transitoires et une insensibilité aux fluctuations du vent et à la variation de la charge comparativement aux contrôleurs PI et flou adaptative (AFLC-PI).

Mots-clés: Batterie de stockage, Contrôleur logique floue (FLC), suivi du point de puissance maximale (MPPT), générateur synchrone à aimant permanent (PMSG), Chaine de conversion d'énergie éolienne petite (SWECS).

الملخص

يتناول هذا المشروع البحثي تطوير استراتيجيات تحكم متقدمة لمولد متزامن مغناطيسي دائم (PMSG) يعتمد على التوربينات الريحية المتغيرة السرعة (VSWT). تم اعتماد وضعين للعمل: الوضع المعزول والوضع المتصل بالشبكة مع بطارية تخزين الطاقة. تم تطوير استراتيجيات تحكم تقليدية وغامضة لتتبع نقطة الاستطاعة القصوى (MPPT) في الأنظمة الهوائية المعزولة (VSWT). تم تطوير إستراتيجية للتحكم في إدارة الطاقة لنظام متصل بالشبكة إلى جانب تخزين طاقة البطارية. تتمثل الميزات الرئيسية في الحصول على أقصى طاقة من الريح عن طريق توليد دورة عمل تتسم بالكفاءة، وضمان جهد ثابت لوصلة التيار المستمر، والحفاظ على سعة الشبكة وتواترها، وتحقيق التوازن بين تدفق الطاقة داخل النظام بغض النظر عن تقلب الرياح وتحميل الطلب. تم التحقق من صحة استراتيجيات التحكم المتقدمة من خلال محاكاة كمبيوتر واسعة باستخدام أداة Matlab Simpower Systems. تتميز إستراتيجية التحكم FMAPT المقترحة بكفاءة تحكم شاملة أعلى. توفر وحدة التحكم F-PI طاقة إخراج أعلى وتقدم أداءً عابراً جيدًا وعدم حساسية لتقلبات الرياح وتباين الحمل مقارنةً بالمتحكمين PI و AFLC-PI.

الكلمات المفتاحية: تخزين البطارية, المنطق الضبابي (FLC), خوارزميات تتبع نقطة الاستطاعة القصوى (MPPT), مولد تزامني ذو مغناطيس دائم (PMSG), نظام تحويل طاقة الرياح الصغير (SWECS).

Table of Contents

List of Figures

List of Tables

List of Abbreviations

AC	Alternative Current
AFLC	Adaptive Fuzzy Logic Controller
BESS	Battery Energy Storage System
CCM	Continuous-Current Mode
COA	Centroid of Area
ESS	Energy Storage System
DC	Direct Current
DCM	Discontinuous-Current Mode
DOC	Depth of Charge
DFIG	Doubly Fed induction generator
FLC	Fuzzy Logic Control
FMAPT	Fuzzy Maximum Aerodynamic Power Tracking
FMEPT	Fuzzy Maximum Electrical Power Tracking
F-PI	Fuzzy Proportional-Integral Controller
HAWT	Horizontal Axis Wind Turbines
HCS	Hill Climb Search
IGBT	Insulated Gate Bipolar Transistor
GSC	Grid Side Converter
MPPT	Maximum Power Point Tracking
ORB	Optimum Relation Based
OTC	Optimal Torque Control
P&O	Perturb and Observe
PCC	Point Common Coupling
PE	Power Electronic
PI	Proportional-Integral Controller
PID	Proportional Integral Derivative controller
PLL	Phase-Locked Loop
PMSG	Permanent Magnet Synchronous Generator
PSF	Power Signal Feedback
PWM	Pulse Width Modulation
SWECS	Small Wind Energy Conversion Systems
VAWT	Vertical Axis Wind Turbines

VOC	Voltage Oriented Control
VSI	Voltage Source Inverter
VSWT	Variable Speed Wind Turbine
WECS	Wind Energy Conversion System
WRSG	Wound Rotor Synchronous Generator
WPS	Wind Power System
WT	Wind Turbine
SCIG	Squirrel Cage Induction Generator
SOC	State of Charge
TSR	Tip Speed Ratio

List of Symbols

P_m	Turbine mechanical power
P_a	Aerodynamic power
P_{dc}	Electrical power
ρ	Air density
V_w	Wind speed
A	Swept area of wind turbine blade
C_p	Power coefficient
λ	Tip speed ratio
B	Pitch angle
R	Turbine rotor radius
Ω_m	Turbine rotating speed
$\omega_{e,}$	Electrical rotor angular speed
T_m	Mechanical torque
T_e	Electromagnetic torque
V_{sq}, V_{sd}	dq-axis stator terminal voltage
i_{sq}, i_{sd}	Currents in (d-q) reference frame
P	Number of poles pairs
R_s	Stator resistance
ϕ_{sd},ϕ_{sq}	dq-axis flux linkages
ϕ_m	Generator flux linkage
$L_{d,}L_q$	dq-axis inductances
T_m	Mechanical torque
T_e	Electrical torque
B_m	Damping coefficient
J_g	Generator inertia
J_{m}	Turbine inertia
D	Duty cycle
S	Switch pulse
V_i	Input voltage
V_{dc}	DC-link voltage
I_{dc}	DC current

P_g, Q_g	Active and reactive power
v_g	Grid phase voltage
i_g	Grid current
Φ_g	Grid power factor angle
E_0	Battery constant voltage
Q	Battery capacity
i_t	Actual battery charge
Q_e	Charge of the battery
C	Battery energy storage capacity
K_p, K_i	Proportional and Integral parameters
e	Standardized error
Δe	Normalized change in error
K_i	Variable normalization gain
Δu	Standardized crisp output

General Introduction

The increase in global energy demands, escalating energy prices, and growing environmental concerns with regard to conventional sources of energy based on fossil fuels have emphasized the need to move energy production to environmentally amiable energy sources. In the past few years, sustainable energy resources have led to high growth in global energy investments, especially wind power energy has been showing good promise as a sustainable development and source of energy. Wind power is the most competitive renewable energy.

According to preliminary statistics published in 2019 by the World Wind Energy Association (WWEA), since last year's global wind day, over 51 GW of both onshore and offshore wind turbine have been installed, bringing the global total capacity up to 591GW and making wind power a significant contributor to energy systems across the world. Today, 91 countries have installed wind energy, with over one third having more than 1 GW. In addition to established markets in Europe, China, and North America, emerging markets in Latin America and Asia will continue to drive growth in the upcoming years.

Wind energy can be used either directly as mechanical power or indirectly by converting the kinetic energy of wind into electrical energy. The most important part of any wind energy system is the wind turbine, which converts wind energy into mechanical power that can be utilized in various applications. Although wind turbine technology has been improving gradually, remarkable advances in the wind turbine design have been achieved. More specifically, modern technological developments and optimizations of a turbine and its components have demonstrated significant improvements in the generated power output and efficiency. Moreover, the developments of specific generators, along with the use of power electronic devices, have allowed gearless turbine designs.

A direct-driven wind power system based on Permanent Magnet Synchronous Generator (PMSG) is an attractive choice for small variable-speed wind generation systems due to its associated benefits. First, PMSG can provide high-reliability power generation since there is no need for external magnetization. Second, the high torque density of the PMSG allows a reduction in the cost of the system. Moreover, a wind turbine with a multi-polar PMSG removes the need for a gearbox. Thus, the system requires less servicing.

To realize a Maximum Power Point Tracking (MPPT) operation, a power electronic interface is necessary. The converter topology based on a three-phase diode rectifier cascaded with a boost converter is more suitable for Small Wind Energy Conversion System (SWECS) applications due to its low cost and high reliability. The control objective of the generator side converter is to extract the maximum available power via designed control methods. Several control structures, differing in complexity and cost, have been considered for SWECS. Developed control methods are proposed to provide maximum extracted energy at all conceivable wind speeds.

As the voltage and frequency of the generator output vary along with the wind speed change, an inverter is used to sustain the DC bus voltage and regulate the grid-side power factor. Thus, active and reactive powers are controlled by the grid-side converter.

With the rapid growth of wind energy development and increasing wind power penetration level, it will be a big challenge to operate the power system with high wind power penetration securely and reliably due to the inherent variability and uncertainty of wind power. With the flexible charging-discharging characteristics, Energy Storage System (ESS) is considered an effective tool to enhance the flexibility and controllability of the wind power system.

Problem statement

One top priority for controlling WECS is to extract the maximum available power from the incident wind for different wind speed values below the rated speed. Various MPPT algorithms have been applied to WECS. However, choosing an exact MPPT algorithm for a particular case requires sufficient proficiency because each algorithm has its own merits and demerits. For this reason, an appropriate review of those algorithms is essential. However, only a few attempts have been made in this concern. In this work, four available MPPT algorithms for extracting maximum power which are classified to conventional and fuzzy logic methods are described. Merits, demerits and comprehensive comparison of the different MPPT algorithms are also highlighted in the terms of complexity, wind speed requirement, prior training, speed responses, etc. and also regarding the ability to acquire the maximum energy output.

Since the PI control depends on the precise mathematical model, its performance becomes poor when there is disturbance of the system parameters or stochastic variations of

the wind speed. Moreover, the setting of the parameters for the controller is difficult since an accurate mathematical model is usually hard to obtain. It should be noted that a complex system is often composed of characteristics non-linear, large time lag, uncertainty, and time-variance characteristics. In this case, it is impossible to obtain a precise mathematical model. A variety of advanced control methods such as the fuzzy logic one have recently been applied in response to wind energy conversion problems, and thereupon has been implemented to solve some of these issues.

The renewable energy source such as wind energy cannot operate satisfactorily at the desired voltage and frequency under the fluctuating load demand due to its intermittent nature. Some additional sources are required in order to counterbalance the fluctuating nature of the wind. With the rapid development of renewable energies and power electronic technologies and with cost reduction of energy storage systems, different control strategies and power management systems have been proposed for wind integration. The battery is one of the more commonly used energy storage to counterbalance the intermittent nature of the wind source.

Objectives of thesis

The primary objectives of this research are to develop different control strategies for a WECS under two operating modes: standalone and grid-connected system in order to maintain stable and reliable operation of this system.

In another words, the aims will be:

- To design and develop a simple and cost-effective simulation model to evaluate the developed control strategies for a power management scheme. The system structure includes the wind turbine, a direct driven permanent magnet synchronous generator (PMSG) and an uncontrolled rectifier followed by a DC/DC boost converter,
- Two conventional MPPT algorithms have been considered to operate the standalone WECS at the maximum power. Furthermore, a comparative study of the corresponding control strategies and architectures is proposed regarding the tradeoffs between structural complexity and energy efficiency,
- Development of an advanced MPPT control schemes based on fuzzy logic for the standalone WECS to ensure a high level operating of the system and a maximum power extraction from the wind,

- Elaboration of an overall dynamic mathematical model connected to the grid using the fuzzy MAPT control scheme,
- To design a control strategy with a Fuzzy Logic Controller (FLC) to regulate the DC-link voltage. It is supposed to improve the dynamic performance compared with the classical PI controller, To maintain the amplitude and frequency of the grid, and to balance the power flow between the generator and the grid to meet the load demand,
- To develop a power management control strategy for a wind power system along with battery energy storage as a hybrid system. Balancing the power flow irrespective of fluctuating wind conditions and variable load demand will be focused on.

Thesis outline

The research presented in this thesis is structured in four chapters. The work carried out in each chapter is summarized as follows:

Chapter 1 provides a market survey and an overview of wind turbine technology, wind energy system classifications, power electronic converters, and wind energy storage system. Moreover, a state of the art of MPPT control strategies for WECS is presented.

Chapter 2 is dedicated to the detailed analysis and modeling of the standalone WECS including wind turbine, PMSG, which is directly driven by the wind turbine without using a gearbox, a switch-mode rectifier that consists of a three-phase diode bridge rectifier and a DC-DC boost converter. Finally, a comparative control study of the switch-mode rectifier between two conventional MPPT algorithms for a maximum power tracking strategy is provided. The proposed control scheme is simulated in ***Matlab/SimPowerSystems*** environment prior to disclose and discuss simulation results.

In chapter 3, a brief history of the fuzzy set theory and its application areas are summarized. FLC, development of the rules, the way of putting experts' ideas into rules and the inference system structure are studied. From crisp input variables to crisp output, all processes are discussed and shown. Defuzzification, rule processing, fuzzy reasoning and crisp output after defuzzification are explained. Then, a comparative control study between two fuzzy maximum power tracking strategies for the switch-mode DC-DC boost converter is realized.

Chapter 4 presents the system integrating a PMSG based Wind Power System (WPS) connected to the grid and a Battery as Energy Storage System (BESS). The mathematical

model and analysis of the Grid Side Converter (GSC) and BESS are detailed. Fuzzy logic control based DC-link voltage is implemented for the grid side converter. Then the control of the power flow between the generator, the battery and the grid to meet the load demand is presented in this chapter. Extensive simulation results have been performed using MATLAB/Simpower system.

Chapter 1. Literature review of wind energy conversion systems and control techniques for maximum power extraction

1.1 Introduction

Over the last twenty years, renewable energy sources have been attracting great attention due to the cost increase, limited reserves, and adverse environmental impact of fossil fuels. In the meantime, technological advancements, cost reduction, and governmental incentives have made some renewable energy sources more competitive in the market. Among them, wind energy is one of the fastest-growing renewable energy source [1].

The development of wind energy conversion technology has been going on since the 1970s and the rapid development has been seen from the 1990s [2], especially in the last decade, stimulated by the high growth rate in the wind energy market. Hence, various new wind energy conversion technologies have been emerging, aiming at reducing cost, and enhancing both efficiency and reliability. The size of wind turbines has increased from a few kilowatts to several megawatts for each of them.

In recent years, wind conversion technology has showen new aspects on its construction and operation. The latest generation of Wind Turbines (WTs) operates at variable speed without speed multiplier. This type of operation can increase energy efficiency, reduce mechanical stress and improve the quality of electrical and mechanical produced energy [3].

For Variable Speed Wind Turbines (VSWTs), PMSGs are the most used technologies due to their simple structure with self-excitation characteristic that can work with a high power factor, high reliability, good performance control, and a great capacity for maximizing the power extracting by the MPPT [4, 5].

To realize the MPPT operation, a power electronic interface is necessary. The converter topology based on a three-phase diode rectifier cascaded with a boost converter is more suitable for SWECS applications due to its low cost and high reliability [6].

Integration of energy storage devices in wind turbines applications aims to answer the following problematic: the excess energy storage of the production compared to demand and the supply of energy for the shortfall because of the intermittent behavior of the wind [7].

This chapter provides an overview of the WECS and of their related technologies. The chapter aims at displaying background on several aspects related to this exciting technology and market trends such as the installed capacity and the growth rate. The details of turbine components, system configurations are presented. It reviews the operating principle of various MPPT algorithms for WECS and discusses their merits and demerits.

1.2 Installed capacity and growth rate

Over the last decades, wind power has reached a significant level in electrical power production. Figure 1.1 shows the evolution of the cumulative installed capacity worldwide as of 2013 [8]. According to preliminary statistics published by the World Wind Energy Association (WWEA), more than 50 GW of the wind power capacity was added to the global wind generation capacity which becames 579 GW in 2018. It is slightly less than in 2017 when 52 GW were installed. 2018 was the second year in a row with a growing number of new installations but at a lower rate of 9.1%, after 10.8% growth in 2017. This growth has been spurred by the continuous cost increase of classic energy sources, cost reduction of wind turbines, governmental incentive programs and public demand for cleaner energy sources. All wind turbines installed by the end of 2018 can cover close to 6% of the global electricity demand.

Figure 1.2 shows the cumulative installed wind power capacity of the top 9 countries in the world as of 2018 [8]. During this year, China has maintained its role as the largest wind power producer. Its installed capacity in 2018 grew to more than 200 GW, equivalent to 34% of the global installed capacity, and is expected to continue to grow at a fast pace in the next few years. Together with an amazing deployment in solar power, the country is now well on its way of making renewable energy its main energy source.

Out of the leading markets, China and the United States saw an increased growth, with over 16% and 10% of the total installed wind power capacity respectively, whereas in Germany and India, this ratio is only 6% and 3% respectively.

1.3 Small and large wind turbines

Over the past few decades, the capacities of WT units have increased from a few tens of kW power capacity to today's multi-MW level. Wind turbines are generally divided into two broad categories based on their rated capacities and their intended applications [9]. Small-to-medium-size wind turbines are those that have their rotor diameters ranging from 3 m to 30 m

and having a power capacity below 300 kW. Figure 1.3 demonstrates the classification of wind turbines based on power rating [10]. Small scale wind turbines can be installed at homes, farms, and businesses to offset the consumption of utility power. Small wind power units can be used in combination with other energy sources such as photovoltaic power and diesel generators to form a standalone/off-grid generation system for remote areas, where access to the power grid is difficult or costly [11].

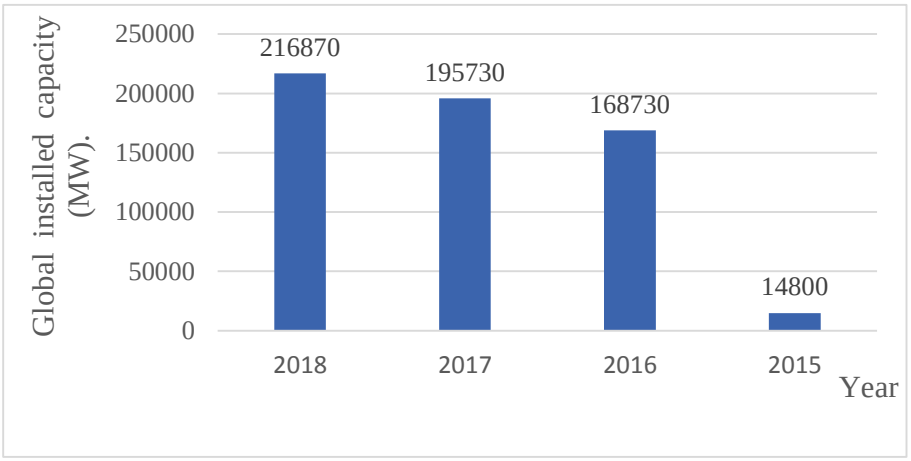

Figure 1. 1. Global annual and cumulative installed wind power capacity (2015-2018).

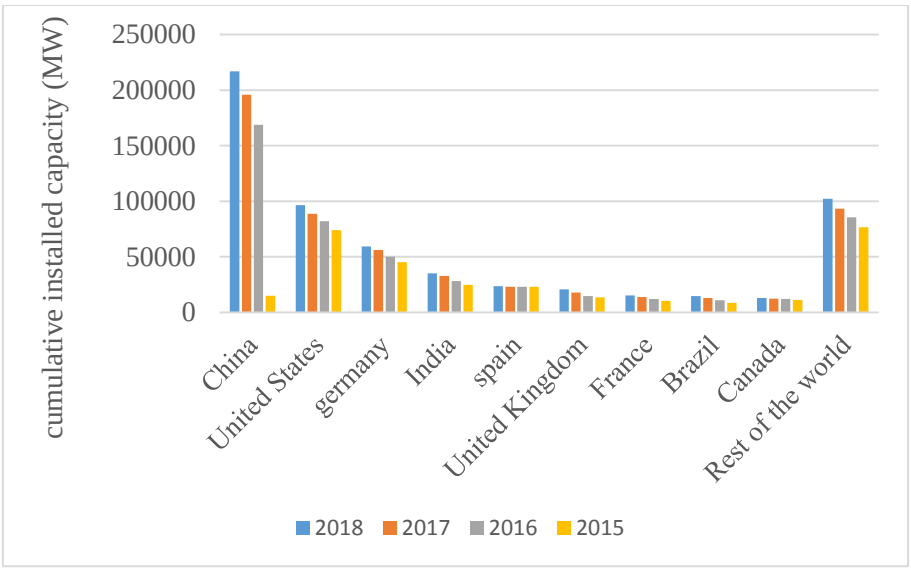

Figure 1. 2. Top 9 countries in cumulative installed wind power capacity as of 2018.

On the other hand, the size of large wind turbines has steadily increased over the years. The evolution in the turbine size can be appreciated in Figure 1.3. Starting with a 50 kW power rating and a 15 m rotor radius in the early 1980s, wind turbines can be found today up

to 10 MW with a rotor diameter of 190 m [10]. The increase in wind turbine size implies more power output since the energy captured is a function of the square of the rotor radius. Larger wind turbines often result in reduced cost since their production, installation, and maintenance costs are lower than the sum of smaller wind turbines achieving the same power output.

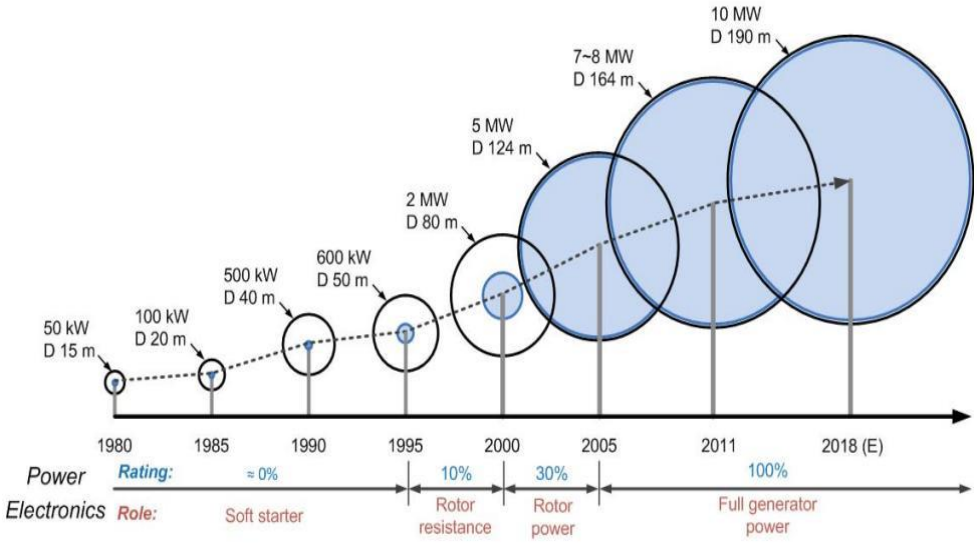

Figure 1. 3. Classification of wind turbines based on the rotor diameter.

1.4 Standalone and grid-connected applications

The wind turbines can operate as standalone units of small power capacities to power villages, farms, and islands where access to the utility grid is remote or costly [12]. Since the stochastic nature of wind and fluctuating loads make the operation of wind power system more challenging than in a grid-connected application, other energy sources are normally required in standalone systems. The integration of energy storage systems, diesel generators, or photovoltaic energy systems with the standalone operation of a wind power system improves the voltage and frequency responses in the presence of fluctuating wind speed and varying load demand [13]. Due to its limited applications, standalone wind power constitutes only a small fraction of the total installed wind capacity in the world. The majority of wind turbines operating in the field are grid-connected, and the power generated is directly uploaded to the grid.

1.5 Wind turbine classification

The wind turbine is one of the most important elements in WECSs. Over the years, different types of wind turbines have been developed [12]. This section provides an overview

of wind turbine technologies, including horizontal/vertical-axis turbines and fixed/variable-speed turbines.

1.5.1 Horizontal-axis and vertical-axis wind turbines

When considering the configuration of the rotating axis of rotor blades, modern wind turbines can be classified into horizontal-axis (HAWT), and vertical-axis turbines (VAWT), as shown in Figure 1.4.

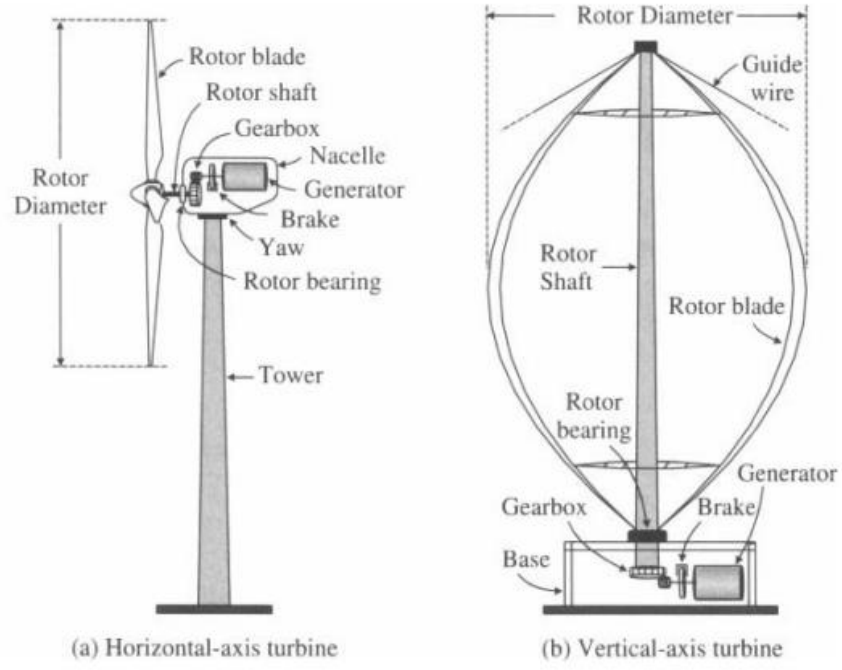

Figure 1. 4. Horizontal- and vertical-axis wind turbines.

Most commercial wind turbines are today horizontal-axis type, in which the rotating axis of the blades is parallel to the wind stream. The tower elevates the nacelle to provide sufficient space for the rotor blade rotation and to reach better wind conditions. The nacelle supports the rotor hub that holds the rotor blades and also houses the gearbox, the generator and, in some designs, the power converters. The industry standard HAWT uses a three-blade rotor positioned in front of the nacelle, which is known as upwind configuration. However, downwind configurations with the blades at the back can also be found in practical applications. Turbines with one, two, or more than three blades can also be seen in wind farms [14].

In vertical-axis wind turbines, the orientation of the spin axis is perpendicular to the ground. The turbine rotor uses curved vertically mounted airfoils. The generator and gearbox

are normally placed in the base of the turbine on the ground, as depicted in Figure 1.4 (b). The rotor blades of the VAWT have a variety of designs with different shapes and numbers of blades. The design given in the figure 1.4 (a) is one of the popular design [15].
A comparison between them is summarized in Table 1.1 [16, 17].

The conversion of wind energy to electrical energy involves primarily two stages: in the first stage, kinetic energy in wind is converted into mechanical energy to drive the shaft of a wind generator. The critical converting devices in this stage are wind blades. For maximizing the capture of wind energy, wind blades need to be carefully designed.

Table 1. 1. Comparison between horizontal- and vertical-axis wind turbines.

Turbine type	Advantages	Disadvantages
HAWT	• Higher wind energy conversion efficiency, • Access to stronger wind due to high a tower, • Power regulation by stall and pitch angle control at high wind speeds.	• Higher installation cost, stronger tower to support the heavy weight of nacelle, • Longer cable from the top of the tower to ground, • Orientation required (yaw control).
VAWT	• Lower installation cost and easier maintenance due to the ground-level gearbox and generator, • Operation independent of wind direction, • Suitable for rooftops (stronger wind without need of tower).	• Lower wind energy conversion efficiency, • Higher torque fluctuations and prone to mechanical vibrations, • Limited options for power regulation at high wind speeds.

The power coefficient C_p deals with the converting efficiency in the first stage, defined as the ratio of the captured mechanical power by blades to the available power in wind:

$$C_p(\lambda,\beta) = \frac{P_m}{\frac{1}{2}\rho A v_w^3} \tag{1.1}$$

The air density ρ is a function of the air pressure and air temperature. At sea level and temperature of 15°C, air has a density of approximately 1.2 kg/m^3, A is the swept area in m^2 ($A=\pi r^2$, with r is the radius of blades in m), v_w is the wind speed in m/s.

C_p has a theoretical maximum value of 0.59 according to the Betz limit [18]. Because there are various aerodynamic losses in wind turbine systems, for instance, blade-tip, blade-root, profile, and wake rotation losses, etc., the real power coefficient C_p is much lower than its theoretical limit, usually ranging from 30 to 45% [16]. Figure 1.5 shows a typical C_p-λ curve for the different types of rotors. We can observe that for each type of turbine, there is an optimal tip-speed ratio λ_{opt} for which the power coefficient is maximum. These curves show the advantage of horizontal turbines with low number of blades in terms of power capture. The three-blade rotors are currently predominant in all modern wind energy systems [17].

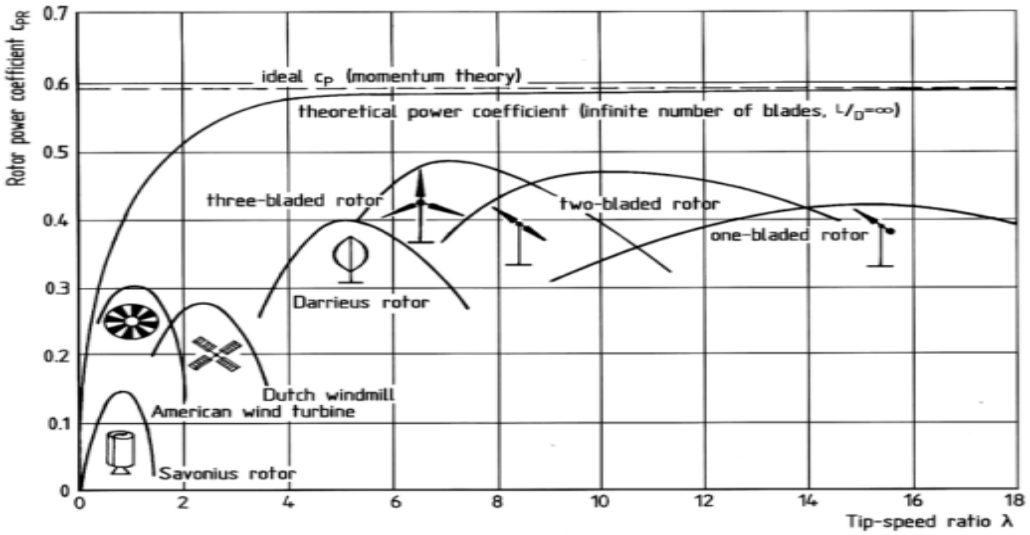

Figure 1. 5. Typical power coefficients of different rotor types over tip-speed ratio.

1.5.2 Fixed-and variable-speed turbines

Wind turbines can also be classified into fixed-speed and variable-speed turbines [19]. As the name suggests, fixed-speed wind turbines rotate at almost a constant speed, which is determined by the gear ratio, the grid frequency and the number of poles of the generator. In general, fixed-speed wind turbines are equipped with a Squirrel Cage Induction Generator (SCIG), that is directly connected to the grid without any power electronic converter [20]. They are designed to achieve maximum efficiency at one particular wind speed, and the system efficiency degrades at other wind speeds. The fixed speed wind turbine features are simple, robust, reliable, and well-proven. Moreover, the cost of its electrical parts is low. Its disadvantages are an uncontrollable reactive power consumption, mechanical stress and limited power quality control. Owing to its fixed-speed operation, all fluctuations in the wind speed are further transmitted as fluctuations in the mechanical torque and then as fluctuations

in the electrical power on the grid. In the case of weak grids, the power fluctuations can also lead to large voltage fluctuations, which, in turn, will result in significant line losses [12].

On the other hand, variable-speed wind turbines are designed to achieve maximum aerodynamic efficiency over a wide range of wind speeds. The turbine can continuously adapt its rotational speed according to the wind speed. In doing so, the tip speed ratio is kept constant at a predefined value that corresponds to the maximum power coefficient [21]. To make the turbine speed adjustable, the wind turbine generator is normally connected to the utility grid through a power converter system [22]. The power converter controls the generator speed; that is, the power fluctuations caused by wind variations are absorbed mainly by changes in the rotor generator speed and, consequently, in the wind turbine rotor speed. The advantages of VSWTs are an increased energy capture, improved power quality and reduced mechanical stress on the wind turbine. The disadvantages are losses in power electronics, the use of more components and the increased of the cost of their equipment.

The introduction of VSWT types increases the number of applicable generator types and also introduces several degrees of freedom in the combination of generator type and power converter type. The variable speed wind turbines can be divided into [23]:

- direct-drive (gearless)
- indirect-drive turbines.

In a gearless direct drive wind turbine, low-speed synchronous generators with a higher number of poles are used. The number of poles of synchronous generators is chosen to match the turbine speed without any gearbox. Both Wound Rotor Synchronous Generator (WRSG) and PMSGs are suitable for the direct-drive turbines [1]. A review of generator systems for direct-drive WT applications is presented in [24].

Therefore, indirect drive VSWT based on DFIGs with partial scale power electronic interfaces or PMSGs with full-scale power electronics interfaces, are popular among others. The DFIG based VSWT system requires a multi-stage gearbox and also needs an excitation current [23]. Different from the DFIG based wind energy systems, those based on PMSGs with full scale power electronic interfaces are becoming more popular due to the number of advantages such as high energy density, simple control methodology, low maintenance cost, self excitation system and possibility to direct coupling to a WT with elimination of the gearbox; except initial installation costs [25]. Furthermore, other features such as complete

decoupling from the grid, full controllability of the system for maximum wind power extraction, high performance, high efficiency, high precision, high reliability, wide operating range and improved capability make wind energy systems based on PMSGs even more attractive; though power converter losses increase [26, 27]. The advantages and disadvantages of different VSWT generators are outlined in [26].

1.6 Power electronic converter topologies

Many industrial applications of PMSG require a wide variable speed range. A standard VSWT concept requires a power electronic system that is capable of adjusting the generator frequency and voltage to the grid. Several types of power electronic interfaces are presented in the diverse works of the literatures for direct-driven variable speed PMSG based wind energy systems [28, 29]. We can distinguish three configurations of AC/DC power electronic converters, the most commonly used ones with the PMSG [30].

Figure 1.6 shows a direct-driven variable speed PMSG with front end uncontrolled diode rectifier. The three-phase diode rectifiers convert the AC voltage to a DC voltage and the Voltage Source Inverter (VSI) converts the DC voltage to AC voltage at the required magnitude and frequency. The DC-link capacitor is a very important component of the drive topology. It is connected between the supply side diode rectifier and the grid side VSI. The capacitor serves as a filter to remove voltage ripples due to the pulsating DC voltage and act as a temporary energy storage or voltage source to the three-phase VSI. This topology is simple and cost-effective; it requires only one controller for the VSI. However, it is less attractive due to the need for means to manage energy efficiency [31].

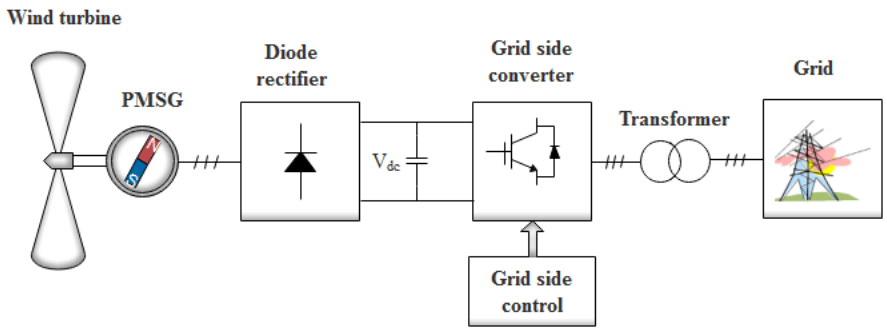

Figure 1. 6. PMSG drive with front end uncontrolled diode rectifier and VSI.

The Full-Scale Back-Back Voltage Source Converter (VSC) topology is widely used for wind energy systems. In this concept, two-level three-phase AC/DC and DC/AC converters

are connected back-to-back between the variable speed PMSG and the grid. Figure 1.7 shows such a system in which the PMSG is connected to the grid via a full-scale back-back converter system. This topology is much preferred since the power converters fully decouple the wind turbine from the grid disturbances and can be caring in some sort of grid support. The full-scale power converter offers the merits of high reliability and good power quality [26]. A full-scale power converter configuration may avoid the bulky grid-side transformer, thereby, reduces the weight and volume of the nacelle [32]. The performance of the wind energy system can be enhanced by PWM control strategies. By using the PWM technique, the low-frequency harmonics are eliminated and the frequency of the first higher-order harmonics lies at about the switching frequency of the inverter or rectifier [33]. However, this structure is more expensive since it requires the implementation of six switches controlled by six PWM signals [34].

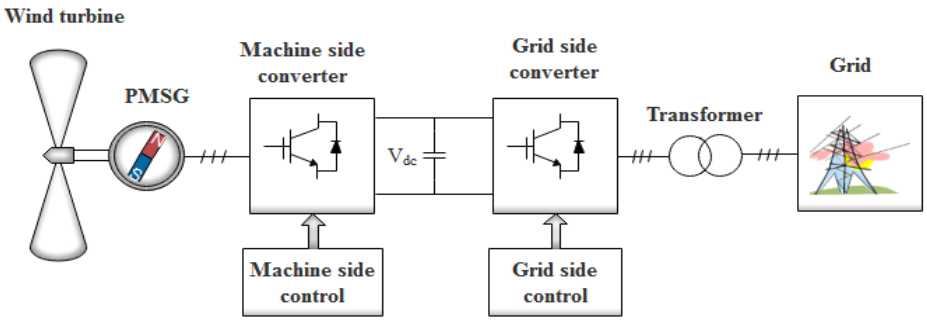

Figure 1. 7. Variable-speed configurations with full-scale converters.

A three-phase diode bridge rectifier cascaded by DC-DC converter is displayed in Figure 1. 8. Since the diode rectifier is an uncontrolled converter, a DC-DC converter is used to control the PMSG speed and achieve maximum power point tracking (MPPT). Between the front-end diode bridge rectifier and the DC-DC converter there is a capacitor whose the role is to reduce the voltage ripple, to provide storage and to isolate the generator side from the grid. In this topology, the generator voltage output is converted into DC voltage using the diode bridge rectifier, and the grid side VSI converts the DC voltage into a constant voltage and frequency. There are two control strategies in this configuration, the DC-DC converter controller and the DC/AC inverter controller.

This topology has attractive features like the decrease in the number of switching devices, and can thereby permit to diminish the size and the cost of the power conversion system in comparison with the PWM converter scheme [35, 36]. One problem with using a

diode rectifier as the generator-side converter is the resulting distortion in the stator current waveforms, leading to higher losses and torque ripples in the generator. Despite this disadvantage, this topology is the most suitable for the low-power wind system. We have retained this topology in our work.

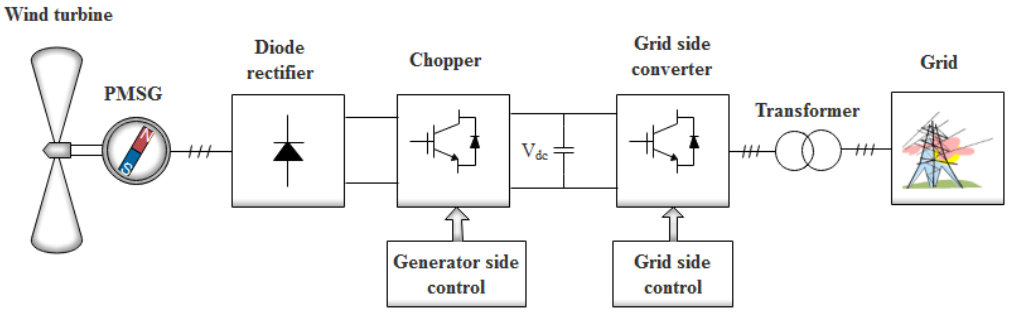

Figure 1. 8. PMSG drive with front end uncontrolled diode rectifier and DC-DC converter and VSI.

1.7 Energy storage system

Energy based on electricity generated from renewable sources such as wind source offers enormous potential for meeting continuous energy demands. However, the use of electricity generated from these intermittent, renewable sources requires efficient electrical energy storage. The presence of energy storage systems is critical for ensuring a high level of power quality [37]. Various storage technologies, including flywheel energy storage (FES) [38, 39], BESS [40, 41], advanced capacitor [42], and Superconducting Magnetic Energy Storage (SMES) [43, 44], are proposed in the literature for wind applications. In this thesis, a wind energy system is combined with battery energy storage to form a hybrid system which operates on a grid-connected mode. Battery storage is one of the best-suited storage technologies for wind power applications, due to its high energy density levels and flexibility, making it easy to integrate. The typical structure of hybrid wind and battery energy storage is shown in Figure 1.9.

The wind energy source is connected to the grid through a series of power electronic interfacing units or converters. Similarly, battery energy storage is also connected to a DC link through a DC-DC converter to match the voltage level with a separate controller. The main objective of the battery energy storage is to counteract the effect of the stochastic nature of the wind energy source.

There are varieties of different battery chemistries that can be used for utility energy storage. The lead-acid batteries are the oldest and the most commonly used ones all over the

world, and account for 75% of renewable energy market owing to their high availability and cost-effective solution, which can be adapted for different types of energy storage applications [45-47]. Lead-acid batteries have been successfully applied for small wind power applications. They have been investigated for the stabilization of grid-connected wind turbines [48]. Lead-acid batteries have an energy efficiency of between 80%-90%. There are two types of lead–acid batteries. They may be flooded (FLA) or sealed valve-regulated (VRLA) types [49].

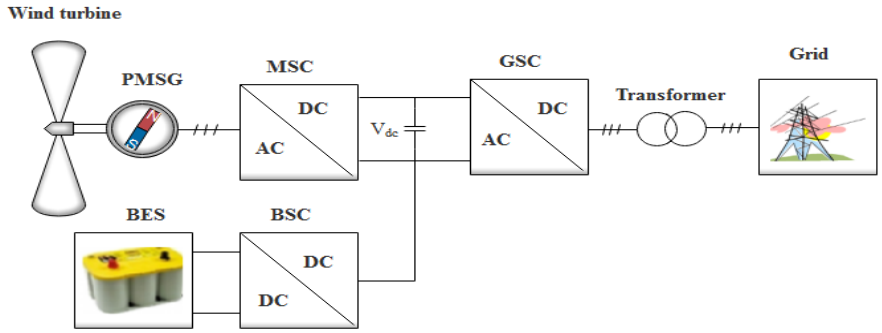

Figure 1. 9. Wind-BESS based hybrid system.

The VRLA in the market attracts more renewable energy owners [37]. The VRLA cells require minimal maintenance than flooded lead-acid (FLA), and much lower electrolyte content [50]. This means the shipping and airfreight regulations and the battery rooms are dramatically simplified, which, in turn, reduces the life cycle costs. However, lower electrolyte content is prone to dry out failures more than the conventional one; however, this can be tackled through the battery management system by using temperature-controlled voltage [51].

1.8 State-of-the-art of MPPT control strategies for WECS

The control of a variable-speed wind turbine below the rated wind speed is achieved by controlling the generator. The main goal of using a MPPT algorithm is to operate the WECS around the maximum power for any variations of the wind speed. The MPPT algorithms researche during the last few decades can be classified into different control methods [52-55], namely Tip Speed Ratio (TSR) control, Optimal Torque Control (OTC), Power Signal Feedback (PSF) control, Hill-Climb Search (HCS) control and FLC. This section reviews and studies the state-of-the-art of available MPPT algorithms.

1.8.1 Optimal tip speed ratio (TSR)

In this method, the maximum power operation of the wind turbine is achieved by keeping the tip speed ratio to its optimal value λ_{opt} despite wind variations. The principle of this control scheme is shown in Figure 1.10 where the measured wind speed v_w is used to get the optimal turbine speed Ω_{m_opt} according to the optimal tip speed ratio (λ_{opt}). The generator speed is controlled by the power converters and will be equal to its reference in steady-state, at which the MPPT is achieved.

$$\Omega_{m\_opt} = \frac{\lambda_{opt} v_w}{R} \tag{1.2}$$

where, λ_{opt} is the optimal tip speed ratio, R is the radius of the turbine, and v_w is the wind speed.

The wind speed needs to be measured by an accurate anemometer which renders the system more costly, particularly for small scale WECS [56] where the accurate value is almost impossibly obtained in practice. Besides, the wind turbine characteristic, which varies from system to system, is also indispensable. Therefore, the optimum TSR-MPPT method is rarely applied in the actual WECSs though the control strategy is very simple and highly efficient [57].

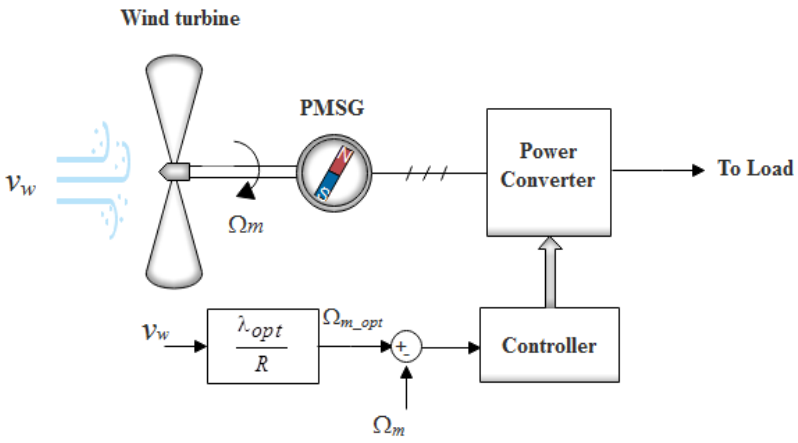

Figure 1. 10. Tip speed ratio control of WECS.

In the literature, some authors [58-60] have suggested the use of the Neural Networks (NN) to estimate the wind speed in order to avoid using anemometers, and further, using the estimated wind speed and knowledge of optimal TSR, the optimal rotor speed can be accurately determined. Nevertheless, the use of such an estimator increases the complexity of

the implementation of the algorithm. The block diagram of the NN-based MPPT controller module is shown in Figure 1.11. The inputs to the NN are the rotor speed ω_m and the mechanical power P_m.

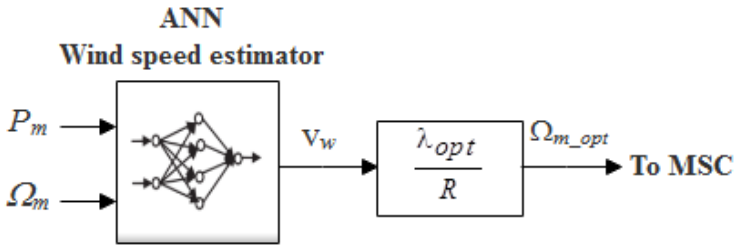

Figure 1. 11. NN-based MPPT control module of turbine rotor speed.

1.8.2 Optimal Torque (OT) control

The maximum power of the wind turbine can also be achieved with the Optimal Torque Control (OTC) algorithm according to equation (1.3), where the optimal mechanical torque of the turbine T_{m_opt} is a quadratic function of the turbine speed Ω_m.

$$T_{m\_opt} = \frac{1}{2}\rho\pi R^5 \frac{C_{p\_\max}}{\lambda_{opt}^3}\Omega_m^2 = K_{opt}\Omega_m^2 \tag{1.3}$$

where ρ is the air density, R is the radius of the turbine, C_{p_max} is the maximum power coefficient of the rotor, λ_{opt} is the optimal tip speed and Ω_m is the wind rotor angular velocity.

Figure 1.12 shows the principle of the MPPT scheme with OTC, where the turbine speed Ω_m is measured and used to compute the OT (T_{m_opt}). The coefficient for the OT (k_{opt}) can be calculated according to the rated parameters of the generator λ_{opt} and C_{p_max}. Through the feedback control, the turbine torque T_m will be equal to its reference T_{m_opt} in steady-state, and this is how the MPPT is realized. It is noted that there is no need to use wind speed sensors in this scheme.

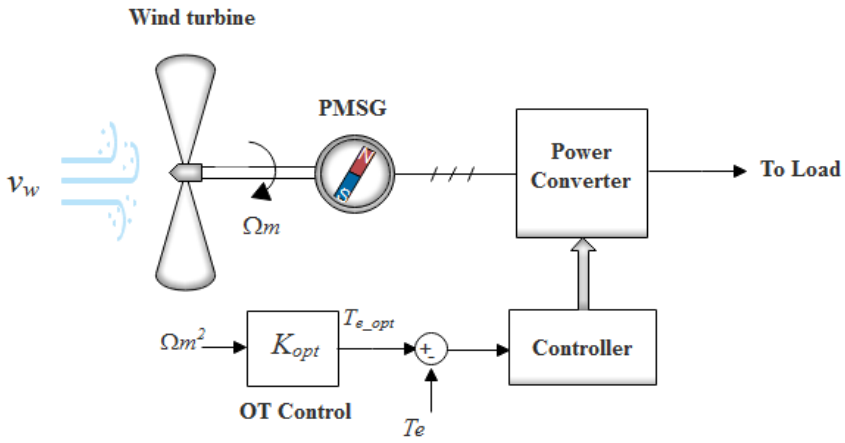

Figure 1. 12. MPPT with optimal torque control of wind turbines.

In general, this method is simple, fast, and efficient [57, 61]. However, its efficiency is lower compared to that of the TSR control method, because it does not measure the wind speed directly, meaning that wind changes are not reflected instantaneously and significantly on the reference signal [6].

1.8.3 Power Signal Feedback (PSF) control

In the PSF control, the MPPT is based on the power versus the turbine speed curve. It is required to have the knowledge of maximum power curve of the wind turbine, and track this curve through its control mechanisms. The maximum power curves need to be obtained via simulations or real-time on individual wind turbines. A simplified control block diagram of a WECS with PSF control for Maximum Power Extraction (MPE) is illustrated in Figure 1.13.

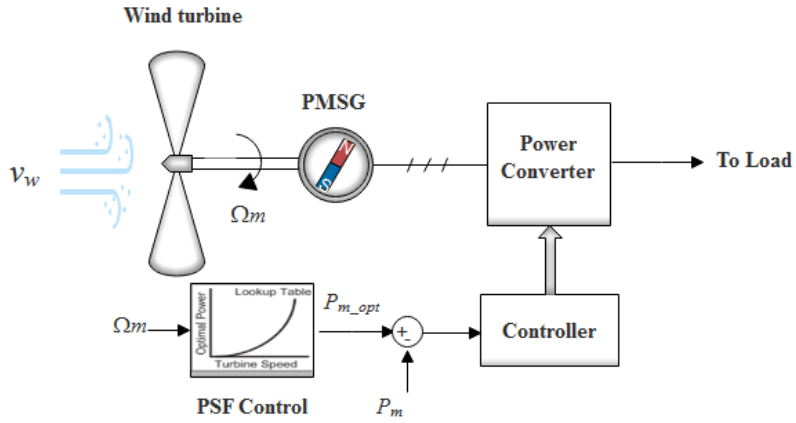

Figure 1. 13. PSF control.

The PSF control block generates the reference power command P_{m_opt} either using a recorded maximum power curve (Figure 1.14) [55, 62], or using the mechanical power equation of the wind turbine (equation 1.4) where wind speed or the rotor speed is used as the input. By maintaining the mechanical power P_m of the generator at its optimum value, the maximum energy conversion efficiency is achieved.

$$P_m = \frac{1}{2} C_p \rho A v_w^3 = k_{opt} \omega_{m\_opt}^3 \tag{1.4}$$

where C_p is the power coefficient of the rotor, ρ is the air density, A is the swept area, and Ω_{m_opt} is the optima wind rotor angular velocity.

According to [63], there is no difference between the PSF and the OT methods in terms of performance and complexity of implementation.

Numerous optimum relationships have been presented in the literature, which are all suitable for MPPT control. The authors [64] have expressed the optimal DC voltage as a function of the DC output power with one coefficient. The DC-voltage versus DC-current optimum relationship was calculated analytically based on the system parameters in [65]. In [66], an optimum relation between the DC-voltage and the DC-current was used to track the Maximum Power Point (MPP). The authors of [67] further simplify this relationship to a linear equation between the DC-current and the square of the DC-voltage.

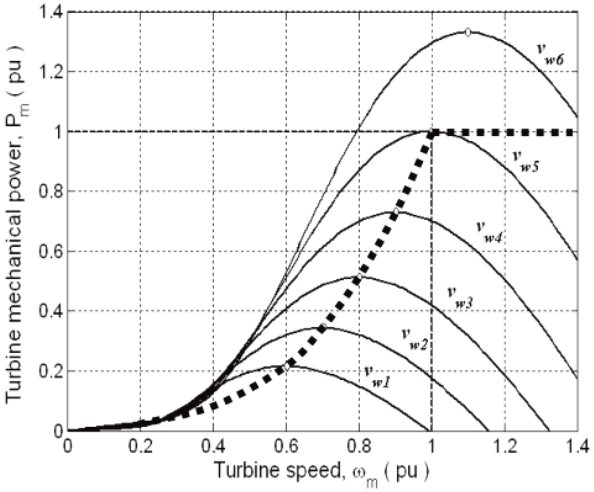

Figure 1. 14. Characteristics of turbine power versus turbine speed for various wind speeds.

1.8.4 Hill Climb Search (HCS)/Perturb & Observe (P&O) control

The HCS control algorithm is a mathematical optimization strategy which continuously searches for the peak power of the wind turbine. It can overcome some of the common

problems normally associated with the TSR and PSF methods. The MPPT can be achieved without any knowledge of the characteristics of the wind energy system. Therefore, the HCS seems to be the top choice for MPPT control in the WECSs due to this feature. The tracking algorithm, depending upon the location of the operating point and relation between the changes in power and speed, computes the desired optimum signal in order to drive the system to the point of maximum power. Figure 1.15 illustrates the principle of HCS control and Figure 1.16 shows a WECS with HCS controller for tracking maximum power point.

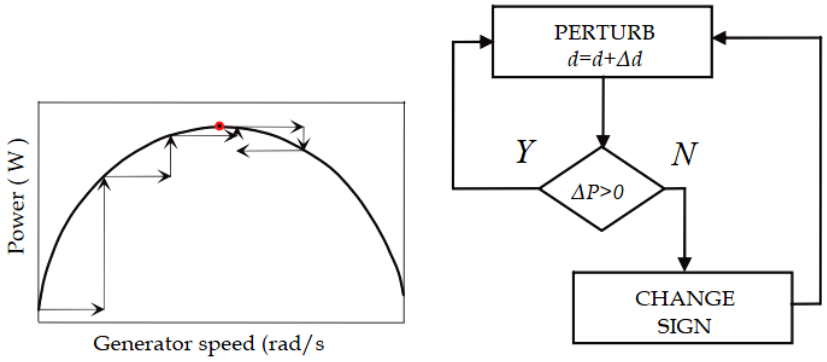

Figure 1. 15. HCS Control Principle.

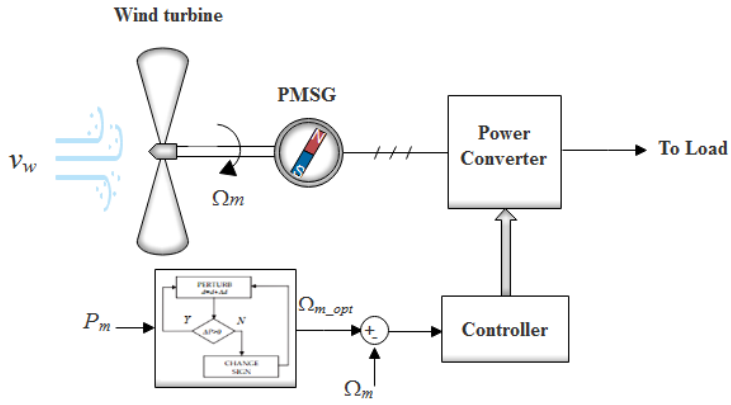

Figure 1. 16. WECS with HCS control.

Although this method is very simple and does not need any knowledge of system parameters, it suffers from some limitations. The efficiency/rapidity trade-off such as a large step size results in a rapid tracking of MPP but inevitable oscillations occur around it. Hence, the efficiency of the system is low, whereas, a smaller step size boosts the system efficiency but reduces the speed of convergence. Further, a highly fluctuating wind speed condition always results in the MPP search in the wrong direction [63].

The authors of [53] review the most proposed MPPT methods and conclude that the Perturb & Observe (P&O) method has not satisfactory performance under fluctuating wind speed.

Aiming to improve the efficiency and rapidity trade-off of the conventional P&O method, several researchers propose replacing the fixed step-size with a variable step-size. The perturbing step size is obtained using the power slope with respect to the control variable. Thus, if the system is working far from the optimal point, due to the large value of the slope, a large step-size is applied, while a small step-size is imposed for an operating point close to the MPP.

The papers [68–72] proposed numerous P&O methods which permit a high dynamic in the tracking of the MPP with fewer oscillations in the steady-state. Nevertheless, the problem of the divergence from the MPP under rapid wind speed variations was not resolved by these techniques, and the system might still fail to track the MPP under these conditions.

A new P&O control is proposed in [73] for SWECSs to accomplish a fast-tracking of the MPP under a rapidly changing of the wind speed in which the proposed algorithm does not require either knowledge of the system parameters or of the mechanical sensors. Nevertheless, the stochastic nature of wind and fluctuating loads make the operation of WPS more challenging than in a grid connected application.

1.8.5 Fuzzy Logic (FL) control

FLC systems provide a much-improved performance to operate the wind system under MPP in fast-changing environmental conditions and uncertainties [74]. The core interest of FLCs is their ability to incorporate experience, intuition, and heuristics into the system instead of relying on mathematical models, making them more effective in power system applications where existing models are ill-defined and not reliable enough [75]. The block diagram of WECS with FL based control strategy is shown in Figure 1.17. The design process for a FLC consists of:

- Determining the inputs,
- Setting up the rules,
- Designing a method to convert the fuzzy result of the rules into the output signal, known as defuzzification.

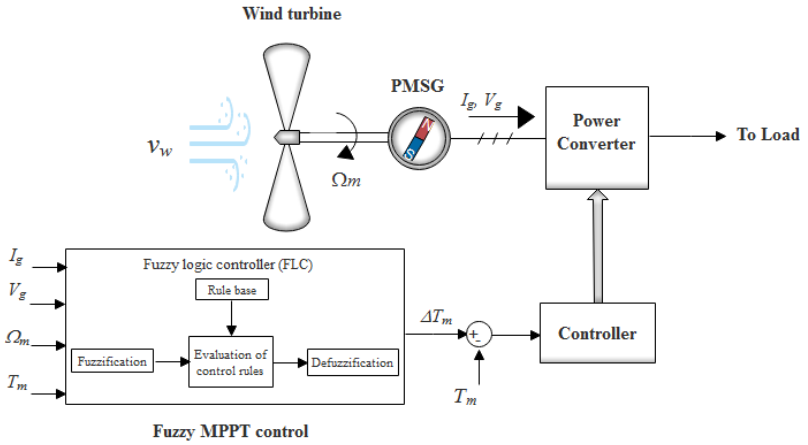

Figure 1. 17. Block diagram of FL MPPT controller for WECS.

They are hybrid systems, which combine other intelligent control methods such as NNs and Genetic Algorithms with the FL.

Many control strategies have appeared in the literature [76-81] concerning the use of the FLC for MPPT applications either independently or along with other methods. The main advantage of such controllers is that its parameters can be changed very quickly in response to changes in the system dynamics without parameter estimation. When the climatic conditions change, the performance of a fuzzy-based MPPT algorithm is strong, however, their strength depends a lot on the knowledge of the user in choosing the appropriate error, levels of membership functions and selection of rule base. The memory requirement also poses limitations in its implementation involving power processors, especially with a significant number of FL inputs raising the dimension of the rule base [22, 82].

Most of the systems proposed in the literature [83-88] use the MPPT structure shown in Figure 1.18 where the rotor speed (ω_m) and generator output power (P_m) are the inputs, while the output is the estimated maximum power that can be generated (ω_m^*). The main goal is to continuously adapt the rotational speed of the generator to the wind speed in a way that the turbine operates at its optimum level of aerodynamic efficiency. The principle of this strategy is to perturb the reference speed, ($\Delta\omega_m^*$) and to observe the corresponding change of power (ΔP_m). If the output power increases with the last speed increment, the searching process continues in the same direction. On the other hand, if the speed increment reduces the output power, the direction of the searching is reversed. This method doesn't need any information on the wind speed or WT parameters which makes it universal for different WT.

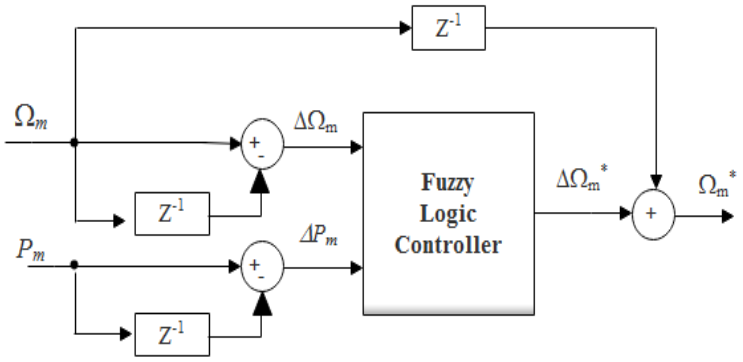

Figure 1. 18. Fuzzy MPPT controller.

In other studies, [77, 78, 89] use the difference between powers and their derivatives as inputs with standard triangular membership functions for both the input and the output. Generator power and output torque variation are used as inputs in [90] with triangular membership functions and seven rule base table. A rotational speed and an aerodynamic torque observer are taken as the input values of fuzzy-based MPPT as described in [91]. Another two input parameters, ΔT and $\Delta\omega_m$, are utilized to limit torque and speed variation. These input parameters are converted into predefined membership functions and send to FLC to accomplish the desired control. Although fuzzy has many benefits compared with other methods, it cannot be applied to each and every problem. Moreover, it requires studying the parameter for assigning the linguistic variables.

1.8.6 Comparison

After reviewing various MPPT algorithms from WECS, a comparative Table 1.2 is presented. A comparison is made among different performance indexes such as convergence speed, memory requirement, training, complexity, etc. The main objective of the MPPT algorithm is to track the optimum power point of VSWT. Choosing an appropriate MPPT technique is a tough task. In comparison, the indirect power control based algorithms such as TSR, OT, and PSF are simple and fast, but it maximizes the captured mechanical wind power instead of output electrical power. TSR control has good performance with fast response and high efficiency. An accurate anemometer is required, due to gust and turbulence, which is expensive and adds extra cost to the system, especially for small-scale WECSs. The practical implementation of this algorithm is difficult because the wind velocity close to the turbine is different from the free stream velocity. OT method is simple, fast, and efficient without a

wind speed sensor. However, it does not measure the wind speed direc0tly, therefore, variation in wind speed is not reflected instantly and significantly on the reference torque, which makes the efficiency of this algorithm less as compared to the TSR algorithm.

The PSF and the OT algorithms are approximately similar in terms of complexity and performance. These algorithms provides robust and cost-effective MPPT control for WECSs.

HCS algorithm is common and simple to implement because it does not need any measurement of the mechanical quantities like rotor speed, turbine speed or wind speed. The algorithm is independent and its tracking is not affected by the turbine or generator parameter shifts. By using the HCS algorithm, maximum power corresponding to any wind velocity can be captured. However, the time taken to reach MPP is long and a considerable amount of power loss takes place during the tracking phase. It can also cause smaller wind turbines to stall. The modified HCS algorithm overcomes the demerits of the HCS algorithm, which are the slow response and the incorrect directionality under rapid wind change. The HCS also results in slower tracking if the step size is too low and hunting (oscillation) around the MPP if the step size is too high, these problems are mitigated by fixed and adaptive step HCS algorithm.

FL based MPPT method is more robust and can handle nonlinearities that gives efficient systems with more reliable yields and greater energy compared with other techniques. The design of the fuzzy controllers does not require precise mathematical modeling or sophisticated computations that in many cases lack efficiency and good performance.

Table 1. 2. Comparison of characteristics of various MPPT methods [92, 93].

MPPT algorithm features	TSR	OTC	HCS	FLC
- Requirement of wind speed sensor	Yes	No	No	No
- Requirement of shaft speed sensor	No	Yes	No	No
- Look-up table requirement	No	Depends	No	No
- Requirement of system pre-knowledge	Yes	Yes	No	No
- Memory requirement	No	Depends	No	Yes
- Complexity	Least	Less	Moderate	High
- Cost	Very high	Moderate	Low	Low
- Convergence speed	Very fast	Fast	Moderate	Fast
- Oscillation at MPP	No	No	Yes	Depends
- MPPT efficiency	Highest	High	Low	Moderate
- Reprogramming with variation in pitch angle	No	Yes	No	Yes

-	Performance under rapid wind condition	Very good	Very good	Poor	excellent
-	Parameter sensitivity	No	Yes	No	No
-	Online updating	No	No	Yes	Depends

1.9 Conclusion

An attempt has been made in this chapter to discuss the most recent research trends in the field of WECS. The basic concepts and market trends of wind power technology were presented. The fundamentals of wind energy systems were discussed, including standalone and grid-connected operations, horizontal and vertical-axis wind turbines, fixed- and variable-speed operations. Power electronic converter topologies and energy storage systems.

From this review, it can be concluded that in terms of efficiency and reliability, the direct-drive PMSG system is found to be the best option. In particular, the direct-drive PMSG with diode rectifier was found to be currently the most preferred topology for small-scale, WECS, as it is less expensive compared to direct-drive PMSG with back to back converter.

There are different types of ESSs in power systems. The BESS is one of the most rapid-growing storage technologies. The BESS installation cost and generating noise are relatively lower than the other storage technologies.

In this chapter, a concise review of MPPT control methods proposed in various studies in the literatures for controlling WECS has been presented. From the comparative study, it has been observed that the performance of the FLC based MPPT algorithm is most promising due to higher efficiency and flexibility.

The next chapter deals with the mathematical modeling, analysis, and control of a standalone WECS adopted in this work namely: wind turbine, PMSG and a three-phase diode rectifier cascaded with a DC-DC boost converter.

References

[1] B. Wu, Y. Lang, N. Zargari, and S. Kouro, *Power Conversion and Control of Wind Energy Systems*. John Wiley & Sons, 2011.

[2] Z. Chen, J. M. Guerrero, and F. Blaabjerg, "A Review of the State of the Art of Power Electronics for Wind Turbines," *IEEE Transactions on Power Electronics*, vol. 24, no. 8, pp. 1859–1875, Aug. 2009.

[3] Y. Zou, M. E. Elbuluk, and Y. Sozer, "Simulation Comparisons and Implementation of Induction Generator Wind Power Systems," *IEEE Transactions on Industry Applications*, vol. 49, no. 3, pp. 1119–1128, May 2013.

[4] O. Carranza, E. Figueres, G. Garcerá, and R. Gonzalez-Medina, "Analysis of the control structure of wind energy generation systems based on a permanent magnet synchronous generator," *Applied Energy*, vol. 103, pp. 522–538, Mar. 2013.

[5] A. G. Aissaoui, A. Tahour, N. Essounbouli, F. Nollet, M. Abid, and M. I. Chergui, "A Fuzzy-PI control to extract an optimal power from wind turbine," *Energy Conversion and Management*, vol. 65, pp. 688–696, Jan. 2013.

[6] M. A. Abdullah, A. H. M. Yatim, C. W. Tan, and R. Saidur, "A review of maximum power point tracking algorithms for wind energy systems," *Renewable and sustainable energy reviews*, vol. 16, no. 5, pp. 3220–3227, 2012.

[7] B. Meghni, D. Dib, and A. T. Azar, "A second-order sliding mode and fuzzy logic control to optimal energy management in wind turbine with battery storage," *Neural Comput & Applic*, vol. 28, no. 6, pp. 1417–1434, Jun. 2017.

[8] "World Wind Energy Association – Wind Power Capacity reaches 597 GW, 50,1 GW added in 2018.". https://wwindea.org/blog/2019.

[9] D. Wood, "Small Wind Turbines," in *Advances in Wind Energy Conversion Technology*, M. Sathyajith and G. S. Philip, Eds. Berlin, Heidelberg: Springer Berlin Heidelberg, 2011, pp. 195–211.

[10] F. Blaabjerg and K. Ma, "Future on Power Electronics for Wind Turbine Systems," *IEEE Journal of Emerging and Selected Topics in Power Electronics*, vol. 1, no. 3, pp. 139–152, Sep. 2013.

[11] E.-E. E. Portal, "Large and Small Wind Turbines are Different," *EEP - Electrical Engineering Portal*, 29-Jun-2011. .

[12] "Wind Power in Power Systems, 2nd Edition, Thomas Ackermann.

[13] D. P. Kaundinya, P. Balachandra, and N. H. Ravindranath, "Grid-connected versus stand-alone energy systems for decentralized power—A review of literature," *Renewable and Sustainable Energy Reviews*, vol. 13, no. 8, pp. 2041–2050, Oct. 2009.

[14] C.-J. Bai and W.-C. Wang, "Review of computational and experimental approaches to analysis of aerodynamic performance in horizontal-axis wind turbines (HA*WT*s)," *Renewable and Sustainable Energy Reviews*, vol. 63, pp. 506–519, Sep. 2016.

[15] M. M. Aslam Bhutta, N. Hayat, A. U. Farooq, Z. Ali, Sh. R. Jamil, and Z. Hussain, "Vertical axis wind turbine – A review of various configurations and design techniques," *Renewable and Sustainable Energy Reviews*, vol. 16, no. 4, pp. 1926–1939, May 2012.

[16] W. Tong, *Wind Power Generation and Wind Turbine Design*. WIT Press, 2010.

[17] M. Stiebler, *Wind Energy Systems for Electric Power Generation*. Berlin Heidelberg: Springer-Verlag, 2008.

[18] A. Betz, *Wind-energie und ihre ausnutzung durch windmühlen*. Vandenhoeck, 1926.

[19] F. Blaabjerg and Z. Chen, *Power Electronics for Modern Wind Turbines*. Morgan & Claypool Publishers, 2006.

[20] M. M. Chowdhury, M. E. Haque, M. Aktarujjaman, M. Negnevitsky, and A. Gargoom, "Grid integration impacts and energy storage systems for wind energy applications — A review," in *2011 IEEE Power and Energy Society General Meeting*, 2011, pp. 1–8.

[21] E. Hau, *Wind Turbines: Fundamentals, Technologies, Application, Economics*, 2nd ed. edition. Springer, 2005.

[22] F. Blaabjerg and Z. Chen, *Power Electronics for Modern Wind Turbines*. Morgan & Claypool Publishers, 2006.

[23] M. Chowdhury, "Modelling and control of direct drive variable speed wind turbine with Interior Permanent Magnet Synchronous Generator.," p. 221, 2014.

[24] D. Bang, H. Polinder, G. Shrestha, and J. A. Ferreira, "Review of Generator Systems for Direct-Drive Wind Turbines," p. 11, April 2008.

[25] M. Singh and A. Chandra, "Application of Adaptive Network-Based Fuzzy Inference System for Sensorless Control of *PMSG*-Based Wind Turbine With Nonlinear-Load-Compensation Capabilities," *IEEE Transactions on Power Electronics*, vol. 26, no. 1, pp. 165–175, Jan. 2011.

[26] Z. q. Zhu and J. Hu, "Electrical machines and power-electronic systems for high-power wind energy generation applications: Part I – market penetration, current technology and advanced machine systems," *COMPEL*, vol. 32, no. 1, pp. 7–33, Dec. 2012.

[27] D. Bang, H. Polinder, G. Shrestha, and J. A. Ferreira, "Review of Generator Systems for Direct-Drive Wind Turbines," p. In: Proceedings of European Wind Energy Conference Exhibition; March/April 2008. pp. 1–11.

[28] Z. Chen and E. Spooner, "Grid power quality with variable speed wind turbines," *IEEE Transactions on Energy Conversion*, vol. 16, no. 2, pp. 148–154, Jun. 2001.

[29] A. Yazdani and R. Iravani, "A neutral-point clamped converter system for direct-drive variable-speed wind power unit," *IEEE Transactions on Energy Conversion*, vol. 21, no. 2, pp. 596–607, Jun. 2006.

[30] J. S. Thongam and M. Ouhrouche, "*MPPT* Control Methods in Wind Energy Conversion Systems," *Fundamental and Advanced Topics in Wind Power*, Jul. 2011.

[31] A. Abdelli, *Optimisation multicritère d'une chaîne éolienne passive*. 2007.

[32] Md. R. Islam, Y. Guo, and J. Zhu, "A review of offshore wind turbine nacelle: Technical challenges, and research and developmental trends," *Renewable and Sustainable Energy Reviews*, vol. 33, pp. 161–176, May 2014.

[33] Y. Daili, "Contribution à la commande d'une petite éolienne destinée à l'électrification des sites isolés," Thesis, 2016, Sétif.

[34] M. Singh, V. Khadkikar, and A. Chandra, "Grid synchronisation with harmonics and reactive power compensation capability of a permanent magnet synchronous generator-based variable speed wind energy conversion system," *IET Power Electronics*, vol. 4, no. 1, pp. 122–130, Jan. 2011.

[35] O. Carranza, E. Figueres, G. Garcerá, and L. G. Gonzalez, "Comparative study of speed estimators with highly noisy measurement signals for Wind Energy Generation Systems," *Applied Energy*, vol. 88, no. 3, pp. 805–813, Mar. 2011.

[36] A. Echchaachouai, S. El Hani, A. Hammouch, and S. Guedira, "A new sensorless Maximum Power Point Tracking technologies of wind conversion chain based on a *PMSG*," in *2014 International Renewable and Sustainable Energy Conference (IRSEC)*, Ouarzazate, Morocco, 2014, pp. 328–333.

[37] *Advances in Batteries for Medium and Large-Scale Energy Storage*. Elsevier book, 2015.

[38] M. I. Daoud, A. M. Massoud, A. S. Abdel-Khalik, A. Elserougi, and S. Ahmed, "A Flywheel Energy Storage System for Fault Ride Through Support of Grid-Connected VSC HVDC-Based Offshore Wind Farms," *IEEE Transactions on Power Systems*, vol. 31, no. 3, pp. 1671–1680, May 2016.

[39] A. A. K. Arani, H. Karami, G. B. Gharehpetian, and M. S. A. Hejazi, "Review of Flywheel Energy Storage Systems structures and applications in power systems and microgrids," *Renewable and Sustainable Energy Reviews*, vol. 69, pp. 9–18, Mar. 2017.

[40] K. C. Divya and J. Østergaard, "Battery energy storage technology for power systems—An overview," *Electric Power Systems Research*, vol. 79, no. 4, pp. 511–520, Apr. 2009.

[41] E. Reihani, S. Sepasi, L. R. Roose, and M. Matsuura, "Energy management at the distribution grid using a Battery Energy Storage System (*BESS*)," *International Journal of Electrical Power & Energy Systems*, vol. 77, pp. 337–344, May 2016.

[42] S. Nomoto, H. Nakata, K. Yoshioka, A. Yoshida, and H. Yoneda, "Advanced capacitors and their application," *Journal of Power Sources*, vol. 97–98, pp. 807–811, Jul. 2001.

[43] W. Buckles and W. V. Hassenzahl, "Superconducting magnetic energy storage," *IEEE Power Engineering Review*, vol. 20, no. 5, pp. 16–20, May 2000.

[44] M. M. Aly, M. Abdel-Akher, S. M. Said, and T. Senjyu, "A developed control strategy for mitigating wind power generation transients using superconducting magnetic energy storage with reactive power support," *International Journal of Electrical Power & Energy Systems*, vol. 83, pp. 485–494, Dec. 2016.

[45] O. Palizban and K. Kauhaniemi, "Energy storage systems in modern grids—Matrix of technologies and applications," *Journal of Energy Storage*, vol. 6, pp. 248–259, May 2016.

[46] X. Luo, J. Wang, M. Dooner, and J. Clarke, "Overview of current development in electrical energy storage technologies and the application potential in power system operation," *Applied Energy*, vol. 137, pp. 511–536, Jan. 2015.

[47] D. Thakur, "Power Management Strategies for a Wind Energy Source in an Isolated Microgrid and Grid Connected System," p. 288, 2015.

[48] R. Teodorescu, C. N. Rasmussen, P. Rodriguez, and H. Vikelgaard, *Overview of the Energy Storage Systems for Wind Power Integration Enhancement*. July 2010.

[49] G. J. May, A. Davidson, and B. Monahov, "Lead batteries for utility energy storage: A review," *Journal of Energy Storage*, vol. 15, pp. 145–157, Feb. 2018.

[50] A. M. O. Haruni, "A stand-alone hybrid power system with energy storage," phd, University of Tasmania, 2013.

[51] B. B. McKeon, J. Furukawa, and S. Fenstermacher, "Advanced Lead–Acid Batteries and the Development of Grid-Scale Energy Storage Systems," *Proceedings of the IEEE*, vol. 102, no. 6, pp. 951–963, Jun. 2014.

[52] D. Kumar and K. Chatterjee, "A review of conventional and advanced *MPPT* algorithms for wind energy systems," *Renewable and Sustainable Energy Reviews*, vol. 55, pp. 957–970, Mar. 2016.

[53] M. Cheng and Y. Zhu, "The state of the art of wind energy conversion systems and technologies: A review," *Energy Conversion and Management*, vol. 88, pp. 332–347, Dec. 2014.

[54] K. Nishida, T. Ahmed, and M. Nakaoka, "A Cost-Effective High-Efficiency Power Conditioner With Simple *MPPT* Control Algorithm for Wind-Power Grid Integration," *IEEE Transactions on Industry Applications*, vol. 47, no. 2, pp. 893–900, Mar. 2011.

[55] Quincy Wang and Liuchen Chang, "An intelligent maximum power extraction algorithm for inverter-based variable speed wind turbine systems," *IEEE Transactions on Power Electronics*, vol. 19, no. 5, pp. 1242–1249, Sep. 2004.

[56] B. Babes, L. Rahmani, A. Chaoui, and N. Hamouda, "Design and Experimental Validation of a Digital Predictive Controller for Variable-Speed Wind Turbine Systems," *Journal of Power Electronics (JPE)*, vol. 17, no. 1, pp. 232–241, 2017.

[57] M. Nasiri, J. Milimonfared, and S. H. Fathi, "Modeling, analysis and comparison of *TSR* and OT*C* methods for *MPPT* and power smoothing in permanent magnet synchronous generator-based wind turbines," *Energy Conversion and Management*, vol. 86, pp. 892–900, Oct. 2014.

[58] Hui Li, K. L. Shi, and P. G. McLaren, "Neural-network-based sensorless maximum wind energy capture with compensated power coefficient," *IEEE Transactions on Industry Applications*, vol. 41, no. 6, pp. 1548–1556, Nov. 2005.

[59] M. N. Eskander, "Neural network controller for a permanent magnet generator applied in a wind energy conversion system," *Renewable Energy*, vol. 26, no. 3, pp. 463–477, Jul. 2002.

[60] M. Pucci and M. Cirrincione, "Neural *MPPT* Control of Wind Generators With Induction Machines Without Speed Sensors," *IEEE Transactions on Industrial Electronics*, vol. 58, no. 1, pp. 37–47, Jan. 2011.

[61] S. Ganjefar, A. A. Ghassemi, and M. M. Ahmadi, "Improving efficiency of two-type maximum power point tracking methods of tip-speed ratio and optimum torque in wind turbine system using a quantum neural network," *Energy*, vol. 67, pp. 444–453, 2014.

[62] A. Tapia, G. Tapia, J. X. Ostolaza, and J. R. Saenz, "Modeling and control of a wind turbine driven doubly fed induction generator," *IEEE Transactions on Energy Conversion*, vol. 18, no. 2, pp. 194–204, Jun. 2003.

[63] S. M. R. Kazmi, H. Goto, H. Guo, and O. Ichinokura, "Review and critical analysis of the research papers published till date on maximum power point tracking in wind energy conversion system," in *2010 IEEE Energy Conversion Congress and Exposition*, 2010, pp. 4075–4082.

[64] J. Chen, J. Chen, and C. Gong, "New Overall Power Control Strategy for Variable-Speed Fixed-Pitch Wind Turbines Within the Whole Wind Velocity Range," *IEEE Transactions on Industrial Electronics*, vol. 60, no. 7, pp. 2652–2660, Jul. 2013.

[65] A. Urtasun, P. Sanchis, I. San Martín, J. López, and L. Marroyo, "Modeling of small wind turbines based on *PMSG* with diode bridge for sensorless maximum power tracking," *Renewable Energy*, vol. 55, pp. 138–149, Jul. 2013.

[66] H.- Zhang, J. Fletcher, N. Greeves, S. J. Finney, and B. W. Williams, "One-power-point operation for variable speed wind/tidal stream turbines with synchronous generators," *IET Renewable Power Generation*, vol. 5, no. 1, pp. 99–108, Jan. 2011.

[67] Y. Xia, K. H. Ahmed, and B. W. Williams, "Wind Turbine Power Coefficient Analysis of a New Maximum Power Point Tracking Technique," *IEEE Transactions on Industrial Electronics*, vol. 60, no. 3, pp. 1122–1132, Mar. 2013.

[68] E. Koutroulis and K. Kalaitzakis, "Design of a maximum power tracking system for wind-energy-conversion applications," *IEEE Transactions on Industrial Electronics*, vol. 53, no. 2, pp. 486–494, Apr. 2006.

[69] M. Kesraoui, N. Korichi, and A. Belkadi, "Maximum power point tracker of wind energy conversion system," *Renewable Energy*, vol. 36, no. 10, pp. 2655–2662, Oct. 2011.

[70] A. M. Eltamaly and H. M. Farh, "Maximum power extraction from wind energy system based on fuzzy logic control," *Electric Power Systems Research*, vol. 97, pp. 144–150, Apr. 2013.

[71] L. Belhadji, S. Bacha, I. Munteanu, A. Rumeau, and D. Roye, "Adaptive *MPPT* Applied to Variable-Speed Microhydropower Plant," *IEEE Transactions on Energy Conversion*, vol. 28, no. 1, pp. 34–43, Mar. 2013.

[72] M. Elnaggar, H. A. Abdel Fattah, and A. L. Elshafei, "Maximum power tracking in *WECS* (Wind energy conversion systems) via numerical and stochastic approaches," *Energy*, vol. 74, pp. 651–661, Sep. 2014.

[73] Y. Daili, J.-P. Gaubert, and L. Rahmani, "Implementation of a new maximum power point tracking control strategy for small wind energy conversion systems without mechanical sensors," *Energy Conversion and Management*, vol. 97, pp. 298–306, Jun. 2015.

[74] H. M. Nguyen and D. S. Naidu, "Advanced control strategies for wind energy systems: An overview," in *2011 IEEE/PES Power Systems Conference and Exposition*, 2011, pp. 1–8.

[75] A. Kentli, "Studies on Fuzzy Logic Control of Electrical Machines in Turkish Universities: An Overview," *Mathematical and Computational Applications*, vol. 16, no. 1, pp. 236–247, Apr. 2011.

[76] M. G. Simoes, B. K. Bose, and R. J. Spiegel, "Fuzzy logic based intelligent control of a variable speed cage machine wind generation system," *IEEE Transactions on Power Electronics*, vol. 12, no. 1, pp. 87–95, Jan. 1997.

[77] A. Z. Mohamed, M. N. Eskander, and F. A. Ghali, "Fuzzy logic control based maximum power tracking of a wind energy system," *Renewable Energy*, vol. 23, no. 2, pp. 235–245, Jun. 2001.

[78] A. G. Abo-Khalil, Dong-Choon Lee, and Jul-Ki Seok, "Variable speed wind power generation system based on fuzzy logic control for maximum output power tracking," in *2004 IEEE 35th Annual Power Electronics Specialists Conference (IEEE Cat. No.04CH37551)*, 2004, vol. 3, pp. 2039-2043 Vol.3.

[79] P. Flores, A. Tapia, and G. Tapia, "Application of a control algorithm for wind speed prediction and active power generation," *Renewable Energy*, vol. 30, no. 4, pp. 523–536, Apr. 2005.

[80] V. Galdi, A. Piccolo, and P. Siano, "Designing an Adaptive Fuzzy Controller for Maximum Wind Energy Extraction," *IEEE Transactions on Energy Conversion*, vol. 23, no. 2, pp. 559–569, Jun. 2008.

[81] V. Calderaro, V. Galdi, A. Piccolo, and P. Siano, "A fuzzy controller for maximum energy extraction from variable speed wind power generation systems," *Electric Power Systems Research*, vol. 78, no. 6, pp. 1109–1118, Jun. 2008.

[82] A. Hazzab, I. K. Bousserhane, M. Zerbo, and P. Sicard, "Real Time Implementation of Fuzzy Gain Scheduling of PI Controller for Induction Motor Machine Control," *Neural Process Lett*, vol. 24, no. 3, pp. 203–215, Dec. 2006.

[83] A. Borni, T. Abdelkrim, L. Zaghba, A. Bouchakour, A. Lakhdari, and L. Zarour, "Fuzzy logic, PSO based fuzzy logic algorithm and current controls comparative for grid-connected hybrid system," presented at the technologies and materials for renewable energy, environment and sustainability: tmrees16-Cnam, Paris, France, 2017, p. 020006.

[84] H. Slah, D. Mehdi, and S. Lassaad, "Advanced Control of a *PMSG* Wind Turbine," *International Journal of Modern Nonlinear Theory and Application*, vol. 05, p. 1, 2016.

[85] M. Kesraoui, S. A. Lagraf, and A. Chaib, "Aerodynamic power control of wind turbine using fuzzy logic," in *2015 3rd International Renewable and Sustainable Energy Conference (IRSEC)*, 2015, pp. 1–6.

[86] M. B. Smida and A. Sakly, "Fuzzy pitch angle control for grid connected variable-speed wind turbine system," in *2016 7th International Renewable Energy Congress (IREC)*, 2016, pp. 1–6.

[87] A. Slimen, H. Tlijani, M. Dhaoui, and R. B. Younes, "Intelligent control of wind pump based on *PMSG* using pitch control," in *2017 14th International Multi-Conference on Systems, Signals Devices (SSD)*, 2017, pp. 59–64.

[88] A. S. Al-Toma, G. A. Taylor, and M. Abbod, "Intelligent pitch angle control scheme for variable speed wind generator systems," in *2017 52nd International Universities Power Engineering Conference (UPEC)*, 2017, pp. 1–6.

[89] X.-Y. Zhang, J. Cheng, and W. Wang, "The intelligent control method study of variable speed wind turbine generator," *2008 IEEE International Conference on Sustainable Energy Technologies*, pp. 173–177, 2008.

[90] Z. Chen, S. A. Gomez, and M. McCormick, "A fuzzy logic controlled power electronic system for variable speed wind energy conversion systems," in *2000 Eighth International Conference on Power Electronics and Variable Speed Drives (IEE Conf. Publ. No. 475)*, 2000, pp. 114–119.

[91] B. Neammanee, K. Krajangpan, S. Sirisumrannukul, and S. Chatrattana, "Maximum Peak Power Tracking-Based Control Algorithms with Stall Regulation for Optimal Wind Energy Capture," in *2007 Power Conversion Conference - Nagoya*, 2007, pp. 1424–1430.

[92] B. Babes and L. Rahmani, "Commande prédictive de la machine synchrone à aimant permanent utilisée dans un système éolien," phd, Université Ferhat Abbas faculté de Technologie département d'électrotechnique, Sétif, 2018.

[93] M. B. H. Kumar, B. Saravanan, P. Sanjeevikumar, and F. Blaabjerg, "Review on control techniques and methodologies for maximum power extraction from wind energy systems," *IET Renewable Power Generation*, vol. 12, no. 14, pp. 1609–1622, Aug. 2018.

Chapter 2. Modeling and control of a standalone wind energy conversion system

2.1 Introduction

Small wind energy conversion systems (SWECS) equipped with PMSG compared to those using induction generators have several benefits [1, 2]. First, PMSG can provide high-reliability power generation since there is no need for external magnetization. Second, the high torque density of the PMSG allows a reduction in the cost of the system [3]. Moreover, a wind turbine with a multi-polar PMSG removes the need for a gearbox [4]. Thus, the system requires less servicing [5]. This chapter presents the modeling, analysis, and control of a PMSG based on standalone VSWT using a switch-mode rectifier. The latter using a diode rectifier and DC-DC boost converter is suitable for low power applications. This type of converters has advantages such as simple structure, low cost, high reliability, and simple MPPT control algorithm [6, 7]. However, it introduces high harmonic distortion and is unable to control the power factor which affects the system performance and efficiency [6, 7].

In this chapter two conventional MPPT algorithms have been proposed namely TSR and Optimum Relation Based (ORB). With the first MPPT technique, the control variable allowing the system to operate at the MPP is obtained by regulating the rotational speed of the generator [7]. This algorithm requires the measured value of wind speed as well as the generator speed to get the optimum TSR (λ_{opt}) of the turbine so as for the system to be in a position to extract maximum attainable power. The TSR algorithm is highly efficient and has a quick response [8]. However, the need of an accurate anemometer for measuring the wind speed makes the system more costly, particularly for small scale WECS.

The algorithm based on the optimum relationship does not need the anemometer, but still, requires the parameters of the specific wind turbine. It has the advantage of a good dynamic response. Nevertheless, to implement the MPPT successfully, a priori relationship needs to be known, which is not easy to determine for real wind energy systems [9, 10].

The detailed analysis of the control scheme is presented. The effectiveness and validity of the two control algorithms developed in this chapter are evaluated based on time-domain simulation studies.

2.2 Wind system configuration

Figure 2.1 shows the system structure of a PMSG based on a variable speed wind turbine using switch-mode rectifier. The PMSG is coupled directly to a three-blade horizontal axis wind turbine; a three-phase diode bridge is employed to rectify the generated output voltage. Due to the uncontrollability of the diode rectifier, a DC-DC converter is used to realize the MPPT operation; only one active power switch device *S* is needed, which reduces the cost and simplifies the control of the system. For simplicity, a resistance load R_L is connected directly to the output of the DC-DC converter to consume the power generated by the SWECS, that can be substituted by a DC–AC inverter with a unity power factor connected to the utility grid or supplying a local load in case of off-grid applications [8, 9].

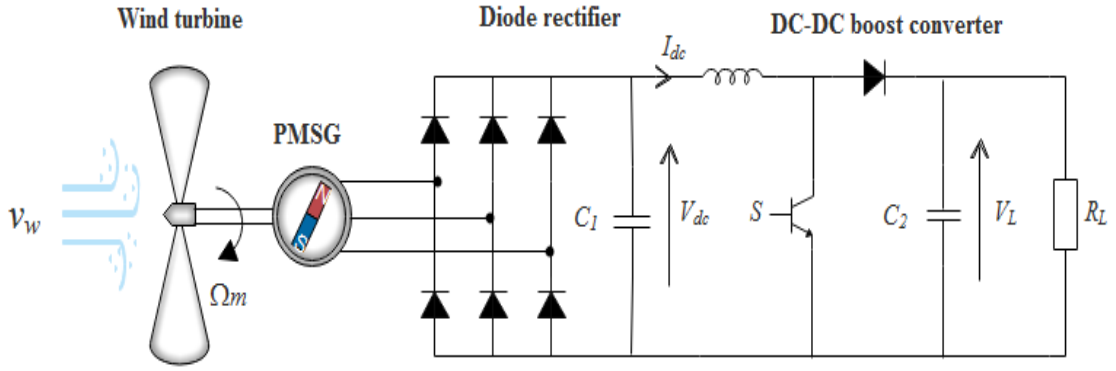

Figure 2. 1. Configuration of the studied system.

2.3 Wind turbine modeling

A wind turbine converts the kinetic energy of the wind into mechanical energy using the rotor blades. The amount of energy which the wind transfers to the rotor depends on the density of the air, the rotor swept area, and the wind speed. The rotor blades of the wind turbine capture only part of the available wind power, and the actual power extracted by a wind turbine is given by equation (2.1) below [12]:

$$P_m = \tfrac{1}{2}\rho\pi R^2 v_w^3 C_p(\lambda,\beta) \qquad (2.1)$$

where ρ is the air density, *R* is the radius of the turbine, v_w is the wind speed, λ is the tip-speed ratio, β is the blade pitch angle, C_p is the power coefficient of the rotor or rotor efficiency [13]. 59.3% is the maximum theoretical efficiency of a wind turbine rotor, it is called the *Betz efficiency* or *Betz' law*. In practical designs, the maximum achievable power coefficient is between 40% and 50% for a three-bladed horizontal axis wind turbine [14].

Based on a previous literature research, the theoretical maximum rotor blade efficiency or power coefficient C_p can be defined as a function of the tip-speed ratio λ and the blade pitch angle β as follows [9]:

$$C_p(\lambda,\beta) = 0.5176\left(\frac{116}{\lambda_i} - 0.4\beta - 5\right)e^{\frac{-21}{\lambda_i}} + 0.0068\lambda \tag{2.2}$$

with

$$\frac{1}{\lambda_i} = \frac{1}{\lambda + 0.08\beta} - \frac{0.055}{\beta^3 + 1} \tag{2.3}$$

β is the blade pitch angle in radians which is taken equal to zero in this work. The TSR is represented by equation (2.4):

$$\lambda = \frac{\Omega_m . R}{v_w} \tag{2.4}$$

The mechanical torque developed by the wind turbine is finally obtained from equation (2.5) [11, 14]:

$$T_m = \frac{P_m}{\Omega_m} = \frac{1}{2}\rho A \frac{v_w^3}{\Omega_m} C_p \tag{2.5}$$

where A is the swept area of wind turbine blade.

The synoptic scheme of the aerodynamic wind turbine model defined by equations (2.3), (2.4) and (2.5) is shown in Figure.2 2.

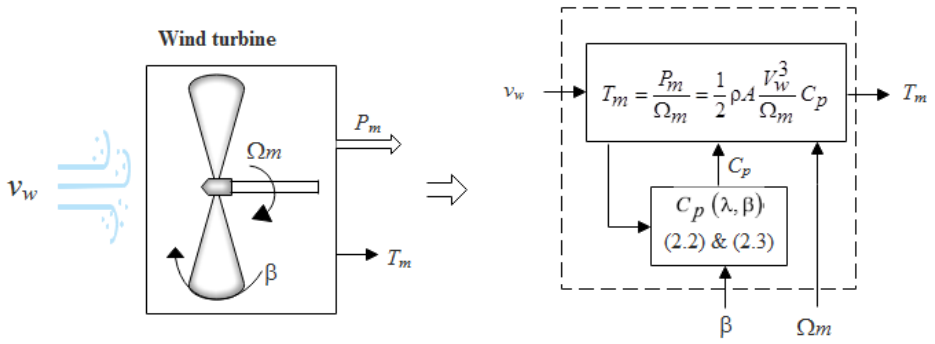

Figure 2. 2. Aerodynamic model of the wind turbine.

2.4 Mechanical drive train model

The power associated with the wind is transmitted to the electrical generator by means of a mechanical transmission, called the drive train. The mathematical model of the direct drive

train depends on the structure of the WECS and on its rated power. Given that a small wind turbine has a low moment of inertia, the drive train model can be simplified to be a one lumped mass model [16, 17].

According to equation (2.6), which is the wind turbine dynamic equation, the drive train model can be simulated as disclosed in Figure 2.3 [18]. Equation (2.6) indicates that the rate of the turbine rotor acceleration or deceleration, defined by $\frac{d\Omega_m}{dt}$, is proportional to the resultant torque on the turbine shaft and its direction.

$$\frac{d\Omega_m}{dt} = \frac{1}{J}\left(T_m - T_e - B_m\Omega_m\right) \tag{2.6}$$

where:

Ω_m: the turbine rotational speed [rad/s],

T_m: the mechanical torque [N.m],

T_e: the electrical torque [N.m],

B_m: the damping coefficient [N.m.s/rad],

J_{eq} is the equivalent rotational inertia of the generator [kg.m^2], which is derived from:

$$J_{eq} = J_g + \frac{J_m}{n_g^2}$$

where J_g and J_m; are the generator and the rotor rotational inertias [Kg.m^2] respectively, n_g is the gear ratio. For direct driven wind turbines with multi-pole synchronous generator, the gearbox can be omitted (n_g=1).

The structure of the model is depicted in figure 2.3.

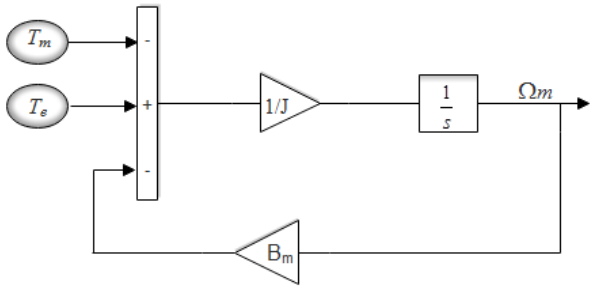

Figure 2. 3. Drive train model.

2.5 PMSG modeling

PMSGs play a key role in direct-drive wind power generation systems for transforming mechanical power into electrical power. Rigorous mathematical modeling of the PMSG is the prerequisite for the design of the machine control algorithms as well as the analysis of the steady-state and dynamic characteristics of wind energy conversion systems. Before developing the mathematical model of the PMSG, several important assumptions need to be made [3, 19]:

1. The damping effects in the magnets and in the rotor are negligible;
2. The magnetic saturation effects are neglected;
3. The eddy current and hysteresis losses are neglected;
4. The back electromotive force (EMF) induced in the stator windings is sinusoidal;
5. The stator windings are sinusoidally distributed along the air gap.

As the generator is directly coupled to the wind turbine rotor, the relationship between the electric speed and the mechanical speed can be expressed as:

$$\omega_e = P\Omega_m \tag{2.7}$$

where P is the number of the pole pairs.

To simplify the analysis of synchronous machinery models, the PMSG dynamic equations are expressed in the d–q reference frame as follows [20]:

$$\begin{cases} V_{sq} = -R_S \cdot i_{sq} - \dfrac{d\varphi_{sq}}{dt} - \omega_e \varphi_{sd} + \omega_e \phi_m \\ V_{sd} = -R_S \cdot i_{sd} - \dfrac{d\varphi_{sd}}{dt} + \omega_e \varphi_{sq} \end{cases} \tag{2.8}$$

R_s: the stator resistance,

ω_e: the electrical rotating speed,

i_{sq}, i_{sd}: the currents in the (d-q) reference frame,

L_d, L_q: the inductances in the (d-q)-axis,

Φ_{sd}, Φ_{sq},: the d-q- axes stator flux linkages,

ϕ_m: the rotor magnetic flux produced by the generator.

The equivalent circuits of the PMSM in the dq-axes reference frame can be drawn as shown in figure 2.4.

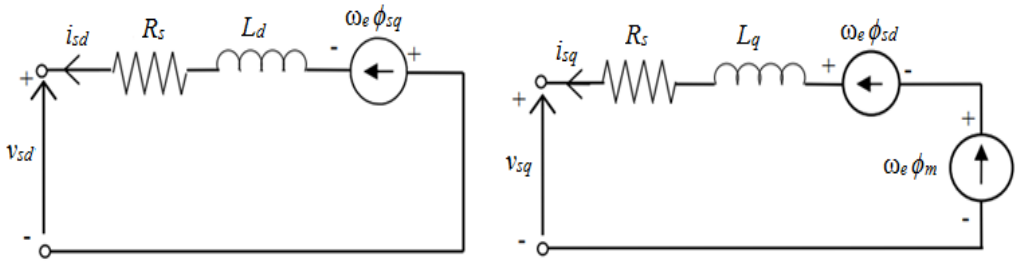

Figure 2. 4. *d-q* model of PMSG in the synchronous reference frame.

The expression (2.9) of the electromagnetic torque T_e is provided by [21]:

$$T_e = \frac{3}{2} P\left[\left(L_d - L_q\right) i_{sd} i_{sq} + \phi_m i_{sq}\right] \tag{2.9}$$

The stator inductances in *d* and *q* axes are approximately equal for a non-salient-pole PMSG (L_d=L_q). Thus, the electromagnetic torque expression can be simplified to:

$$T_e = \frac{3}{2} P \times \phi_m i_{sq} \tag{2.10}$$

2.6 Three Phase Diode Rectifier

Figure 2.5 shows the PMSG with a three-phase diode rectifier, where R_s is the stator resistance, L_s is the stator inductance of PMSG. The instantaneous phase voltages of the PMSG are given by:

$$\begin{cases} v_{an} = V_m \sin(\omega t) \\ v_{bn} = V_m \sin(\omega t - 120°) \\ v_{cn} = V_m \sin(\omega t - 240°) \end{cases} \tag{2.11}$$

where, V_m is the peak value of phase voltage.

$$V_m = \omega_e \Phi_m \tag{2.12}$$

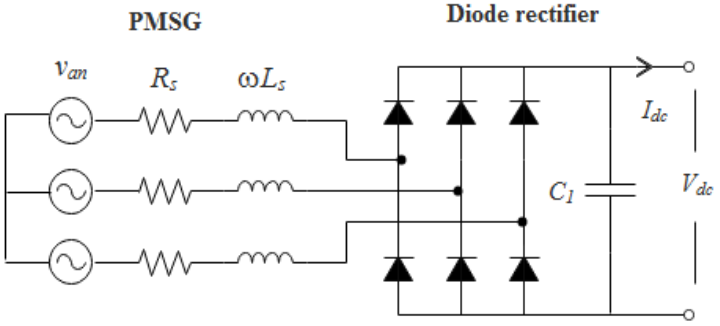

Figure 2. 5. PMSG with a three-phase diode rectifier.

The rectifier average output voltage V_{dc1} (neglecting *Rs* and $Xs=\omega L_S$) is [22]:

$$V_{dc} = \frac{1}{\pi/3}\int_{\pi/3}^{2\pi/3} \sqrt{3}V_m \sin(\omega_e t)\, d\omega t = \frac{3\sqrt{3}}{\pi}V_m = \frac{3\sqrt{3}}{\pi}\omega_e \phi_m \tag{2.13}$$

The amplitude of AC voltage terms are [23]:

$$V_n = \frac{6\sqrt{3}}{\pi\left(n^2-1\right)}V_m \tag{2.14}$$

where, n= 6,12,18 …

As the output voltage ripple is periodic with a period equal to 1/6 of the rectifier input, the harmonics in the output are of order $6K\omega_e$, *K*=1,2,3,…

If the generator inductance L_s is considered, the rectifier output DC voltage can be given by equation (2.15) below [16].

$$V_{dc} = \frac{3\sqrt{3}}{2\pi}V_m\left(1+\cos(u)\right) \tag{2.15}$$

where *u* is the overlap angle given by :

$$u = \cos^{-1}\left(1-\frac{2I_{dc}L_s\omega_e}{\sqrt{3E}}\right) \tag{2.16}$$

Where *E* is the magnitude of the electromotive force per phase of the PMSG.

Note that the presence of the generator inductor causes a voltage drop and reduces the DC output voltage.

The Fourier series of the currents in phase *a* of the AC line is [24]:

$$i_a(t) = \sum_{k=1,5,7}^{\inf}\left(A_{0k}\cos k\omega_e t + B_{0k}\sin k\omega_e t\right) \tag{2.17}$$

where

$$A_{0k} = \frac{I_{dc}\sqrt{3}}{\pi}(-1)^{l+1}\left[\frac{2\sin ku}{k}+\frac{1}{1-\cos u}\left(-\frac{2\sin ku}{k}+\frac{\sin(k+1)u}{k+1}+\frac{\sin(k-1)u}{k-1}\right)\right] \tag{2.18}$$

$$B_{0k} = \frac{I_{dc}\sqrt{3}}{\pi}(-1)^{l+1}\left[\frac{2\cos ku}{k}+\frac{1}{1-\cos u}\left(-\frac{2(1-\cos ku)}{k}-\frac{1-\cos(k+1)u}{k+1}-\frac{1-\cos(k-1)u}{k-1}\right)\right] \tag{2.19}$$

Since the AC circuit is assumed balanced, phase *b* and *c* currents are known as they have $2\pi/3$ and $4\pi/3$ phase shifts relative to phase *a* current, respectively. Then, using a *dq* transformation:

$$i_{sq} = -\frac{2}{3}\left(i_a \sin\omega_e t + i_b \sin\left(\omega_e t-\frac{2\pi}{3}\right)+i_c \sin\left(\omega_e t-\frac{4\pi}{3}\right)\right) \tag{2.20}$$

Substituting (2.17) into (2.20):

$$i_{sq} = -\Sigma_{k=1,5,7}^{\inf}\left(A_{0k}\cos(1-k)\omega_e t + B_{0k}\sin(1-k)\omega_e t\right) \tag{2.21}$$

From (2.21), the average i_{sq} can be expressed as:

$$i_{sq} = \frac{1}{2\pi}\int_0^{2\pi} i_{sq}\, d\omega t = -B_{01} \tag{2.22}$$

Where

$$B_{01} = \frac{I_{dc}\sqrt{3}}{\pi}\left(2 - 2\cos u - \frac{1-\cos 2u}{2(1-\cos u)}\right) \tag{2.23}$$

As can be seen from equations (2.22), (2.23) and (2.10), the generator electromechanical torque T_e can be varied by controlling the current I_{dc}.

2.7 DC-DC boost converter

DC-DC converters are power electronic circuits that convert a DC voltage to a different DC voltage level, often providing a regulated output used either for supplying DC power to the resistive load or storing energy in batteries.

The output of the three-phase rectifier feeds the input of the DC-DC boost converter to regulate the DC link voltage V_{dc} to a suitable level for the proper wind operation. This regulation can be easily achieved by PWM at a fixed frequency. A typical circuit diagram for the boost converter is shown in Figure 2.6.

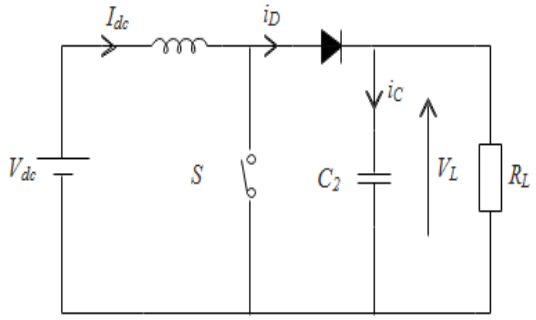

Figure 2. 6. A simplified circuit for the boost converter.

When the switch is closed (Figure 2.7), the diode is reverse biased, and the output is isolated from the input. The input supplies energy to the inductor. Kirchhoff's voltage law around the path containing the source, inductor, and closed switch is:

$$\frac{dI_{dc}}{dt} = \frac{V_{dc}}{L} \tag{2.24}$$

The rate of change of the current is a constant, so the current increases linearly while the switch is closed, as shown in Figure. 2.9.b. The change in the inductor current is computed from:

$$\frac{\Delta I_{dc}}{\Delta t} = \frac{\Delta I_{dc}}{DT} = \frac{V_{dc}}{L} \tag{2.25}$$

where D is the duty cycle.

Solving for Δi_L for the switch closed,

$$\left(\Delta I_{dc}\right)_{closed} = \frac{V_{dc} DT}{L} \tag{2.26}$$

When the switch is opened (Figure 2.8), the inductor current cannot change instantaneously, so the diode becomes forward-biased to provide a path for inductor current. Assuming that the output voltage (V_{dc}) is a constant, the voltage across the inductor is:

$$\begin{cases} V_i = V_{dc} - V_L = L\dfrac{dI_{dc}}{dt} \\ \dfrac{dI_{dc}}{dt} = \dfrac{V_{dc} - V_L}{L} \end{cases} \tag{2.27}$$

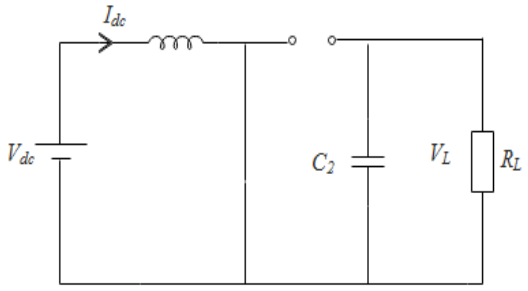

Figure 2. 7. Equivalent circuit for the switch closed.

The rate of change of the inductor current is a constant, so the current must change linearly while the switch is open. The change in inductor current while the switch is open is:

$$\frac{\Delta I_{dc}}{\Delta t} = \frac{\Delta I_{dc}}{(1-D)T} + \frac{V_{dc} - V_L}{L} \tag{2.28}$$

Solving for ΔI_{dc},

$$\left(\Delta I_{dc}\right)_{open} = \frac{\left(V_{dc} - V_L\right)(1-D)T}{L} \tag{2.29}$$

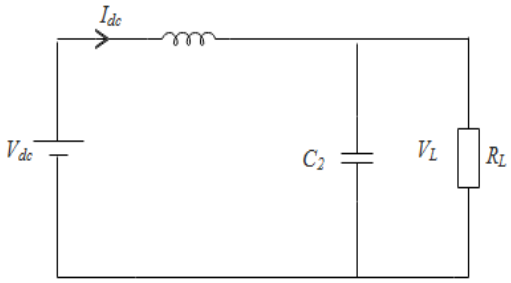

Figure 2. 8. Equivalent circuit for the switch open.

Depending on the continuity of the DC inductor current I_{dc}, the operation of the converter can be divided into two operating modes: continuous-current mode (CCM) and discontinuous-current mode (DCM). When a boost converter operates in CCM, the inductor current (I_{dc}) never falls to zero. Figure 2.9 shows the typical waveforms of currents and voltages in the boost converter operating in this mode [19].

For steady-state operation, the net change in the inductor current must be zero. Using equations (2.26) and (2.29),

$$\begin{cases} \left(\Delta I_{dc}\right)_{closed} + \left(\Delta I_{dc}\right)_{open} = 0 \\ \dfrac{V_{dc} DT}{L} + \dfrac{\left(V_{dc} - V_L\right)(1-D)T}{L} = 0 \\ V_{dc}\left(1-D\right) - V_L\left(1-D\right) = 0 \end{cases} \tag{2.30}$$

Solving for V_L,

$$V_L = \frac{V_{dc}}{1-D} \tag{2.31}$$

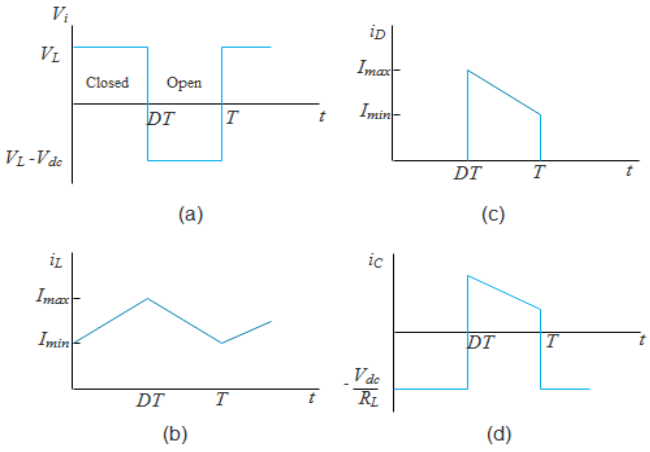

Figure 2. 9. Boost converter waveforms. (a) Inductor voltage; (b) Inductor current; (c) Diode current; (d) Capacitor current.

As the duty ratio is increased, the denominator of equation (2.31) becomes smaller, resulting in a larger output voltage. The boost converter produces an output voltage that is greater than or equal to the input voltage.

Maximum and minimum inductor currents are determined by using the average value and the change in the current from equation (2.29).

$$I_{\max} = I_{dc} + \frac{\Delta I_{dc}}{2} = \frac{V_{dc}}{(1-D)^2 R_L} + \frac{V_{dc} DT}{2L} \tag{2.32}$$

$$I_{\min} = I_{dc} - \frac{\Delta I_{dc}}{2} = \frac{V_{dc}}{(1-D)^2 R_L} - \frac{V_{dc} DT}{2L} \tag{2.33}$$

The minimum combination of inductance and switching frequency (f_s) for continuous current in the boost converter is, therefore [23].

$$L_{\min} = \frac{D(1-D)^2 R}{2 f_s} \tag{2.34}$$

The output power of the DC-DC boost converter can be expressed as follows [16]:

$$P_{dc} = \frac{{V_{dc}}^2}{R_L (1-D)^2} \tag{2.35}$$

2.8 Control of switch-mode rectifier with Maximum Power Extraction

This section presents a control development for a switch-mode rectifier using two conventional control methods to perform the MPPT. The main goal is to operate the WECS around the maximum power for any variations of the wind speed, which can be achieved by adjusting the duty cycle in such a way that the optimal tip speed ratio λ_{opt} is maintained [8, 28].

2.8.1 MPPT with Optimal TSR

The goal of this method is to maintain the TSR at a fixed optimum value, so that maximum power can be extracted [25]. Regardless the wind speed, the optimal TSR for a given turbine remains constant. Figure 2.10 shows the power coefficient C_p versus the TSR curve. It can be seen that there is an optimum TSR for λ_{opt}=8.01 at which the power coefficient is maximum C_{p_max}=0.48. Therefore, the mechanical power extracted from the wind is also maximum.

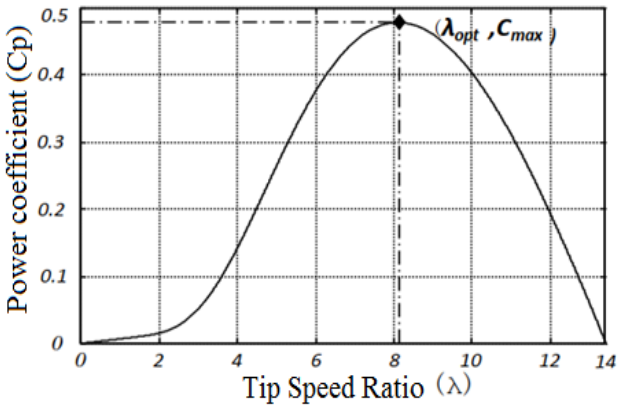

Figure 2. 10. Power coefficient versus tip speed ratio.

In this method, the maximum mechanical power is captured by the wind turbine by regulating the generator speed under different wind speeds. The principle of this control scheme is shown in the figure 2.11 where the measured wind speed v_w is used to produce the generator speed reference ω_{e_ref} according to the λ_{opt}. The generator speed ω_e is controlled by the boost converter and will be equal to its reference in steady-state, at which the *MPPT* is achieved. The control algorithm includes the following steps.

1- The desired rotational speed (Ω_{m_ref}=Ω_{m_opt}) is calculated with the following equation:

$$\Omega_{m\_ref} = \frac{\lambda_{opt}}{R} v_w \tag{2.36}$$

The relationship between the electric speed and the mechanical speed can be expressed as:

$$\omega_e = P\Omega_m \tag{2.37}$$

where P is the number of the pole pairs of the PMSG,

2- The error between the reference speed and the actual speed is fed into the *PI* controller to set the reference torque generator T_{e_ref},

3- This reference torque is then used to calculate the inductor current reference (I_{L_ref}) by using the given equation [11]:

$$I_{dc}^{*} = \frac{T_e^{*} \times \omega_e}{V_{dc}} \tag{2.38}$$

4- The error between the reference DC current and the measured inductor current is passed through the proportional-integral (PI) controller to produce the duty cycle (D).

5- Finally, the duty cycle (D) is used to produce the required PWM pulses for the IGBT switch of the boost DC-DC converter.

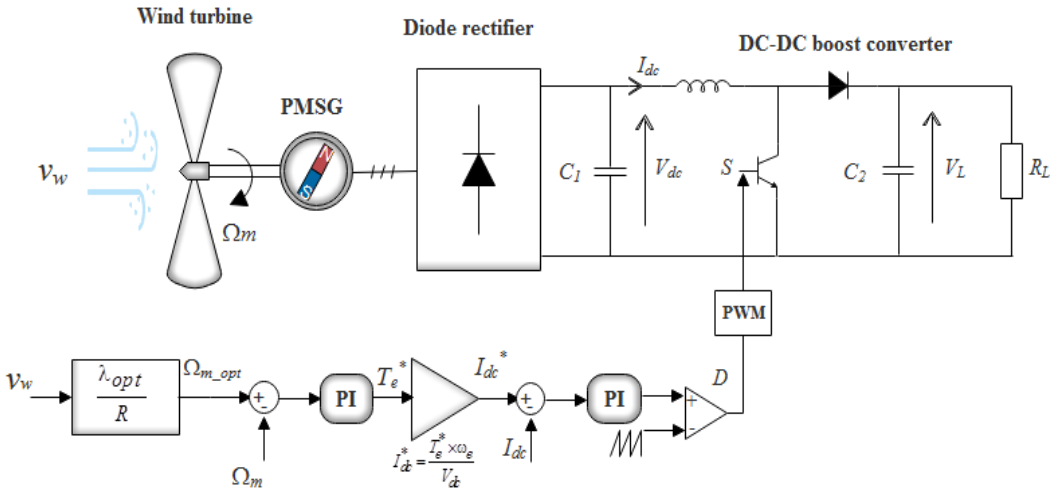

Figure 2. 11. Control of Boost DC-DC Converter with MPPT.

2.8.2 MPPT with Optimal Relation-Based (ORB) $V_{dc}=f(I_{dc})$

This MPPT algorithm depends on numerous optimum relationships, between quantities like wind speed, turbine power output, converter DC voltage, current, power, etc [10, 26, 27], which are all suitable for MPPT control. It has the advantage of not requiring the anemometer, unless there is any need for the lookup table. Nevertheless, to implement the MPPT successfully, a priori relationship needs to be known, which is not easy to determine for real wind energy systems. In this method, a linear equation between the DC-voltage and the DC-current has been proven to be suitable for the MPPT control for wind generation systems equipped with diode rectifiers. This study is very useful to understand the system operation and to optimize the MPPT for the entire operating range [7].

It is considerable to notice that there is a unique optimum value of the λ_{opt} at which the power coefficient is maximum C_{p_max} [28]. If the system operates at the optimal point, the maximum mechanical power expression can be established as follows [29]:

$$P_{m\_\max} = \frac{\rho \pi R^5 C_{p\_\max}}{2\lambda_{opt}^3} \Omega_m^3 = K'_{opt} \Omega_{m\_opt}^3 \tag{2.39}$$

where P_{m_max} is the maximum mechanical power and Ω_{m_opt} is the optimum wind rotor angular velocity corresponding to a specific wind speed.

The torque on the wind turbine shaft can be calculated from the power expression as:

$$T_{m\_\text{opt}} = K_{opt\_T}\Omega_m^2 \tag{2.40}$$

As pointed out in the previous section, the generator will accelerate or decelerate based on the torque difference applied to its input and output as indicated in the equation (2.6). The power electronic interface is current-controlled, which is translated to the torque on the generator side. The MPPT algorithm will continuously change the current command to reach the MPPT. Changing the current, the torque applied to the generator will modify the acceleration properties of the generator. The acceleration information will be projected into the DC-link voltage slope. The higher acceleration/deceleration is, the steeper rate of change of the DC-link voltage (Figure 2.12). the knowledge of the slope of the DC-link voltage, in addition to that of the DC current, can then be used to determine roughly how much electrical torque should be applied to the generator to match the turbine torque and stabilize the system [30]. From that, the relationship between the rotational speed and the rectifier output-voltage can be obtained from equation (2.13), and is expressed as follows:

$$\Omega_m = K_u V_{dc} = \frac{\pi P}{\Phi_m 3\sqrt{3}} V_{dc} \tag{2.41}$$

where $\emptyset_m$ is the flux linkage established by a permanent magnet (Wb), and P is the number of pole pairs.

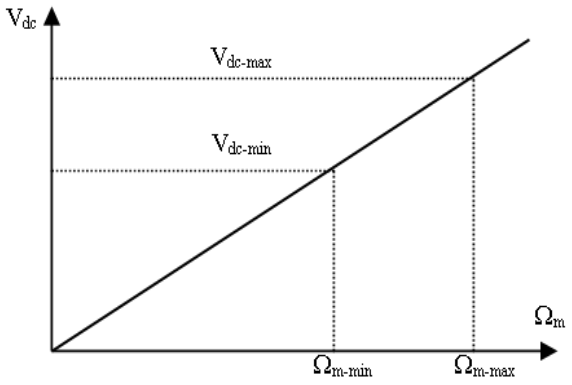

Figure 2. 12. Rectifier output voltage supplying DC/DC boost converter.

The expression of electromagnetic torque can be obtained by substituting equation (2.20) into equation (2.10) as [30]:

$$T_e = \frac{3\sqrt{3}}{\pi} P\phi_m I_{dc} \tag{2.42}$$

The mechanical system can be described by equation (2.43) by neglecting the friction:

$$T_m - T_e = J\frac{d\Omega_m}{dt} \tag{2.43}$$

The relationship between the optimum rectified voltage and the rectified current is obtained by substituting equation (2.40) and (2.41) into equation (2.42):

$$V_{dc\_opt} = \left(\frac{\frac{3\sqrt{3}}{\pi} P\phi_m}{K_u^2 K_{opt-T}} I_{dc} \right)^{1/2} = \left(K_{opt} I_{dc} \right)^{1/2} \tag{2.44}$$

As indicated in equation (2.44), the rectified current I_{dc} is proportional to the square of the rectified voltage V_{dc_opt}. It is clear that if k_{opt} is known by the control action, it is possible to obtain the optimal operating point and to implement the MPPT algorithm efficaciously [31, 32]. The block diagram of this control method can be obtained as displayed in figure 2. 13.

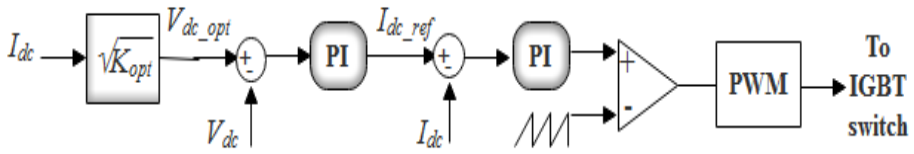

Figure 2. 13. Block diagram of the MPPT control.

2.9 Standard PI control for DC-DC boost converter

In order to get the maximum power from the wind, the variable-speed turbine should run at different speed when the latter changes. The dynamic characteristics of the control system must be properly defined and designed to achieve satisfactory generated power quality and system security, availability and reliability.

Therefore, great attention has to be kept on the theoretical design task so as to assure the correct operation of the control system. The evaluation of PI controller parameters is one of the key issues in the design of a cascaded control structure where the inner loop is designed to achieve fast response and outer one is designed to achieve optimum regulation and stability [33].

2.9.1 PMSG speed loop for the TSR MPPT method

In the TSR method, the MPPT is achieved by the generator side rectifier controller. This is done by adjusting the wind turbine rotor speed (or generator speed) relative to the change in the wind speed. This section presents the design of the PI controller, the control system is trained to find the gain of the regulator by minimizing the overshoot and the tracking error.

As shown in figure 2.14, the actual wind turbine rotor speed Ω_m is compared with the reference rotor speed estimated by the MPPT algorithm in equation (2.36), and the speed error is processed through the PI controller to estimate the reference electromagnetic torque T_e as underneath:

$$T_{e\_ref} = \left(K_p + \frac{K_i}{S} \right) \times \left(\Omega_{m\_ref}(s) - \Omega_m(s) \right) \tag{2.45}$$

where K_p is the proportional gain and K_i is the integral gain.

The closed-loop transfer function is mathematically represented by:

$$\Omega_m(s) = F(s).\Omega_{m\_ref}(s) - P(s).T_m(s) \tag{2.46}$$

where *F(s)* and *P(s)* are given by:

$$F(s) = \frac{K_p s + K_i}{Js^2 + \left(B_m + K_p \right) s + K_i} \tag{2.47}$$

$$P(s) = \frac{s}{Js^2 + \left(B_m + K_p \right) s + K_i} \tag{2.48}$$

where B_m is the damping coefficient and J is the equivalent rotational inertia of the generator. During the steady-state, the static error owing to the external disturbance on the aerodynamic torque T_m has been eliminated by the integral action of the controller. The controlled rotor speed is then expressed as:

$$\Omega_m(s) = F(s) \times \Omega_{m\_ref}(s) \tag{2.49}$$

The parameters K_p and K_i can be estimated using equation (2.50), where ω_n and ξ are respectively the dynamics of the system and the damping factor.

$$\begin{cases} K_i = \omega_n^2 \cdot J \\ K_p = 2 \cdot \xi \cdot \omega_n \cdot J - B_m \end{cases} \tag{2.50}$$

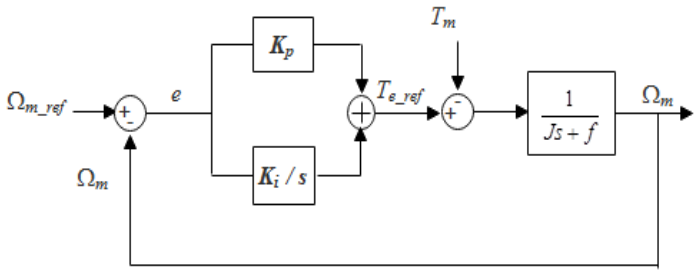

Figure 2. 14. Generator speed control for MPPT.

2.9.2 Voltage control loop for the ORB MPPT method

To ensure the operation point of the MPP, or remaining close to it, this control used a relationship V_{dc}=f(I_{dc}) to find the voltage that supplies the maximum power point and a PI controller to achieve the reference voltage given by the MPPT system. The design of the controller is based on the DC side measurements using a linear model in open-loop.

The PI controller gains are obtained based on the transfer function between the voltage V_{dc} and the DC current taking into account the proportionality expressed in equation (2.41).
From equation (2.41) the following relationship is valid:

$$\frac{dV_{dc}}{dt} \alpha \frac{d\Omega_m}{dt} \tag{2.51}$$

α denote proportionality.

As suggested by equation (2.50), the machine acceleration information is projected onto the DC-link voltage slope change. The voltage slope is used thereupon to detect the wind speed change. Equations (2.43) and (2.51) yield to:

$$\frac{dV_{dc}}{dt} = \frac{T_m - T_e}{J} \tag{2.52}$$

Incorporating (2.5) and (2.42) for the mechanical and electromechanical torque equations and using (2.52) give:

$$\frac{dV_{dc}}{dt} = \frac{1}{K_u J}\left[\frac{1}{2}\rho A \frac{V_w^3}{K_u V_{dc}} C_p - \frac{3\sqrt{3}}{\pi}\phi_m I_{dc}\right] \tag{2.53}$$

From (2.53), the next relation can be deduced:

$$\frac{dV_{dc}}{dt} \alpha \left(-I_{dc}\right) \tag{2.54}$$

α denote proportionality.
By transforming (2.53) in the Laplace domain, it comes:

$$G(s) = \frac{V_{dc}}{I_{dc}} = \frac{1}{K_u J s}\frac{3\sqrt{3}}{\pi}\phi_m \tag{2.55}$$

The block diagram of the DC voltage control can be obtained as displayed in figure 2. 15.

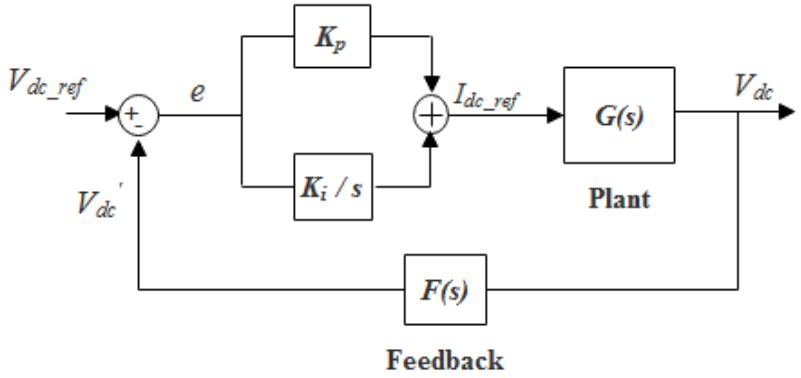

Figure 2. 15. DC Voltage control scheme.

$F(s)$ is the feedback transfer function. In this study, $F(s)$ is assumed to be unity. However, in an actual setup, it has a gain that is determined by the sensor. Besides, $F(s)$ can represent a low pass filter that might be required to suppress the noise of the measured value.

From Figure 2.15, the closed-loop transfer function for the voltage control loop can be presented as:

$$T(s) = \frac{1 + \frac{K_p}{K_i} s}{1 + \frac{K_p}{K_i} s + \frac{K_u J \pi}{3\sqrt{3}\phi_m} s^2} \tag{2.56}$$

PI parameters are calculated from equation (2.56) using the pole placement method as:

$$\begin{cases} K_i = \dfrac{\omega_n^2 K_u J \pi}{3\sqrt{3}\phi_m} \\ K_p = \dfrac{2\xi\omega_n K_u J \pi}{3\sqrt{3}\phi_m} \end{cases} \tag{2.57}$$

2.9.3 Current control loop

The current loop is common for both the MPPT controllers used, where the optimal reference current obtained from the outer loop control is compared with the measured rectified current so that the error is compensated by the PI controller to track the maximum power. The controller generates the pulse ***S*** to drive the switch under the PWM technique. The control loop scheme is shown in figure 2.16.

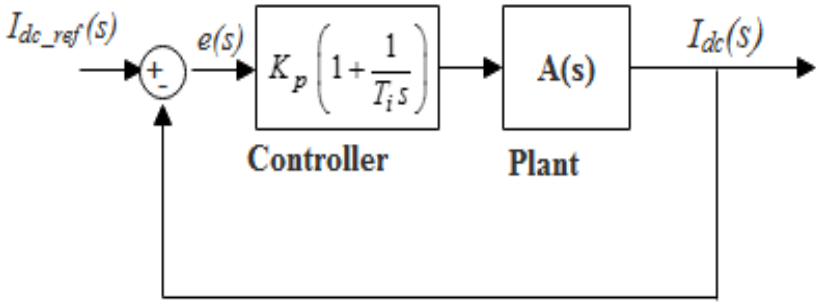

Figure 2. 16. Current control loop structure.

The transfer function of the control loop depicted in Figure 2.16, is formulated as follows:

$$B(s) = K_p\left(1+\frac{1}{T_i s}\right)\times A(s) \tag{2.58}$$

The linearized transfer function between the inductor current and the duty cycle given in [34] is defined by:

$$A(s) = \frac{\hat{I}_{dc}(s)}{\hat{D}} = \frac{2V_{dc}}{R_L(1-D)^2}\,\frac{1+\frac{R_L C}{2}s}{1+\frac{L}{R_L(1-D)^2}s+\frac{LC}{(1-D)^2}s^2} \tag{2.59}$$

where V_{dc}, $R_{L,}$ D, L and C are the output voltage of the boost DC-DC converter, the resistive load, the duty cycle, the inductor and the DC link capacitor, respectively.

The design of the PI controller parameters can be carried out in the frequency domain. The frequency response analysis technique is used to enhance the stability of the closed-loop system. Figure 2.17 shows the bode diagrams of the open-loop plant. The gains of the PI regulator can be tuned graphically using *MATLAB Sisotool software*.

From Figure 2.18, it can be observed that with a phase margin of 56°, the stability criterion of the system is respected. We will thereby limit in this case the crossover frequency to 4000 rad/s to attain satisfactorily, dynamic response and the performance.

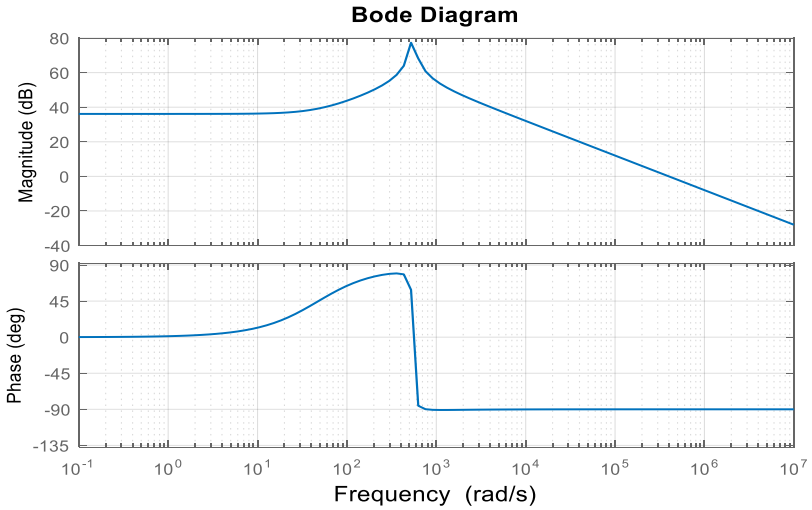

Figure 2. 17. Bode plot for the open-loop system.

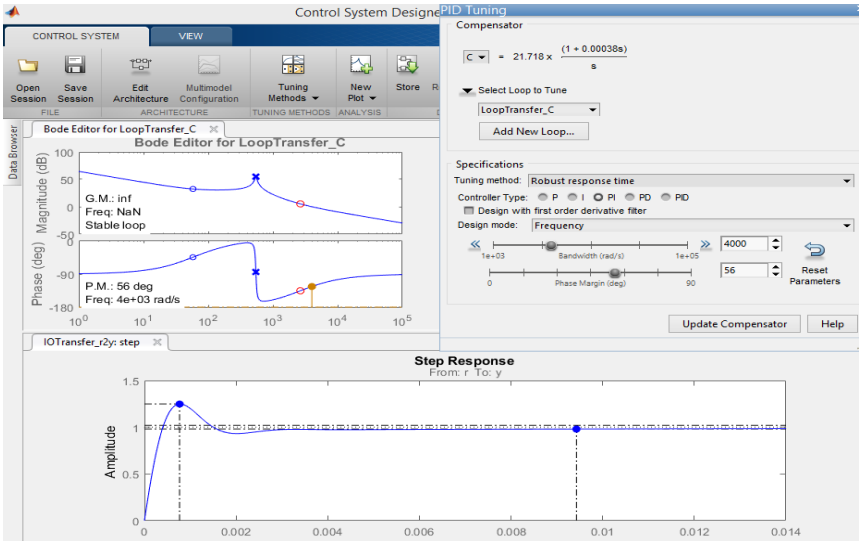

Figure 2. 18. PI tuning of inner current controller.

2.10 Simulation results

For checking the effectiveness of the proposed control strategies, a simple simulation system consisting of a PMSG based on VSWT and DC-DC boost converter is performed using the MATLAB/SimPower Systems environment. Two optimization algorithms namely TSR and ORB are discussed and compared under the variable wind speed profile indicated in figure 2.19. A dual-loop scheme is implemented with two PI blocks to check the tracking ability of the MPPT techniques. The parameters considered for the comparison are the MPPT algorithm efficiency, the power generated by the wind turbine, the steady and dynamic response under changeable wind conditions.

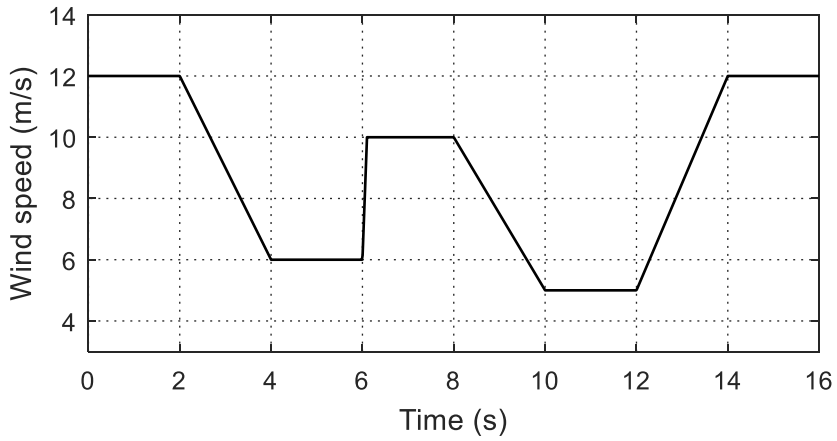

Figure 2. 19. Wind speed profile.

Figure 2.20 shows the speed response of the PMSG for a step change of the wind speed (Figure 2.19). It is observed that the PI controller provides a perfect following of the reference rotor speed and generate the optimum inductor current that extracts the maximum power from the wind turbine.

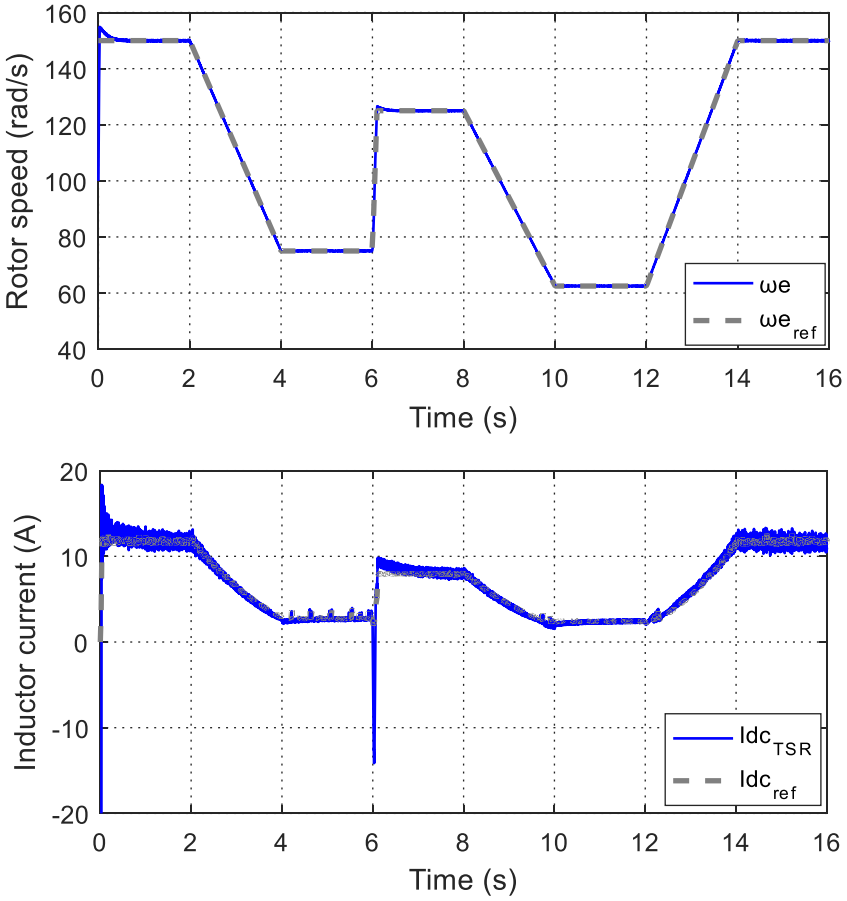

Figure 2. 20. Simulation result of the TSR MPPT algorithm.

Figure 2.21 illustrates the DC side voltage V_{dc} when the system tracks the MPP based on the proposed optimum relationship. This figure shows a good dynamic under variable wind speed. It can be noticed that the PI has a good response and tracks satisfactorily the optimum voltage. In this approach, the rectified voltage is directly related to the optimum rectified current, showing that the DC current is regulated to the desired reference value ensuring correct operation of the selected topology.

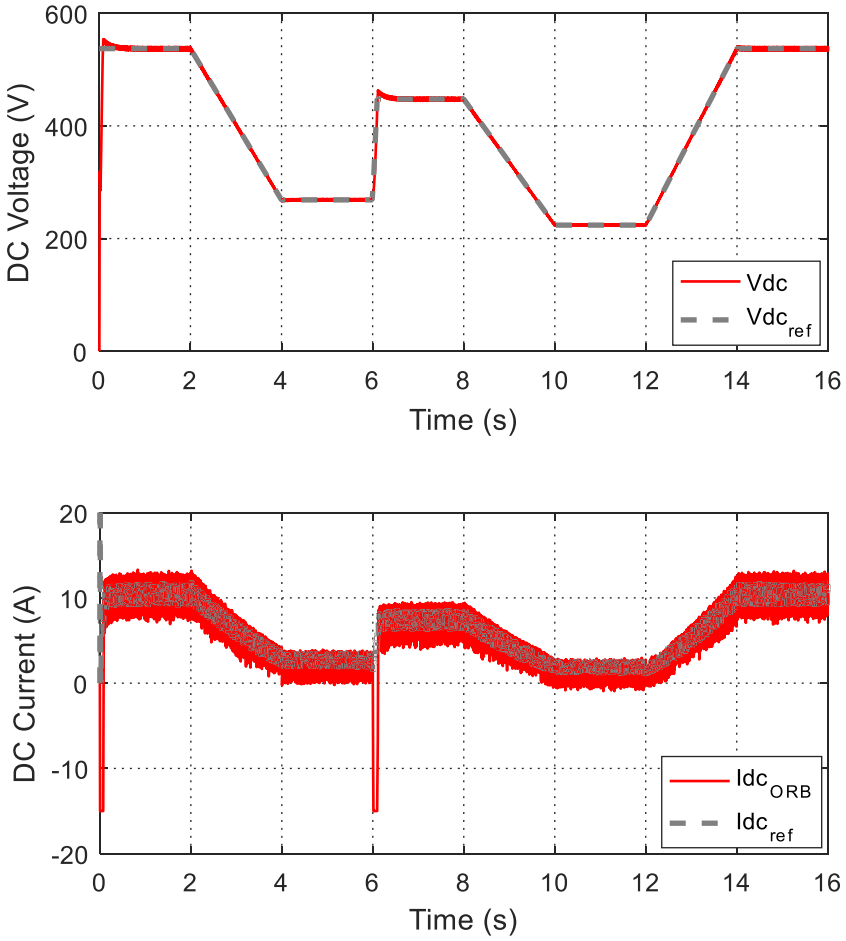

Figure 2. 21. Simulation result of the ORB MPPT algorithm.

Figure 2.22 shows the power coefficient of the two MPPT approaches and that the TSR technique has a good overall efficiency than the ORB method at steady state, C_p only varies in a narrow range, $0.47 < C_p < 0.48$. By contrast, with the ORB method, C_p varies in a wide range.

Figure 2.23 shows the maximum power extraction with TSR and ORB under varying wind speed. It is noticed that there is only little difference in the power extracted for both techniques.

Figure 2.24 shows the captured energy for both methods under the same fluctuating wind speed profile. The extracted electrical energy with the TSR method is 0.3% higher than that of the ORB technique.

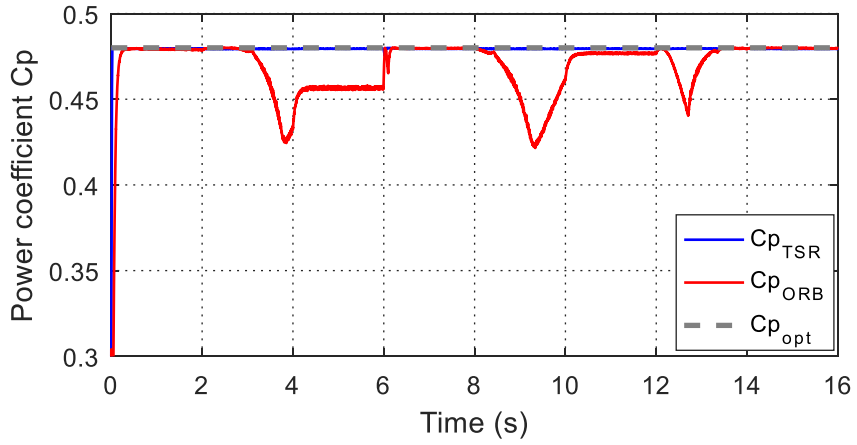

Figure 2. 22. Power coefficient C_p.

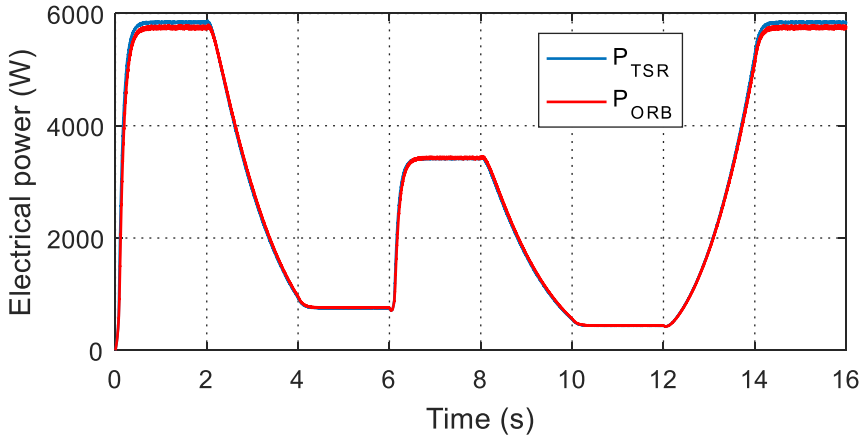

Figure 2. 23. Electrical power P_{dc}.

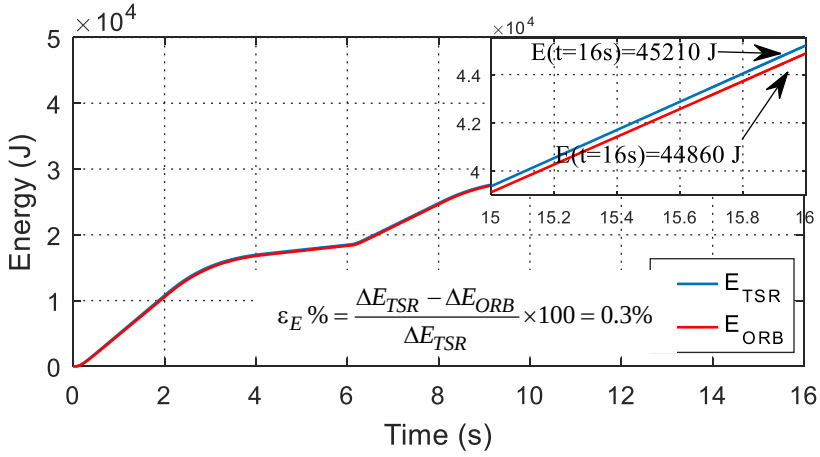

Figure 2. 24. Captured energy under fluctuating wind profile.

2.11 Conclusion

A detailed analysis of a PMSG based standalone wind turbine has been investigated in this chapter. The generator terminals have been connected to the load through the uncontrolled rectifier, the DC-DC boost converter. A dual-loop control scheme with two PI controllers has been proposed to regulate the generator speed and DC voltage under fluctuating wind speed conditions. The overall system performance and control characteristics of the presented generating system has been studied and discussed to operate the WECS around the maximum power for any variations of the wind speed, which can be achieved by adjusting the duty cycle in such a way that the optimal tip speed ratio λ_{opt} is maintained. Two conventional MPPT algorithms were used namely the TSR and the ORB methods, the first is addressed to operate the wind turbine around the maximum power by regulating the rotational speed of the generator, whereas, the second one is used to control the DC side rectifier.

The main aim of the MPPT algorithm is to track the optimum power point of the variable speed wind turbine. Choosing an appropriate MPPT technique is a tough task. In comparison, the TSR algorithm is very simple and fast. It obtained the maximum average value of C_p and maintained it at its maximum even with changes in wind speed. On the other hand, the ORB method is simple and cheaper, but it is less efficient in maximum wind power and difficult to calculate and can vary in real applications.

References

[1] C. Wei, Z. Zhang, W. Qiao, and L. Qu, "An Adaptive Network-Based Reinforcement Learning Method for MPPT Control of PMSG Wind Energy Conversion Systems," IEEE Transactions on Power Electronics, vol. 31, no. 11, pp. 7837–7848, Nov. 2016.

[2] M. E. Haque, M. Negnevitsky, and K. M. Muttaqi, "A Novel Control Strategy for a Variable-Speed Wind Turbine With a Permanent-Magnet Synchronous Generator," IEEE Transactions on Industry Applications, vol. 46, no. 1, pp. 331–339, Jan. 2010.

[3] M. Chowdhury, "Modelling and control of direct drive variable speed wind turbine with Interior Permanent Magnet Synchronous Generator.," p. 221, 2014.

[4] M. Liserre, R. Cardenas, M. Molinas, and J. Rodriguez, "Overview of Multi-MW Wind Turbines and Wind Parks," IEEE Transactions on Industrial Electronics, vol. 58, no. 4, pp. 1081–1095, Apr. 2011.

[5] B. Meghni, D. Dib, and A. T. Azar, "A second-order sliding mode and fuzzy logic control to optimal energy management in wind turbine with battery storage," Neural Comput & Applic, vol. 28, no. 6, pp. 1417–1434, Jun. 2017.

[6] W. Qiao, L. Qu, and R. G. Harley, "Control of IPM Synchronous Generator for Maximum Wind Power Generation Considering Magnetic Saturation," IEEE Transactions on Industry Applications, vol. 45, no. 3, pp. 1095–1105, May 2009.

[7] D. Kumar and K. Chatterjee, "A review of conventional and advanced MPPT algorithms for wind energy systems," Renewable and Sustainable Energy Reviews, vol. 55, pp. 957–970, Mar. 2016.

[8] M. Nasiri, J. Milimonfared, and S. H. Fathi, "Modeling, analysis and comparison of TSR and OTC methods for MPPT and power smoothing in permanent magnet synchronous generator-based wind turbines," Energy Conversion and Management, vol. 86, pp. 892–900, Oct. 2014.

[9] Y. Daili, J.-P. Gaubert, and L. Rahmani, "Implementation of a new maximum power point tracking control strategy for small wind energy conversion systems without mechanical sensors," Energy Conversion and Management, vol. 97, pp. 298–306, Jun. 2015.

[10] H.- Zhang, J. Fletcher, N. Greeves, S. J. Finney, and B. W. Williams, "One-power-point operation for variable speed wind/tidal stream turbines with synchronous generators," IET Renewable Power Generation, vol. 5, no. 1, pp. 99–108, Jan. 2011.

[11] B. Babes, L. Rahmani, A. Chaoui, and N. Hamouda, "Design and Experimental Validation of a Digital Predictive Controller for Variable-Speed Wind Turbine Systems," Journal of Power Electronics (JPE), vol. 17, no. 1, pp. 232–241, 2017.

[12] J. Fortmann, Modeling of Wind Turbines with Doubly Fed Generator System. Springer Vieweg, 2015.

[13] Thomas Ackermann, "Wind Power in Power Systems, 2nd Edition," Book, 2012.

[14] A. Betz, Wind-energie und ihre ausnutzung durch windmühlen. Vandenhoeck, 1926.

[15] M. Aner, "Improved MPPT Dynamics for Starting and Power Extraction of a Small Wind Turbine Employing a PMSG and a VSMC," Thesis, University of Calgary, 2014.

[16] Y. Daili, "Contribution à la commande d'une petite éolienne destinée à l'électrification des sites isolés," Thesis, 2016, sétif.

[17] M. Yin, G. Li, M. Zhou, and C. Zhao, "Modeling of the Wind Turbine with a Permanent Magnet Synchronous Generator for Integration," in 2007 IEEE Power Engineering Society General Meeting, 2007, pp. 1–6.

[18] A. Rolan, A. Luna, G. Vazquez, D. Aguilar, and G. Azevedo, "Modeling of a variable speed wind turbine with a Permanent Magnet Synchronous Generator," in 2009 IEEE International Symposium on Industrial Electronics, 2009, pp. 734–739.

[19] B. Wu, Y. Lang, N. Zargari, and S. Kouro, Power Conversion and Control of Wind Energy Systems. John Wiley & Sons, 2011.

[20] Y. Zou;J. He "Comprehensive modeling, simulation and experimental validation of Permanent Magnet Synchronous generator wind power system", IEEE Conference 2016 in Detroit, MI, USA.

[21] C.-M. Hong, C.-H. Chen, and C.-S. Tu, "Maximum power point tracking-based control algorithm for PMSG wind generation system without mechanical sensors," *Energy Conversion and Management*, vol. 69, pp. 58–67, May 2013.

[22] Z. Alnasir and M. Kazerani, "A small-scale standalone wind energy conversion system featuring SCIG, CSI and a novel storage integration scheme," *Renewable Energy*, vol. 89, pp. 360–370, Apr. 2016.

[23] "D. W. Hart, "Power Electronics", McGraw Hill, Book, 2011 -

[24] M. F. Rahman, L. Zhong, and K. W. Lim, "A direct torque-controlled interior permanent magnet synchronous motor drive incorporating field weakening," *IEEE Transactions on Industry Applications*, vol. 34, no. 6, pp. 1246–1253, Nov. 1998.

[25] M. A. Abdullah, A. H. M. Yatim, C. W. Tan, and R. Saidur, "A review of maximum power point tracking algorithms for wind energy systems," *Renewable and sustainable energy reviews*, vol. 16, no. 5, pp. 3220–3227, 2012.

[26] Y. Xia, K. H. Ahmed, and B. W. Williams, "Wind Turbine Power Coefficient Analysis of a New Maximum Power Point Tracking Technique," *IEEE Transactions on Industrial Electronics*, vol. 60, no. 3, pp. 1122–1132, Mar. 2013.

[27] A. Urtasun, P. Sanchis, I. San Martín, J. López, and L. Marroyo, "Modeling of small wind turbines based on PMSG with diode bridge for sensorless maximum power tracking," *Renewable Energy*, vol. 55, pp. 138–149, Jul. 2013.

[28] K. Kim, Y. Jeung, D. Lee, and H. Kim, "LVRT Scheme of PMSG Wind Power Systems Based on Feedback Linearization," *IEEE Transactions on Power Electronics*, vol. 27, no. 5, pp. 2376–2384, May 2012.

[29] Y. Daili, J.-P. Gaubert, and L. Rahmani, "New control strategy for fast-efficient maximum power point tracking without mechanical sensors applied to small wind energy conversion system," *Journal of Renewable and Sustainable Energy*, vol. 7, no. 4, p. 043102, Jul. 2015.

[30] Z. M. Dalala, Z. U. Zahid, W. Yu, Y. Cho, and J. Lai, "Design and Analysis of an MPPT Technique for Small-Scale Wind Energy Conversion Systems," *IEEE Transactions on Energy Conversion*, vol. 28, no. 3, pp. 756–767, Sep. 2013.

[31] B. Shen, B. Mwinyiwiwa, Y. Zhang, and B. Ooi, "Sensorless Maximum Power Point Tracking of Wind by DFIG Using Rotor Position Phase Lock Loop (PLL)," *IEEE Transactions on Power Electronics*, vol. 24, no. 4, pp. 942–951, Apr. 2009.

[32] C. Liu and Y. Hsu, "Effect of Rotor Excitation Voltage on Steady-State Stability and Maximum Output Power of a Doubly Fed Induction Generator," *IEEE Transactions on Industrial Electronics*, vol. 58, no. 4, pp. 1096–1109, Apr. 2011.

[33] I. Munteanu, A. I. Bratcu, N.-A. Cutululis, and E. Ceanga, *Optimal Control of Wind Energy Systems: Towards a Global Approach*. Springer Science & Business Media, 2008.

[34] N. Maherzi, Conservatoire national des arts et métiers (France), and Centre régional (Rhône-Alpes), "Etude, conception et réalisation d'un convertisseur d'énergie DC/DC associé à des supercondensateurs," [s.n.], S.l., 2010.

Chapter 3 Fuzzy maximum power point extraction for a standalone wind energy conversion system

3.1 Introduction

As previously explained, MPPT algorithms are necessary to operate the WECS around the maximum power. Several control strategies (MPPTs) can be used for energy conversion. If the wind-turbine characteristic $C_p(\lambda)$ is supposed to be a priori known, it can be used for an optimum relationship to implement the MPPT process. On the contrary, if this characteristic is unknown, an operational seeking algorithm such as Fuzzy Logic (FL) has to be implemented [1, 2].

FL based control systems provide a much-improved performance to operate the wind system under maximum power point in fast-changing environmental conditions and uncertainties [3]. The core interest of FLCs is their ability to incorporate experience, intuition and heuristics into the system instead of relying on mathematical models, making them more effective in power system applications where existing models are ill-defined and not reliable enough [4].

FLCs are suitable for wind systems characterized by high nonlinearity, input fluctuation, and environmental variations. However, a FLC has a high computational burden during hardware and software implementation involving power processors especially with a significant number of fuzzy logic inputs raising the dimension of the rule base [5]. Despite these drawbacks, FL still stays more effective and robust than the conventional methods.

The purpose of this chapter is to develop a fuzzy maximum power point tracking algorithm for small wind energy conversion systems. A comparison has been made between the performance of the different MPPT algorithms (conventional and FLC) based on complexity, wind speed requirement, prior training, and the ability to acquire the maximal energy output. The analysis is based on simulations on MATLAB/Simpower system environment.

3.2 Fuzzy control processor

FL concept was introduced in 1965 with the proposal of fuzzy set theory by Lotfi A. Zadeh [6]. FLCs based on fuzzy set theory are used to represent the experience and

knowledge of a human operator in terms of linguistic variables called fuzzy rules. Since an experienced human operator adjusts the system inputs to get the desired output by just looking at the system output without any knowledge of the system's dynamics and interior parameter variations, the implementation of linguistic fuzzy rules based on the procedures done by human operators does not also require a mathematical model of the system. Therefore, a FLC becomes nonlinear and adaptive in nature having a robust performance under parameter variations with the ability to get desired control actions for complex, uncertain and nonlinear systems without the requirement of their mathematical models and parameter estimation [7, 9]. FL-based controllers provide a mathematical foundation for approximate reasoning, which has been proven to be very successful in a variety of applications [7, 10, 12].

In engineering, FL and reasoning algorithms are used in control, systems identification, modeling, decision-making, management and many other similar applications related to industrial developments and management. Known fuzzy reasoning algorithms such as Mamdani fuzzy reasoning, Sugeno fuzzy reasoning, and steps toward FLCs are given hereafter.

3.2.1 Mamdani Fuzzy reasoning

After the introduction of the FL concept by Lotfi A. Zadeh, Mamdani and his colleagues developed and used a FLC in a hydraulic pressure system [10, 12]. Mamdani reasoning algorithm is very suitable to be used in FLC systems. Figure 3.1 shows the block diagram of a typical FLC based Mamdani fuzzy reasoning algorithm. The crisp inputs $x \in X$ and $y \in Y$ in Mamdani fuzzy reasoning are mapped from crisp input universes X and Y into fuzzy input universe in terms of fuzzy membership values $\mu_i(x)$ and $\mu_j(y)$, where i and j are the number of fuzzy sets in which x and y have nonzero membership degrees. After the rule processing in the rule base, the fuzzy outputs from each rule are obtained and combined in the reasoning stage of output universe Z. The crisp output is then obtained by applying a process called defuzzification, which is usually an averaging math function. These stages will be explained in detail next.

a. Fuzzification

As shown in Figure 3.1, the fuzzy processor uses the error $e(k)$ and its change $de(k)$ as two crisp inputs and converts them to fuzzy membership values in the fuzzifier. These two inputs are defined as in (3.1):

$$\begin{cases} e(k) = r(k) - y(k) \\ de(k) = e(k) - e(k-1) \end{cases} \tag{3.1}$$

where e(k) is the difference between the reference signal $r(k)$ and the output signal $y(k)$.

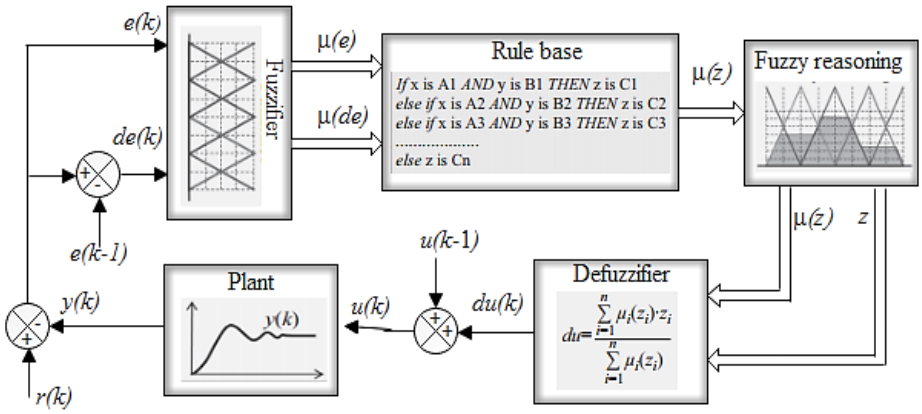

Figure 3. 1. Structure of **FLC**.

b. Fuzzy rule base

The fuzzy rule base is the brain of fuzzy reasoning algorithms. The rules represent the operational behavior of a system, decision process, and thoughts of an expert. Therefore, the construction of a rule base system is very important to get the correct decision. Therefore, experts' ideas, knowledge, intuitions, and tricks are included in a decision process, and in the rule base. There isn't a direct method to drive the rules. However, some works have been done to complete the rules after having some initial rules. Rule construction processes are given next to show a way of constructing the rules.

c. Fuzzy rules: the modeling of thoughts

The fuzzy rule base, which may also be called the fuzzy decision table, is the unit mapping two crisp inputs, $e(k)$ and $de(k)$ to the fuzzy output space defined on the universe of $du(k)$. The fuzzy rules represent the knowledge and abilities of a human operator who makes necessary adjustments to operate the system with minimum error and fast response. In order to model the actions that a human operator would decide whether the change, $du(k)$, at the output of the fuzzy processor should increase or decrease the control signal according to the error $e(k)$ and its change $de(k)$. It is necessary to observe the behavior of the error signal $e(k)$ and its change $de(k)$ on different operating regions, as shown by the Roman numbers in Figure 3.2. The output $du(k)$ from the FLC is the change that is required to increase or

decrease the overall control action to the controlled system. Therefore, the signs of $e(k)$ and $de(k)$ are used to determine the signs of $du(k)$, which determines whether the overall control signal is to be increased. The sign of $du(k)$ should be positive if $u(k)$ is required to be increased and it should be negative otherwise.

Step input responses of reference $r(k)$, actual system output $y(k)$, control error $e(k)$ and change in error $de(k)$ are given in Figure 3.2 for an oscillatory second-order system. Since the magnitude of the error change $de(k)$ is much smaller than $e(k)$ and the others, it was multiplied by ten so as to make it visible in the figure. Now, let us look at closely to each region and see what an operator is supposed to do to have a zero steady-state error.

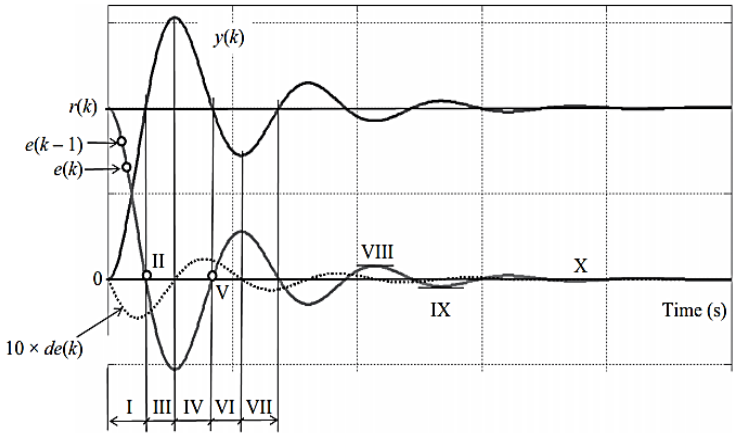

Figure 3. 2. Operating regions of error and error change.

At region I: The error $e(k)$ is positive and its change $de(k)$ is negative, meaning that the error is decreasing towards zero. Therefore, the control input $u(k)$ should be increased so that the decrement of the error toward zero becomes faster. $du(k)$ should remain positive to increase the value of $u(k)$.

At region II*:* $e(k)$ is zero and $de(k)$ is negative. This means that the control signal $u(k)$ is higher than the required value and must be reduced. Otherwise, the error will be negative and continue to get away from zero. The error becomes negative when the output $y(k)$ becomes greater than the reference $r(k)$. Therefore, the control input $u(k)$ should be reduced by generating a negative $du(k)$.

At region III: Both $e(k)$ and $de(k)$ are negative. The error is negative and continues to be more negative. This means that the overshoot is increasing. Something must be done to reduce the control signal $u(k)$ so that the overshoot and error will be smaller or brought to zero. Therefore, $du(k)$ must have a negative sign.

At region IV: $e(k)$ is negative and $de(k)$ is positive. The error is still negative, but getting toward zero because of positive $de(k)$. The overshoot is also decreasing. In order to make this decrement faster, the control signal $u(k)$ should be reduced again. Therefore, $du(k)$ is kept negative.

At region V: $e(k)$ is zero and $de(k)$ is positive. This means that the control signal $u(k)$ is smaller than the required value and must be increased. Otherwise, the error will be positive and keeps increasing in the positive direction. The error continues to be positive with larger magnitude and the output $y(k)$ becomes smaller than the reference $r(k)$. Therefore, control input $u(k)$ should be increased by generating a positive $du(k)$.

At region VI: Both $e(k)$ and $de(k)$ are positive. The error is positive and increases in the positive direction. This means that the output $y(k)$ is under the reference $r(k)$ and needs to be increased. The control signal $u(k)$ must be increased to increase $y(k)$ so that the error will be smaller or brought to zero. Therefore, $du(k)$ must be positive.

At region VII: This is a repeat of region I with smaller magnitudes.

At region VIII: $e(k)$ is positive and $de(k)$ is zero. The error is positive and constant since there is no change. This means that the oscillations are over or very small. However, the output is smaller than the reference and control signal $u(k)$ needs to be increased. Therefore, a positive value for $du(k)$ should be assigned.

At region IX: $e(k)$ is negative and $de(k)$ is zero. The error is negative and constant since there is no change. This means that the oscillations are over or very small. However, the output is greater than the reference and control signal $u(k)$ needs to be reduced. Therefore, a negative value for $du(k)$ should be assigned to decrease the error.

At region X: Both $e(k)$ and $de(k)$ are zero. The error is zero and not changing anymore. Therefore, $du(k)$ is set to zero since no change is required for the control signal $u(k)$.

Representing the input crisp variables $e(k)$ and $de(k)$ by three fuzzy sets, negative (N), zero (Z) and positive (P), means that these input spaces are partitioned into three fuzzy regions each yielding a fuzzy output space with nine rules maximum. A nine-rule fuzzy decision table may be sufficient for some applications. However, many applications require

more rules than nine. In order to construct a fuzzy rule decision table with more than nine rules, the input spaces must be partitioned into more than three regions each. For example, the linguistic variable negative can be partitioned into subcategories as negative small (NS) and negative big (NB). Similarly, the term *positive* can have subcategories as positive small (PS) and positive big (PB). Using the subset zero (ZE) besides these four subsets, there will be five fuzzy subsets defined in the universes of $e(k)$ and $de(k)$. Therefore, a 5x5 decision space is obtained for $du(k)$ at the output, which can be extended to a 49-rule table by adding fuzzy subsets negative medium (NM) and positive medium (PM) into negative and positive sections of $e(k)$ and $de(k)$.

A very fine subdivision of the input universes on more than seven fuzzy sets generally does not improve the behavior of the dynamics of the system to be regulated.

d. The input-output interaction

A plot of $e(k)$ versus $de(k)$ makes it easy to see the variation space of these variables. Therefore, a FLC designer can see and define the boundaries of the variables. The definitions of the boundaries are very important to select a working area in the input space so that the sparsity is minimized and operations are focused on the active areas of the input universes. Such a plot of $e(k)$ versus $de(k)$ for a second-order oscillatory system is shown in Figure 3.3, where each one of the universes of $e(k)$ and $de(k)$ is partitioned into three regions as negative (N), zero (Z) and positive (P). The usable area in Figure 3.3 is shown by the shaded area. Triangular-type membership functions are used for partitioning the crisp universes into fuzzy subsets. Different membership functions such as Gaussian, trapezoidal and bell could have also been used. Each one of these membership functions has its own effects on the FLC output [13]. However, triangular membership functions are more convenient for expressing the concept because its linearity makes it easier to intercept membership degrees from a triangle.

e. Fuzzy conclusion

The reasoning section of the fuzzy processor combines the individual consequents to a general fuzzy conclusion of the process.

f. Defuzzification

Defuzzification is done in order to convert the fuzzy conclusion into a crisp value. Defuzzification may be explained as the extraction of a single crisp value from an area that is

representing the fuzzy conclusion of a fuzzy reasoning process. The most known defuzzification methods are listed below.

- Lower maximum (LM)
- Upper maximum (UM)
- Mean of maxima (MOM)
- Equal areas (EA)
- Center of areas (COAs)
- Center of gravity (COG)

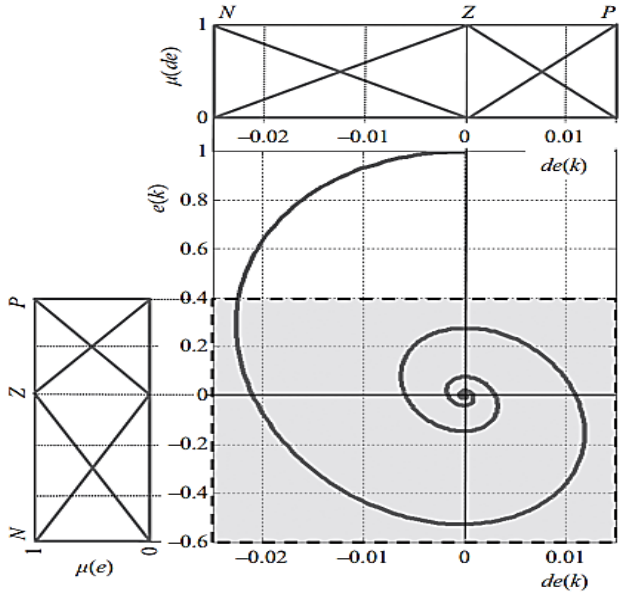

Figure 3. 3. Input space of an FLC from the system response.

The COA method is the most used one in fuzzy logic control applications [14]. In this method, the crisp output is the point that corresponds to the COAs that are obtained as the union of the areas from individual rules. The defuzzification is done using the formula given in equation (3.2):

$$Z_{COA} = \frac{\sum_{i=1}^{n} w_{Ri} \cdot Z_i}{\sum_{i=1}^{n} w_{Ri}} \tag{3.2}$$

where n is the number of the active rules, $w_{Ri}(z)$ is the weighting factor from the i^{th} rule, z_i is the crisp value defined in the output universe and corresponds to the center of the core set of the output fuzzy set.

The fuzzy processor uses the Mamdani fuzzy reasoning method from the inputs $e(k)$ and $de(k)$ to the output $du(k)$. Depending on the magnitude of the control signal $u(k)$, the actuator

adjusts the power or energy input to the physical system to be controlled so that the system output tracks the reference. The fuzzy processor, summers, and the physical system altogether are called the FLC system, and the process result in the control signal $u(t)$ is called the FLC.

3.2.2 Takagi–Sugeno (TS) fuzzy reasoning

Takagi and Sugeno have developed the TS fuzzy model for system identification and modeling based on input-output data [15]. TS fuzzy modeling can be used to represent complex nonlinear systems by fuzzy rules that have linear crisp equations as the consequents [16]. This fuzzy approach is widely used in system modeling and identifications [17, 20]. The use of TS fuzzy modeling approach as a fuzzy reasoning method is explained in [21]. The general structure of the fuzzy rules in this method is written as in equation (3.3):

If x is A and y is B then z is f(x,y) (3.3)

where A and B are fuzzy subsets defined in the universes X and Y, respectively. When compared with the rules in the Mamdani fuzzy reasoning method, it is seen that only the output space is different in equation (3.3). The output space in TS fuzzy reasoning does not include fuzzy subsets. A crisp function $f(x,y)$ is used to find a crisp output for each rule. The crisp output function is usually defined in terms of crisp input variables x and y, and written as:

$$z_i = f(x, y) \tag{3.4}$$

where i is the active rule number. After calculating a crisp output z_i for each active rule, the final crisp output is obtained as a weighted sum of the crisp outputs as:

$$z = \sum_{i=1}^{N} w_{Ri} \cdot z_i \tag{3.5}$$

where

$$\sum_{i=1}^{N} w_{Ri} \cong 1 \tag{3.6}$$

where N is the total number of the rules or active rules, w_{Ri} is the weighting factor obtained from the i^{th} rule and z_i is given in (3.4). The values of w_{Ri} are obtained as the process of the rule base system using the operator *min* or arithmetic *product*, which makes the output to be equal or smaller than the inputs. Therefore, (3.6) is expected to be satisfied, otherwise, if the sum of the weighting factors is much greater than one, the fuzziness of the process weakens. Since the outputs from individual rules are not fuzzy, a defuzzification is not required in the TS fuzzy reasoning and (3.5) is used. However, in some applications, if (3.6) is not

approximately satisfied, then the final crisp output is obtained as a weighted average similar to the COA method given by (3.2).

3.3 Fuzzy-based maximum power extraction algorithm

In this section, two fuzzy-based MPPT methods are designed for controlling the IGBT switch of the DC-DC boost converter. According to the power measurement, the MPPT algorithms are categorized into maximum aerodynamic power tracking (MAPT) and maximum electrical power tracking (MEPT). Both algorithms are simple in structure, low cost and have a good response to wind speed variations [22]. The schematic diagram of the standalone WECS including the proposed fuzzy-based MPPT algorithms is shown in Figure 3.4.

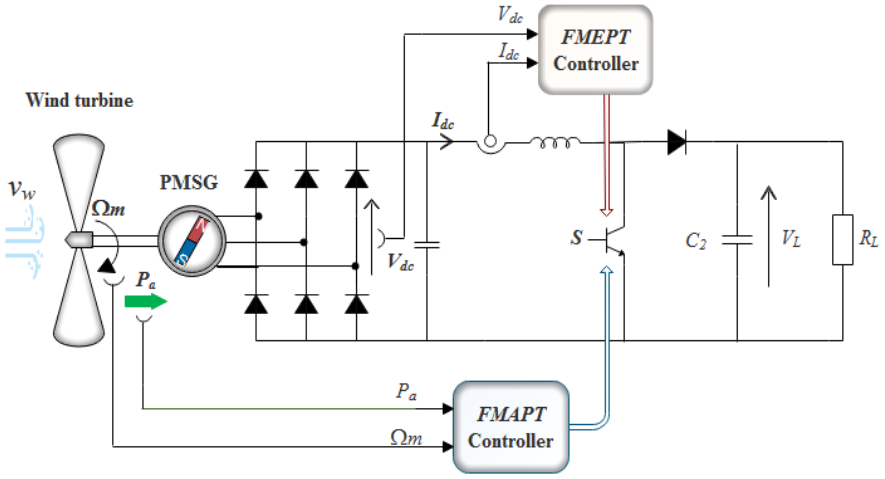

Figure 3. 4. Schematic diagram of the SWECS including the proposed Fuzzy MPPT.

3.3.1 Fuzzy based-MAPT

To track an optimal rotor speed reference, without measuring the wind speed and without the knowledge of the turbine characteristics, a control which is based on FLC is introduced to determine the operating point corresponding to the maximum power for wind turbine system. The proposed FLC is based on the behavioral rules linked to power and rotor speed variations. Figure 3.5 gives an example of a track in the $P(\Omega)$ plan for a constant wind speed.

The power variation (ΔP) is either in the positive direction or in the negative one. The value of ΔP can also be small or on the contrary large. This control allows the research of the optimum point while being based on the expert observations. From these judgments, the

reference rotational speed variation (ΔΩ) is increased or decreased in a small or large way in the direction which makes it possible to increase the power *P* [23].

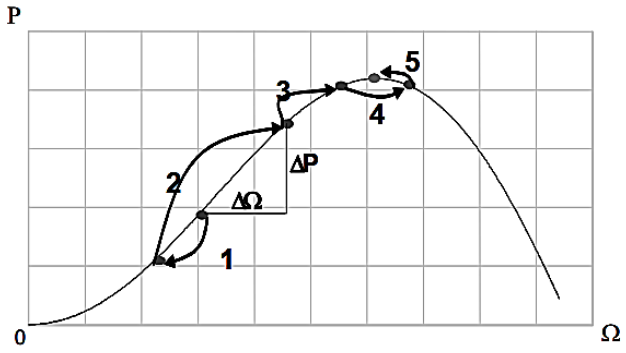

Figure 3. 5. Operating principle of the Fuzzy MPPT for a constant wind speed.

when the wind speed varies, the same types of rules are applied to track the maximum power point as shown in Figure 3.6.

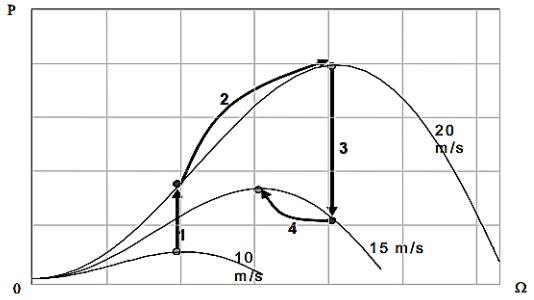

Figure 3. 6. Operating principle of the Fuzzy MPPT for a sudden change in wind speed.

The structure of the proposed fuzzy logic controller is shown in Figure 3.7. The MPPT algorithm contains the measurement of the variations of wind power $\Delta \hat{P}_a$ and the variation of rotational speed $\Delta\Omega_m$ and proposes a variation of the speed reference $\Delta\Omega_{m\_ref}$. These variables are normalized by the scaling factors K_1, K_2, K_3 and updated using the following equations:

$$\begin{cases} \Delta \hat{P}a = K_1\left(\hat{P}a\left[k\right]-\hat{P}a\left[k-1\right]\right) \\ \Delta\Omega_m = K_2\left(\Omega_m\left[k\right]-\Omega_m\left[k-1\right]\right) \\ \Omega_{m\_ref}\left[k\right] = K_3\left(\Omega_m\left[k-1\right]+\Delta\Omega_{m\_ref}\left[k\right]\right) \end{cases} \quad (3.7)$$

FLC speed input can be measured by the rotor speed sensors, whereas the aerodynamic power is estimated, the raison being that $\hat{P}_a$ cannot be measured directly [24]. Hence, the electrical power (V_{dc}, I_{dc}) and the various losses (electrical or mechanical) are measured and then the aerodynamic power captured by the wind turbine is deduced. All losses in the converters and in the filter are neglected, only mechanical losses ($p_{loss\text{-}m}$) and Joule losses ($p_{loss\text{-}J}$) of the PMSG are taken into account [25]. The aerodynamic power is estimated with the hereunder equation:

$$\hat{P}_a = P_{dc} + p_{loss-J} + p_{loss-m} \tag{3.8}$$

with:

$$\begin{cases} p_{loss-J} = 3R_s I_s^2 \\ p_{loss-m} = f\Omega_m^2 \end{cases} \tag{3.9}$$

where

R_s: is the electrical phase resistance,

I_s: is the phase current,

B_m: is the damping coefficient.

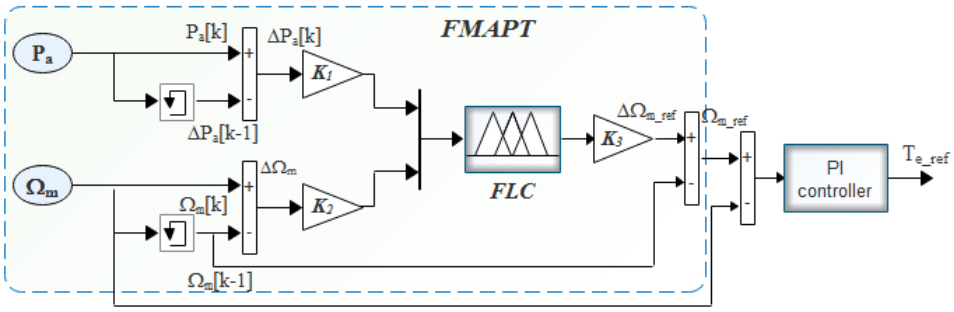

Figure 3. 7. Block diagram of the proposed FMAPT controller.

The FLC block includes three functional blocks: fuzzification, fuzzy rule algorithm, and defuzzification. Figure 3.8 shows the membership functions of the input and output variables in which the membership functions of input variables $\Delta\hat{P}_a$ and $\Delta\Omega_m$ are triangular and have seven fuzzy subsets. Seven fuzzy subsets are also considered for membership functions of the output variable $\Delta\Omega_{m\_ref.}$ These input and output variables are expressed in terms of linguistic variables such as **PB** (Positive Big), **PM** (Positive Medium), **PS** (Positive Small), **Z** (Zero), **NB** (Negative Big), **NM** (Negative Medium), and **NS** (Negative Small)).

The control rules are indicated in Table 3.1 with $\Delta \hat{P}_a$ and $\Delta\Omega_m$ as inputs and $\Delta\Omega_{m\_ref}$ as the output. The fuzzy inference is carried out by using Sugeno's method [26], and the defuzzification uses the center of gravity to compute the output of this FLC as indicated in equation (3.10).

$$\Delta\Omega_{m-opt}[k] = \frac{\sum_{i=1}^{n} \mu\left(\Delta\Omega_{m-opt_i}\right) \times \Delta\Omega_{m-opt_i}}{\sum_{i=1}^{n} \mu\left(\Delta\Omega_{m-opt_i}\right)} \tag{3.10}$$

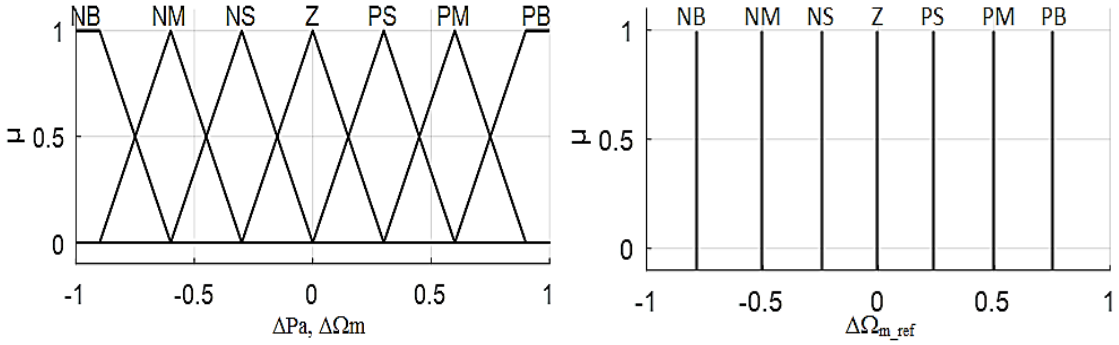

Figure 3. 8. Inputs/Output membership functions of the FMAPT algorithm.

Table 3. 1 Set of fuzzy rules**.**

$\Delta\Omega_m/\Delta$Pa	NB	NM	NS	Z	PS	PM	PB
NB	PB	PB	NM	Z	NM	NB	NB
NM	PB	PM	PS	Z	NS	NM	NB
NS	PM	PS	PS	Z	NS	NS	NM
Z	NB	NM	NS	Z	PS	PM	PB
NS	NM	NS	NS	Z	PS	PS	PM
NM	NB	NM	NS	Z	PS	PM	PB
NB	NB	NB	NM	Z	PM	PB	PB

In accordance with Table 3.1, the fuzzy MPPT rules are given in the forms of the verbal statements below [27]:

1- If a great increase in the rotor speed (Ω_m) involves a great increase in the power ($\hat{P}_a$), then we continue to strongly increase the reference speed (Ω_{m_ref}).

2- If a great increase in the rotor speed (Ω_m) involves a great reduction in the power $\hat{P}_a$, then the reference speed (Ω_{m_ref}) has to be diminished to obtain a fast increase in the power $\hat{P}_a$.

3- If a great increase in the rotor speed (Ω_m) involves a weak increase in the power(we get closer to the optimal reference speed), then we increase moderately the reference speed (Ω_{m_ref}) (the beginning of stabilization).

4- If a small reduction in the rotor speed involves an average increase in the power, then the reference speed has to be slightly decreased so as to achieve the maximum power point more quickly.

5- If any increase or decrease involves zero power change, then the control variable (Ω_{m_ref}) should remain the same.

6- If a zero change of the rotor speed involves an increase in the power, which indicates that the wind speed increased, then the reference speed should increase to get closer to the new optimal speed.

7- If a zero change of the rotor speed involves a decrease in the power, which indicates that the wind speed decreased, then the reference speed should decrease.

As shown in Figure 3, FLC optimizes the reference speed Ω_{m_ref} for maximum power tracking. This value represents a positive input for the *PI* controller, which performs the speed control in steady-state. The PI loop operates with a fast rate and provides fast response and overall system stability.

3.3.2 Fuzzy based-MEPT

The main objective of this section is to drive the optimum DC- voltage corresponding to the maximum electrical power without any knowledge of the wind turbine characteristics. A fuzzy-based MEPT algorithm is developed in order to converge toward the optimal point. The main advantage of this method is that it requires neither wind velocity sensors nor rotor speed sensors. The proposed FLC structure is shown in Figure 3.9 where the electrical power (P_{dc}) and the DC voltage (V_{dc}) variations are selected as the two input variables for the FLC. The output is the change of the optimum DC voltage (ΔV_{dc_ref}), these variables are normalized by the scaling factors and updated according to equation 3.11.

$$\begin{cases} \Delta P_{dc}[k] = K_1 \left(P_{dc}[k] - P_{dc}[k-1] \right) \\ \Delta V_{dc}[k] = K_2 \left(V_{dc}[k] - V_{dc}[k-1] \right) \\ V_{dc\_ref}[k] = K_3 \left(V_{dc}[k-1] + \Delta V_{dc\_ref}[k] \right) \end{cases} \tag{3.11}$$

where ΔP_{dc}[k] and ΔV_{dc}[k] denote the electrical DC power and rectified voltage variations, respectively, V_{dc}[k] is the optimum rectified voltage.

Gains known as "scale factors" (K_1, K_2, K_3) are present in the fuzzy controller inputs and output variables making it possible to change the sensitivity of the controller without changing its structure.

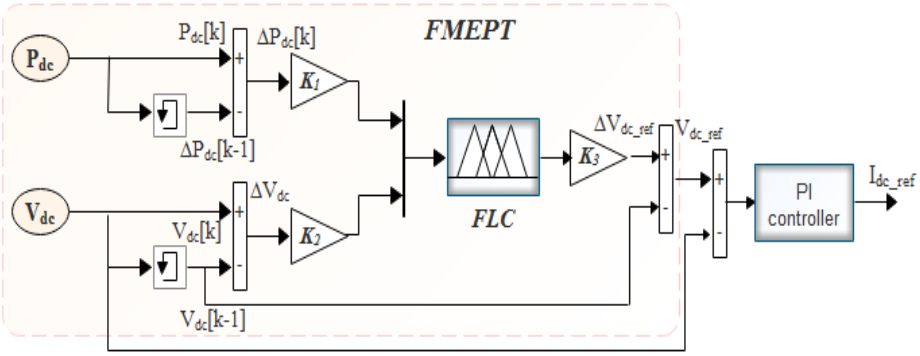

Figure 3. 9. Block diagram of the proposed *FMEPT* controller.

The FLC used in this algorithm is the Mamdani-Type fuzzy inference system. As illustrated in Figure 3.10, the membership functions for the input and output variables are triangular and trapezoidal and have seven fuzzy subsets, namely: **PB** (Positive Big), **PM** (Positive Medium), **PS** (Positive Small), **Z** (Zero), **NB** (Negative Big), **NM** (Negative Medium), and **NS** (Negative Small) [28].

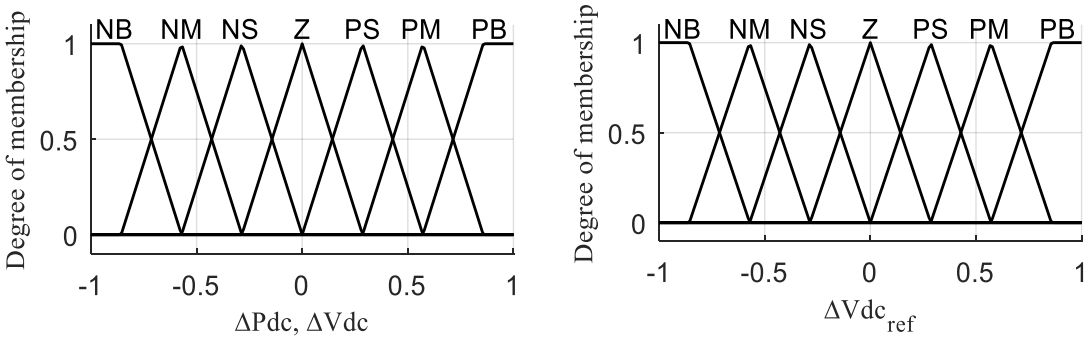

Figure 3. 10. Inputs/Output membership functions of the FMEPT algorithm.

49 fuzzy rules are considered in this design, which are shown in Table 3.2. Crisp input signals are first mapped to linguistic values, and then combined based on all the rules by using

the maximum aggregation method "sum" [11]. Finally, the defuzzification is performed using the COA of final combined fuzzy set in order to obtain the change of the optimum rectified voltage.

As explained previously, the MPPT technique takes measurement of the DC voltage and current, and then uses FLC to calculate the reference voltage (V_{dc_ref}). Then, there is another control loop where PI controller regulates the input voltage of converter. Its task is to minimize the error between V_{dc_ref} and the measured DC voltage (V_{dc}). The PI loop operates with a much faster rate and provides a fast response and the overall system stability [29].

Table 3. 2 Fuzzy control rules.

$\Delta V_{dc}/\Delta P_{dc}$	NB	NM	NS	Z	PS	PM	PB
NB	PB	PM	PM	NM	NM	NM	NB
NM	PB	PM	PS	NM	NS	NM	NB
NS	PB	PM	PS	NS	NS	NM	NB
Z	Z	Z	Z	Z	Z	Z	Z
NS	NM	NS	NS	PS	PS	PS	PM
NM	NB	NM	NS	PM	PS	PM	PB
NB	NB	NM	NM	PB	PM	PM	PB

3.4 Results and discussion

The simulation has been carried out through MATLAB/Simpower system software to prove the effectiveness of the proposed algorithms. The main objective is to show the capability of the proposed algorithm to track the maximum power point compared with the conventional approach presented in chapter 2 for the same proposed system configuration and parameters.

Figure 3.12 illustrates the simulation results of both algorithms; the conventional algorithm based on the TSR approach and the fuzzy MAPT algorithm under the simulated wind speed profile shown in Figure 3.11. The comparison has been done by observing optimal rotor speed and inductor current waveforms that supply the maximum power point. It can be seen that the system reacts perfectly under a rapid variation of the wind speed and also that the fuzzy algorithm successfully detects the wind speed variation.

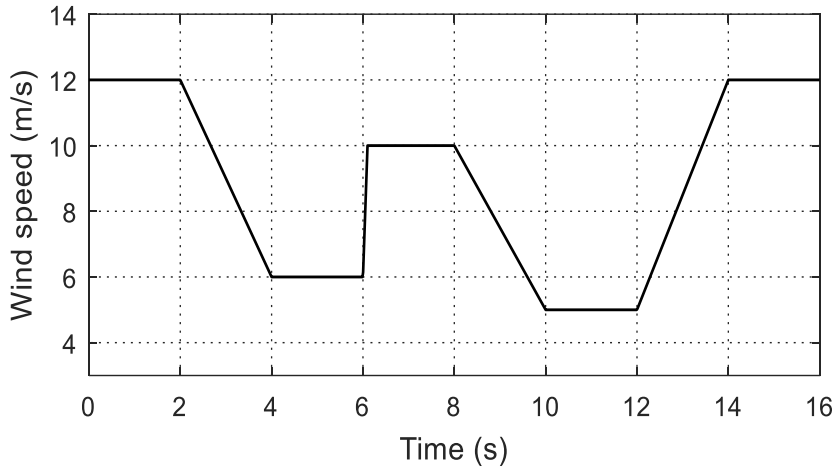

Figure 3. 11. Wind speed profile.

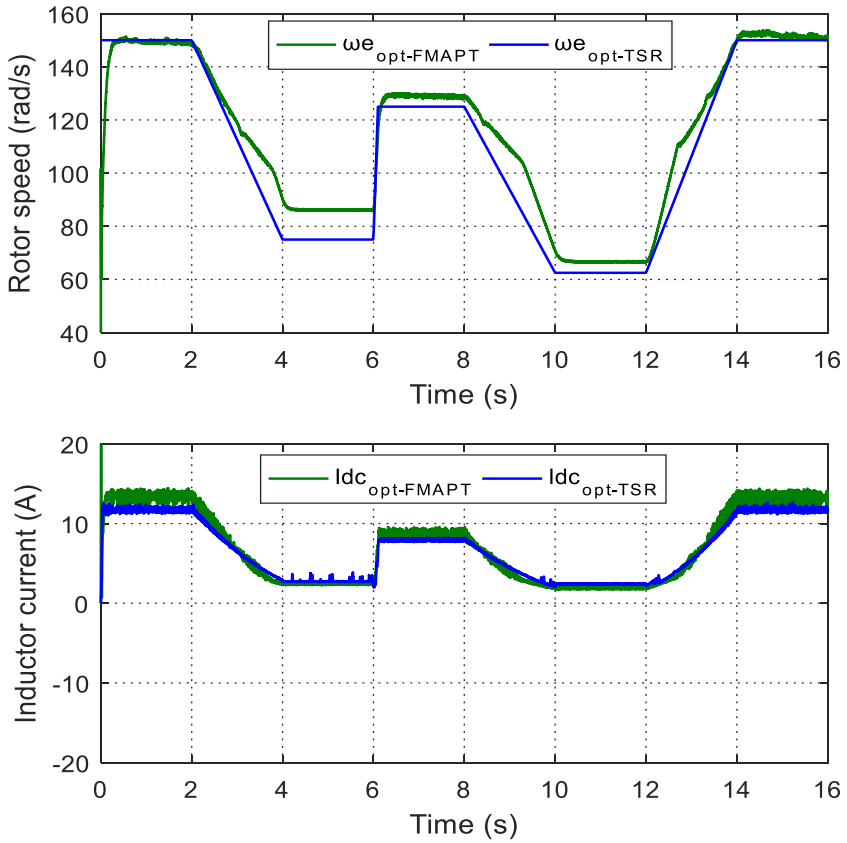

Figure 3. 12. Simulation result of the FMAPT algorithm.

As can be observed from Figure 3.12, with the proposed fuzzy approach, the optimal generator speed changes to a new optimal value. Likewise, the optimum DC current tracking control can be better maintained by using the proposed control strategy as compared with the conventional method, and hence the maximum power point tracking control can be better achieved by using the proposed control strategy.

As shown in Figure 3.13, the performances of the FMEPT algorithm have been compared with the conventional ORB technique under rapid variations of the wind speed. The comparison has been accomplished by observing the DC voltage and the boost DC current waveforms. It is clear from the Figure that the system reaches the MPP with a new optimum voltage by using the proposed fuzzy MEPT control strategy. Likewise, the optimum DC current is changed accordingly.

In order to quantify the benefit offered by using the proposed fuzzy algorithms in terms of quantity of extracted energy, the captured energy is evaluated for the proposed and conventional algorithms under the same wind speed.

As can be observed from Figure 3.15, the simulation results together with the comparison explicitly demonstrated that the proposed FMAPT and FMEPT provide the highest MPPT efficiencies of respectively 99.8% and 97.9% compared to the conventional MPPT techniques. It is deduced that the proposed FMAPT control system is quite able to generate the maximum wind power under varying wind conditions. Thus the output electrical powers and the associated MPPT efficiencies are summarized in Table 3.3.

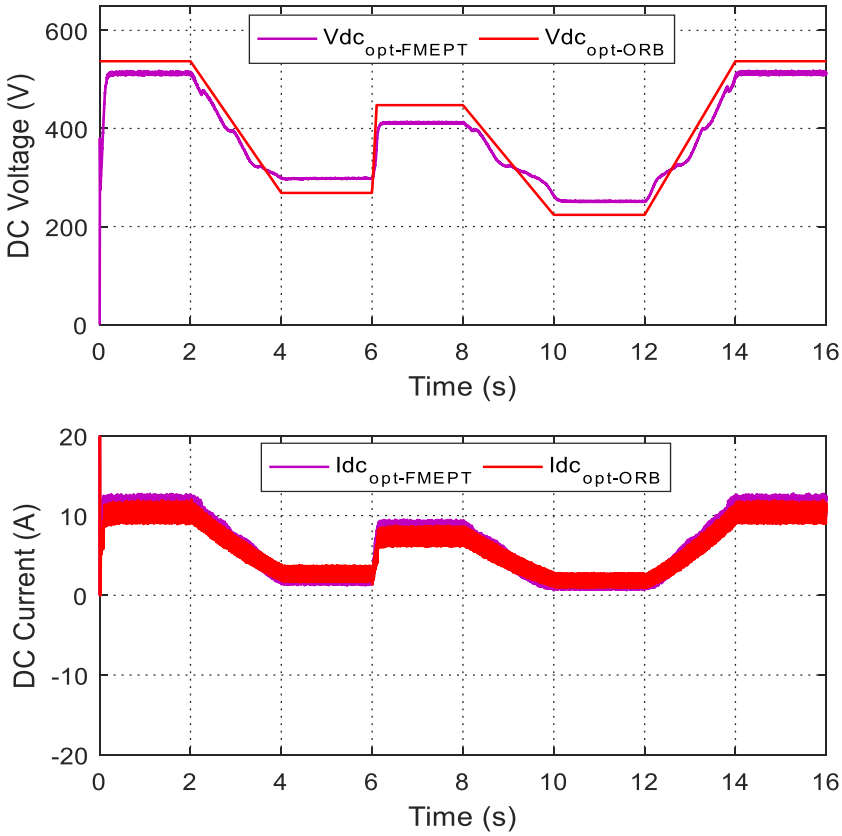

Figure 3. 13. Simulation result of the FMEPT algorithm.

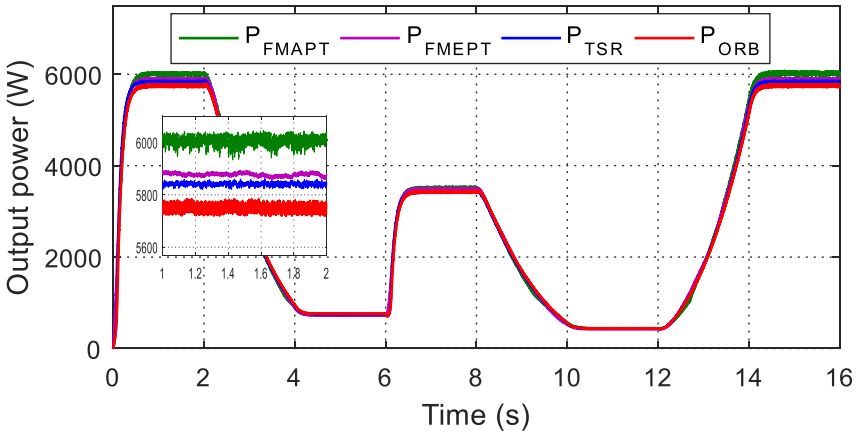

Figure 3. 14. Electrical output power P_{dc}.

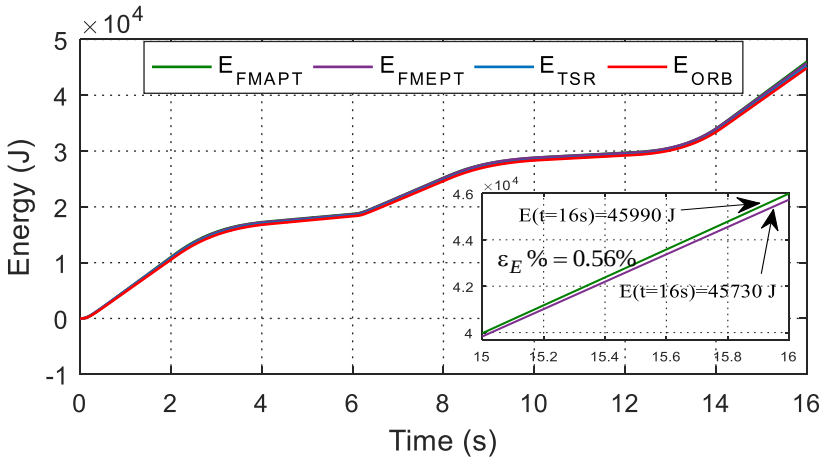

Figure 3. 15. Captured energy under fluctuating wind profile.

Table 3. 3 Comparison performances at rated wind speed for the different algorithms.

MPPT method	TSR	ORB	FMEPT	FMAPT
Output power (W)	5836	5757	5878	5990
Energy (J)	45210	44860	45730	45990
MPPT efficiency(%)	97.2%	95.9%	97.9%	99.8%

3.5 Conclusion

In this chapter, the FLC based on a fuzzy set theory was introduced. A step input responses of an oscillatory second-order system was used to explain the Mamdani fuzzy reasoning. Takagi–Sugeno (TS) fuzzy reasoning used for the system modeling and its identification was also presented and compared to Mamdani's one. Thereafter, a fuzzy optimization control scheme was applied for controlling the duty cycle of the DC-DC boost

converter. The purpose was to enhance the capability of capturing the maximum wind power of the variable wind speed. Two MPPT control schemes have been modeled, simulated and compared, namely the FMAPT and FMEPT. It is shown that the MAPT controller has to be employed to derive the optimum rotor speed corresponding to the best power point of the wind turbine based on variations of the measured aerodynamic power and rotor speed. While the FMEPT controller has been designed to track the derived optimum rectified voltage based on the variations of measured electrical DC power and the rectified voltage, and hence to achieve the maximum electrical energy from wind generator.

The simulation verifications were presented, and the proposed FMAPT and FMEPT were also compared to the conventional MPPT methods. The simulation results together with the comparison explicitly demonstrated that the proposed MEPT and MMPT provide the highest MPPT efficiencies as compared to the conventional control method. It was also deduced that the MEPT and MMPT not only provide very good responses to sudden variations in wind speed but also are simpler and lower-cost compared to the conventional ones. The proposed FMAPT control strategy has a higher overall control efficiency and can be excellently used to more effectively extract the maximum wind energy. The FMAPT will be used for the grid wind energy conversion system in the next chapter.

References

[1] *Advances and applications in nonlinear control systems*. New York, NY: Springer Berlin Heidelberg, 2016.

[2] G. Hou, Z. Jiang, Y. Yang, and J. Zhang, "Variable universe fuzzy controller used in MPPT based on DFIG wind energy conversion system," in *2016 Chinese Control and Decision Conference (CCDC)*, 2016, pp. 5871–5875.

[3] H. M. Nguyen and D. S. Naidu, "Advanced control strategies for wind energy systems: An overview," in *2011 IEEE/PES Power Systems Conference and Exposition*, 2011, pp. 1–8.

[4] A. Kentli, "Studies on Fuzzy Logic Control of Electrical Machines in Turkish Universities: An Overview," *Mathematical and Computational Applications*, vol. 16, no. 1, pp. 236–247, Apr. 2011.

[5] A. Hazzab, I. K. Bousserhane, M. Zerbo, and P. Sicard, "Real Time Implementation of Fuzzy Gain Scheduling of PI Controller for Induction Motor Machine Control," *Neural Process Lett*, vol. 24, no. 3, pp. 203–215, Dec. 2006.

[6] L. A. Zadeh, "Fuzzy sets," *Information and Control*, vol. 8, no. 3, pp. 338–353, Jun. 1965.

[7] J. Maiers and Y. S. Sherif, "Applications of fuzzy set theory," *IEEE Transactions on Systems, Man, and Cybernetics*, vol. SMC-15, no. 1, pp. 175–189, Jan. 1985.

[8] I. H. Altas and A. M. Sharaf, "A fuzzy logic power tracking controller for a photovoltaic energy conversion scheme," *Electric Power Systems Research*, vol. 25, no. 3, pp. 227–238, Dec. 1992.

[9] I. Eminolu and . H. Alts, "A method to form fuzzy logic control rules for a PMDC motor drive system," *Electric Power Systems Research*, vol. 39, no. 2, pp. 81–87, Nov. 1996.

[10] E. H. Mamdani, "Application of fuzzy algorithms for control of simple dynamic plant," *Proceedings of the Institution of Electrical Engineers*, vol. 121, no. 12, pp. 1585–1588, Dec. 1974.

[11] E. H. Mamdani and S. Assilian, "An experiment in linguistic synthesis with a fuzzy logic controller," *International Journal of Man-Machine Studies*, vol. 7, no. 1, pp. 1–13, Jan. 1975.

[12] E. H. Mamdani, "Advances in the linguistic synthesis of fuzzy controllers," *International Journal of Man-Machine Studies*, vol. 8, no. 6, pp. 669–678, Nov. 1976.

[13] I. H. Altaş, *Fuzzy Logic Control in Energy Systems with Design Applications in MATLAB®/Simulink®*. Institution of Engineering and Technology, 2017.

[14] J. A. Bernard, "Use of a rule-based system for process control," *IEEE Control Systems Magazine*, vol. 8, no. 5, pp. 3–13, Oct. 1988.

[15] L. K. Wong, F. H. F. Leung, and P. K. S. Tam, "Design of fuzzy logic controllers for Takagi–Sugeno fuzzy model based system with guaranteed performance," *International Journal of Approximate Reasoning*, vol. 30, no. 1, pp. 41–55, May 2002.

[16] K. Tanaka and M. Sano, "A robust stabilization problem of fuzzy control systems and its application to backing up control of a truck-trailer," *IEEE Transactions on Fuzzy Systems*, vol. 2, no. 2, pp. 119–134, May 1994.

[17] W. Zeng, Y. Zhao, and Q. Yin, "Sugeno fuzzy inference algorithm and its application in epicentral intensity prediction," *Applied Mathematical Modelling*, vol. 40, no. 13, pp. 6501–6508, Jul. 2016.

[18] K. Tanaka, T. Ikeda, and H. O. Wang, "Robust stabilization of a class of uncertain nonlinear systems via fuzzy control: quadratic stabilizability, H/sup /spl infin// control theory, and linear matrix inequalities," *IEEE Transactions on Fuzzy Systems*, vol. 4, no. 1, pp. 1–13, Feb. 1996.

[19] H. O. Wang, K. Tanaka, and M. F. Griffin, "An approach to fuzzy control of nonlinear systems: stability and design issues," *IEEE Transactions on Fuzzy Systems*, vol. 4, no. 1, pp. 14–23, Feb. 1996.

[20] J.-R. Jang, "ANFIS: adaptive-network-based fuzzy inference system," *IEEE Transactions on Systems, Man, and Cybernetics*, vol. 23, no. 3, pp. 665–685, May 1993.

[21] J.-S. R. Jang, *Neuro-fuzzy and Soft Computing: A Computational Approach to Learning and Machine Intelligence*. Prentice Hall, 1997.

[22] H. Fathabadi, "Novel Maximum Electrical and Mechanical Power Tracking Controllers for Wind Energy Conversion Systems," *IEEE Journal of Emerging and Selected Topics in Power Electronics*, vol. 5, no. 4, pp. 1739–1745, Dec. 2017.

[23] A. Mirecki, X. Roboam, and F. Richardeau, "Architecture Complexity and Energy Efficiency of Small Wind Turbines," *IEEE Transactions on Industrial Electronics*, vol. 54, no. 1, pp. 660–670, Feb. 2007.

[24] X. Yunqi, "A novel optimum power fuzzy control strategy for doubly-fed wind turbine," in *IEEE ICCA 2010*, 2010, pp. 165–170.

[25] T. Azzouz, "Modélisation et commande d'un système de conversion d'énergie éolienne à base d'une MADA," phd, Université Mohamed Khider - Biskra, 2015.

[26] A. Mirecki, "Étude comparative de chaînes de conversion d'énergie dédiées à une éolienne de petite puissance," thesis, Toulouse, INPT, 2005.

[27] P.-C. Cheng, B. Peng, Y.-H. Liu, Y.-S. Cheng, and J.-W. Huang, "Optimization of a Fuzzy-Logic-Control-Based MPPT Algorithm Using the Particle Swarm Optimization Technique," 2015.

[28] B. Babes and L. Rahmani, "Commande prédictive de la machine synchrone à aimant permanent utilisée dans un système éolien," phd, Université Ferhat Abbas faculté de Technologie département d'électrotechnique, Sétif, 2018.

[29] S. Abdeddaim and A. Betka, "Optimal tracking and robust power control of the DFIG wind turbine," *International Journal of Electrical Power & Energy Systems*, vol. 49, pp. 234–242, Jul. 2013.

Chapter 4 Control Strategy for a grid-connected wind system with a battery energy storage.

4.1 Introduction

This chapter aims to supply the basic concepts to understand a wind energy system and the way it must be operated to be connected to the utility grid and to balance the power flow within the system irrespective of fluctuating wind conditions and load demands by the integration of an energy storage system.

The proposed coordinated controller has three subsystems (generator side converter, BESS side converter, and grid side system). The control of the generator side converter has been detailed in the previous chapters. Therefore, the method that obtains better results, i.e. the FMAPT algorithm, is retained to connect the system to the utility grid.

In this chapter, particular attention is paid to the grid side and BESS. The control of the both subsystems is examined, by studying their dynamic models. Therefore, once the dynamic models are understood, it is possible to study their control.

The vector control strategy is based on the space vector representation of the grid side system. It is revealed as an effective control that provides reasonably simple and easy to understand characteristics, accompanied by a good performance. Hence, utilizing this control, the main objectives of the GSC are achieved: control of the DC bus voltage and maintain the amplitude and frequency of the grid.

The DC-link voltage control represents a key part to balance the power flow between the generation and the load irrespective of the variable wind speed and load demand [1]. Reliable DC-link voltage regulation control based on fuzzy logic is developed to replace the conventional PI controller. The purpose is to present a comparative control study between a classical PI, a conventional Fuzzy-PI, and an Adaptive Fuzzy Logic Controller-PI (AFLC-PI) for setting the DC-link voltage at the predetermined value with a view to extract the maximum possible power from the wind [2, 3].

Finally, the power management control strategy for a PMSG based VSWT along with lead-acid battery energy storage is proposed for the purpose of ameliorating the performance

of the battery storage by consuming the excess power and supplying the deficit power. Extensive simulation results have been performed using MATLAB/Simpower system**.**

4.2 System description

A PMSG-based wind power system is connected to the grid through a series of power electronic-based interfacing units so as to permit the wind turbine to operate at changeable wind speed, as illustrated in Figure 4.1. To achieve MPPT and DC-link voltage regulation as the wind speed changes, the generator-side converter is designed to control the wind turbine and generator speed to track maximum power at various wind speeds, while the grid-side converter matches the output power from the generator to the AC grid by maintaining a constant DC-link voltage. This enables a fixed frequency and fixed voltage to be supplied to the utility grid.

The grid side filter is used in line with the inverter to provide a smooth and pure sinusoidal waveform, while the transformer is used to provide isolation between the grid and the wind turbine [4, 5].

The bidirectional converter for the battery is used to balance the power flow by charging or discharging the battery as per requirements. The battery current (i_{bat}) can flow in and out of the battery by triggering the DC-DC converter switches.

The following subsections explain each element in more detail.

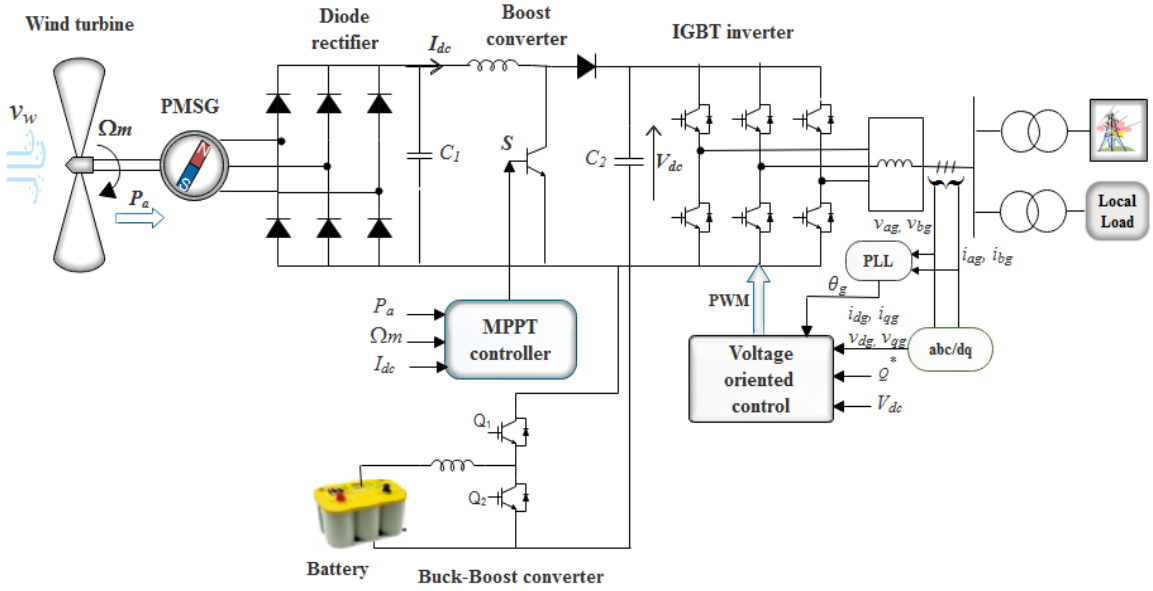

Figure 4. 1. Schematic diagram of PMSG based WECS connected to the grid with BESS.

4.3 Three-phase VSI model

Figure 4.2 shows the electrical scheme of the three-phase DC/AC VSI. The inverter transforms a DC voltage to a three-phase AC voltage with fixed magnitude and frequency for the grid [6].

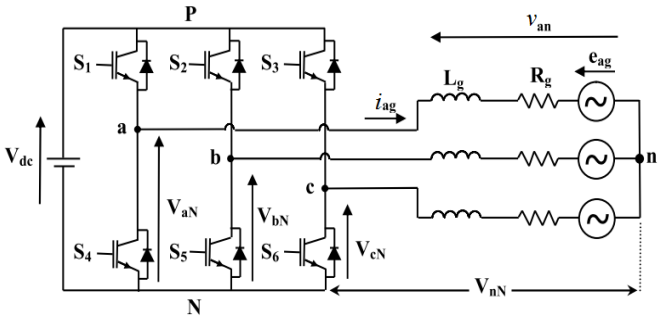

Figure 4. 2. VSI power circuit.

The three-phase DC/AC is a two-level VSI. It consists of six power electronic semiconductor switches (normally IGBT) and six antiparallel diodes allowing bidirectional current flow and unidirectional voltage blocking capability [4]. There are three-phase legs of power switches and free-wheeling antiparallel diodes, two power switches are in each inverter phase leg of the VSI operate in a complementary mode to avoid short-circuiting the DC-link voltage supply [7].

The operating status of the switches in the two-level inverter in Figure 4.2 can be represented by switching states. As indicated in Table 4.1, switching state **1** denotes that the upper switch in an inverter leg is ON and the inverter terminal voltage is positive *(+V_{dc})*, whereas **0** indicates that the inverter terminal voltage is zero due to the conduction of the lower switch. There are eight possible combinations of switching states in the two-level inverter. The formula of the six active vectors can be given as follows [4]:

$$\overrightarrow{V_k} = \frac{2}{3} V_{dc} e^{j(k-1)\frac{\pi}{3}} \tag{4.1}$$

k=1,….,6

where V_{dc} is the DC link voltage (V).

The zero vector V_0 has two switching states [111] and [000], one of which is redundant.

Table 4. 1. Switching states.

Switching state	Leg *a*			Leg *b*			Leg *c*		
	S_1	S_4	V_{aN}	S_3	S_6	V_{bN}	S_5	S_2	V_{cN}
1	ON	OFF	V_{dc}	ON	OFF	V_{dc}	ON	OFF	V_{dc}
0	OFF	ON	0	OFF	ON	0	OFF	ON	0

A typical space vector diagram for the two-level inverter is shown in Figure 4.3, where the six active vectors V_1 to V_6 form a regular hexagon with six equal sectors (1 to 6). The zero vectors V_0 and V_7 lie at the center of the hexagon.

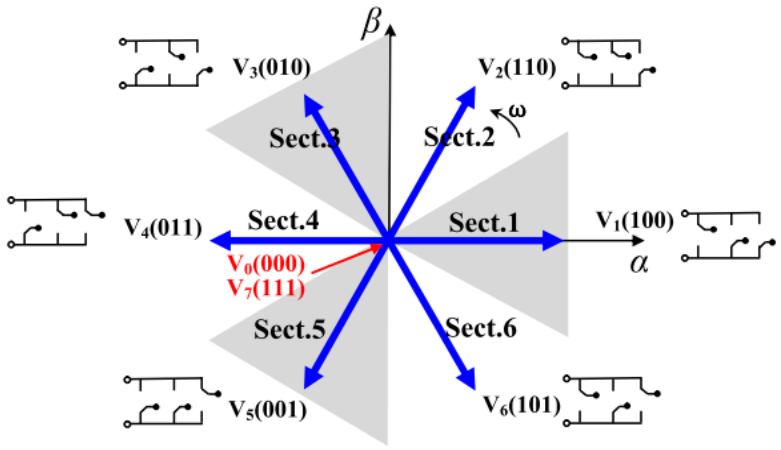

Figure 4. 3. Space-vector diagram for the two-level inverter in the αβ plane.

4.4 Grid Model

The grid voltage is modeled as an ideal three-phase balanced voltage consisting of a series combination of resistance and inductance [7, 8]. The line resistance is negligibly small and has a limited impact on the performance of the system. The three-phase system can be modeled as three independent, but equivalent, single-phase systems as depicted in Figure 4.4.

Taking into account the definitions of variables from the circuit shown in Figure 4.4. The electric equations of the system can easily be derived as follows:

$$v_{ai} = L_g \frac{di_{ag}}{dt} + R_g i_{ag} + v_{ag} \tag{4.2}$$

$$v_{bi} = L_g \frac{di_{bg}}{dt} + R_g i_{bg} + v_{bg} \tag{4.3}$$

$$v_{ci} = L_g \frac{di_{cg}}{dt} + R_g i_{cg} + v_{cg} \tag{4.4}$$

where R_g and L_g are the equivalent series resistance and inductance of the grid-side filter, respectively. v_{ai}, v_{bi}, v_{ci} are the inverter voltages. v_{ag}, v_{bg}, v_{cg} are the grid voltages. i_{ag}, i_{bg}, i_{cg} are the grid currents.

For wind energy applications, the active (P_g) and reactive power (Q_g) supplied to the grid can be expressed as [9]:

$$P_g = 3v_g i_g \cos\varphi_g \tag{4.5}$$

$$Q_g = 3v_g i_g \sin\varphi_g \tag{4.6}$$

where:

v_g is the rms grid phase voltage (V).

i_g is the rms grid current (A).

Φ_g is the grid power factor angle (deg).

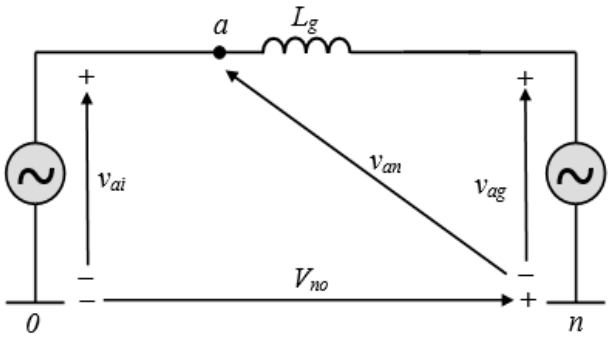

Figure 4. 4. Simplified equivalent single-phase grid circuit (a phase).

4.5 Battery Energy Storage System (BESS)

Energy storage provides an opportunity to grasp and balance the wind energy as it is produced. It may be stored and used later when the demand is expected to increase the capacity of the wind energy production [10, 11]. The research work in this thesis considers the lead-acid battery as an energy storage due to its popularity on the renewable energy market, and its good performances compared to other types of batteries. The system is clean and does not suffer from deleterious chemical action while its energy density and its specific energy are low. The lead-acid battery performs reliably and robust over a wide range of temperature. One of the main factors for its popularity choice and dominant position is its low cost with good performance and life cycle [12, 13].

4.5.1 Battery model

To simulate the system, a model of BESS has to be defined. In the literature, BESS models developed for the sizing and the scheduling are simple with a few parameters such as battery current, capacity, state of charge and temperature [14]. All these parameters are varied with the operating conditions and affect the capacity of the battery to charge or discharge. The lead-acid battery used in this work is modeled by the battery model included in SimPower Systems [15]. It is modeled as a variable voltage source in series with an equivalent internal resistance as shown in Figure 4.5.

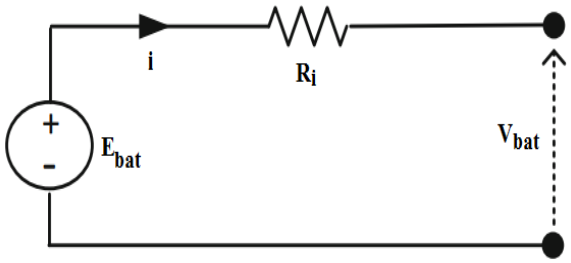

Figure 4. 5. Simplified lead–acid battery model.

As Figure 4.5 illustrates, the battery voltage is given by the following equation:

$$V_{bat} = E_{bat} - R_i i_{bat} \tag{4.7}$$

where V_{bat} is the battery rated voltage, R_i is internal resistance (Ω). The battery output voltage E_{bat} for the period of charging or discharging depends on the internal battery parameters such as the battery current i_{bat}, the hysteresis phenomenon during the charging/discharging cycles and the extracted capacities [13, 16].

i. Discharging mode

In the discharge mode where $i_{bat}^* > 0$, the lead-acid battery is modeled by equation (4.8):

$$E_{bat} = E_0 - K\frac{Q}{Q - i_t} i_{bat}^* - K\frac{Q}{Q - i_t} i_t + f_{hyst-dish}(i) \tag{4.8}$$

ii. Charging mode

In the charge mode where $i_{bat}^* < 0$, the lead-acid battery is modeled by equation (4.9):

$$E_{bat} = E_0 - K\frac{Q}{0.1Q - |i_t|} i_{bat}^* - K\frac{Q}{Q - i_t} i_t + f_{hyst-char}(i) \tag{4.9}$$

where E_0 is the battery constant voltage (V), K is the polarization constant (V/Ah), Q is the battery capacity (Ah), i_t is the actual battery charge (Ah), and i_{bat}^* is the filtered current (A).

iii. **Instantaneous characteristics**

The state of charge (SOC) of the BESS is the parameter related to the number of charges stored in the battery. A SOC of 100% means that the BESS is fully charged, whereas at 0% it is considered empty. In real-life situations, it is important to maintain the SOC within the limits recommended to prevent internal damage, $SOC_{min} \leq SOC \leq SOC_{max}$. The SOC is calculated by [16, 17]:

$$SOC = 1 - \frac{Q_e}{C(0,\theta)} \tag{4.10}$$

Another variable widely used in the literature is the depth of discharge (DOD), which describes the emptiness of the battery (complement of the SOC). It is defined as:

$$DOC = 1 - \frac{Q_e}{C(I_{avg},\theta)} \tag{4.11}$$

where Q_e (A s) is the charge of the battery, DOC is the battery depth of charge, I_{avg} (A) is the mean discharge current, and C(A s) is the BESS capacity.

4.5.2 Battery converter modeling

A variety of DC/DC power converter based PWM serves as an interface between the various energy sources and the DC bus; these converters are used to control the flow of energy between sources to regulate the DC link voltage (V_{dc}) by charging or discharging the battery as per requirements [18, 38]. In this present study, the lead-acid battery is connected to the DC bus through a bidirectional DC/DC converter (buck-boost). Therefore, the flow of current and power is bidirectional, depending on the operating conditions (change in the wind speed and the load). The schematic diagram of the battery DC/DC buck-boost converter is shown in Figure 4.6. It consists of a high-frequency inductor, an output filtering capacitor, and two IGBT-diodes switches. The upper and lower switches make it possible to charge and discharge the battery storage system [18, 19].

Switches Q_1 and Q_2 are switched so that the converter operates in a steady state with four sub-intervals. A brief description of the operation of four different interval times is below [20]:

- **Interval 1 (t_0 - t_1)**

In this interval, the lower switch Q_2 is ON and the upper switch Q_1 is OFF with diode D_1 and D_2 reverse biased as shown in Figure 4.7 (a). During this time, the converter operates

in the boost mode and the inductor is charged and current through the inductor increases. The battery voltage (V_{bat}) and the increased inductor current (Δi_{bat} (+)) are expressed as follows:

$$V_{bat} = L\frac{di_{bat}}{dt} = L\frac{\Delta i_{bat}}{\Delta T} \tag{4.12}$$

$$\Delta i_{bat}(+) = \frac{V_{bat}}{L} T_{ON} \tag{4.13}$$

where T_{ON} is the ON time of lower switch Q_2.

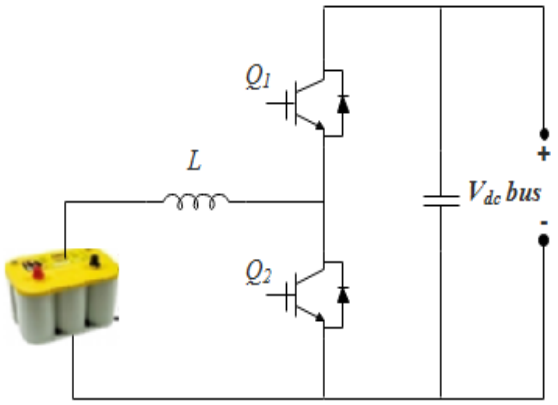

Figure 4. 6. Bidirectional DC/DC battery power converter.

– **Interval 2 ($t_1 – t_2$)**

During this interval, both switches Q_1 and Q_2 are turned OFF. The diode D_1 of the upper switch Q_1 conducts as shown in Figure 4.7 (b). In this case, the inductor current starts decreasing. The decrease of the induction current (Δi_{bat} (-)) during the OFF state is given by:

$$\Delta i_{bat}(-) = \frac{(V_{dc} - V_{bat})}{L} T_{OFF} = \frac{(V_{dc} - V_{bat})}{L}(T - T_{ON}) \tag{4.14}$$

where T_{OFF} is the OFF time of the lower switch Q_2 and T is the total time of operation.

In steady-state operation, (Δi_{bat} (+)) during ON time and (Δi_{bat} (-)) during OFF time has to be equal. Consequently, (4.13) and (4.14) are equated as follows:

$$\frac{V_{bat}}{L} T_{ON} = \frac{(V_{dc} - V_{bat})}{L}(T - T_{ON}) \tag{4.15}$$

The relationship between battery voltage (V_{bat}) and DC link voltage (V_{dc}) as a function of the duty ratio can be expressed as:

$$V_{bat} = d_u \times V_{dc} \tag{4.16}$$

Where d_u is the duty ratio for the upper switch of the battery converter.

– **Interval 3 ($t_2 – t_3$)**

At time (t_2 - t_3) the upper switch Q_1 is ON and the lower switch Q_2 is turned OFF with diode D_1 and D_2 on the reversed bias, as shown in Figure. 4.7 (c). During this interval, the converter operates in buck mode. The inductor current is expressed as follows:

$$\Delta i_{bat}(+) = \frac{(V_{dc} - V_{bat})}{L} T_{ON} \tag{4.17}$$

– **Interval 4 ($t_3 – t_4$)**

During this interval, both upper switch Q_1 and lower switch Q_2 are turned OFF and the diode D_2 of the lower switch conducts as shown in Figure 4.7 (d). During this interval, the converter works as a buck converter. The inductor current decreases and expressed as follows:

$$\Delta i_{bat}(-) = \frac{V_{bat}}{L} T_{OFF} = \frac{V_{bat}}{L}(T - T_{ON}) \tag{4.18}$$

In steady-state operation, Δi_{bat} (+) during ON time and Δi_{bat} (-) during OFF time have to be equal. As a result, (4.17) and (4.18) are equated as follows:

$$\frac{(V_{dc} - V_{bat})}{L} T_{ON} = \frac{V_{bat}}{L}(T - T_{ON}) \tag{4.19}$$

From equation (4.19), the output voltage can be expressed as a function of duty ratio as:

$$V_{dc} = \frac{1}{1 - d_L} V_{bat} \tag{4.20}$$

where d_L is the duty ratio for the lower switch of the battery converter.

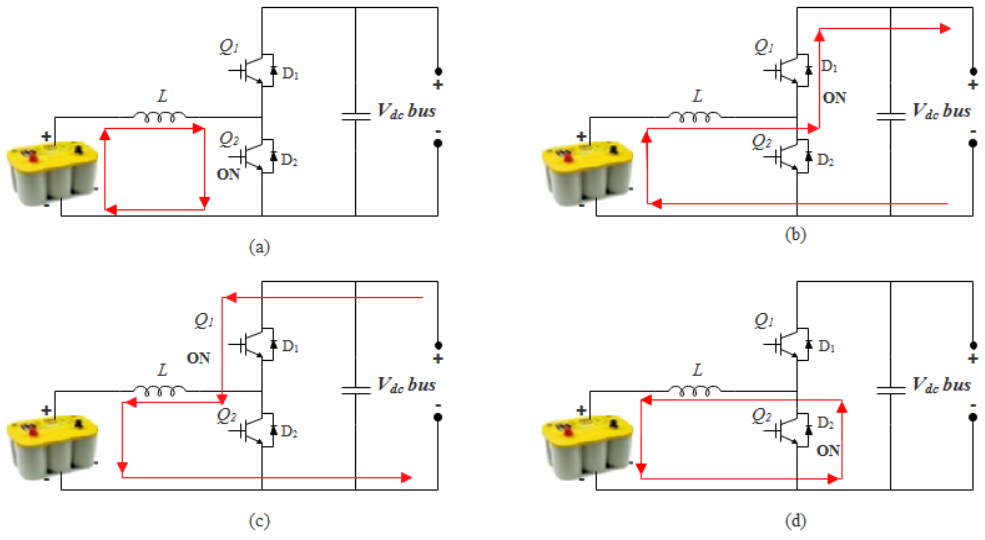

Figure 4. 7. Bidirectional DC-DC converter operation, (a) interval 1, (b) interval 2, (c) interval 2, (d) interval 4.

4.6 Control of the grid-side system

This section tackles the control of the grid side converter where a vector control based scheme is studied. Among control strategies for grid-connected converter, this control technique is widely extended due to its good performance characteristics with reasonably simple implementation requirements [21, 22]. Using this control strategy, it is possible to achieve two main objectives of the GSC: control of the DC link voltage and control of the active/reactive power supplied to the grid to ensure reliable operation of the system [4, 23]. The simplified block diagram of the grid side system control is given in Figure 4.8.

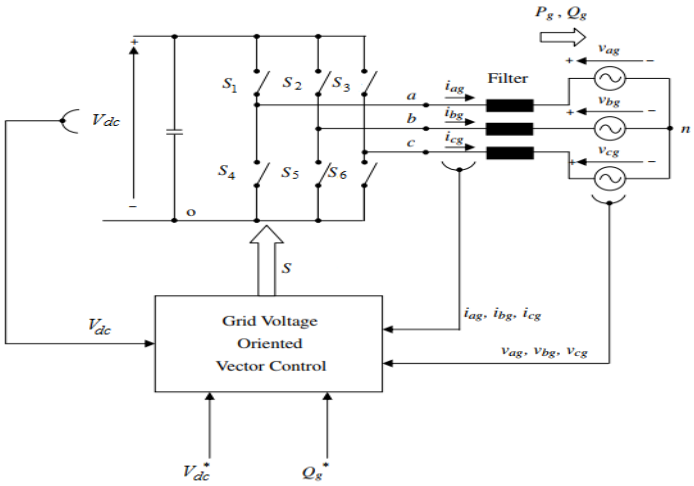

Figure 4. 8. Grid side system control.

4.6.1 Voltage Oriented Control (VOC)

Figure 4.9 shows the VOC scheme for the grid-connected inverter. This scheme is based on the park transformation. It is possible to express the three-phase voltages with the *dq* components. The control algorithm is implemented in the grid-voltage synchronous reference frame, where all the variables are from the DC components in steady-state [24]. This facilitates the design and control of the inverter.

To realize the VOC, the angle of the grid voltage is needed θ_g. This angle is used for voltage and current coordinate transformations by means of Park's transformation (*abc* - *dq*) or through Park's inverse transformation (*dq* – *abc*) [25]. In general, this angle is estimated by a Phase Locked Loop (PLL).

As illustrated in Figure 4.9, the control strategy consists of three control loops in the system. These are:

– Two inner current loops regulated by the *PI* controller for the *dq*-axis currents.

– One outer DC voltage loop controlled by two based FLC, including a Fuzzy-PI and an AFLC-PI to compare the performance of both controllers.

With the VOC scheme, the three-phase line currents in the *abc* stationary frame i_{ag}, i_{bg}, and i_{cg} are transformed into the two-phase currents i_{dg} and i_{qg} in the *dq* synchronous frame. The independent control of these two current components provides an effective means for the independent control of the active and reactive power of the system [26].

To achieve the VOC scheme, the *dq*-axis is aligned with the grid voltage vector, therefore the *d*-axis grid voltage is equal to its magnitude ($v_{dg} = v_g$) and the *q*-axis voltage v_{qg} is then equal to zero $v_g = \sqrt{\left(v_{dg}\right)^2 + \left(v_{qg}\right)^2} = 0$, from which the active and reactive power of the system are calculated as beneath [20]:

$$\begin{cases} P_g = \dfrac{3}{2}\left(v_{dg} i_{dg} + v_{qg} i_{qg}\right) \\ Q_g = \dfrac{3}{2}\left(v_{qg} i_{dg} + v_{dg} i_{qg}\right) \end{cases} \tag{4.21}$$

for v_{qg}=0, the equations for the active and reactive power can be written as:

$$\begin{cases} P_g = \dfrac{3}{2} v_{dg} i_{dg} \\ Q_g = -\dfrac{3}{2} v_{dg} i_{qg} \end{cases} \tag{4.22}$$

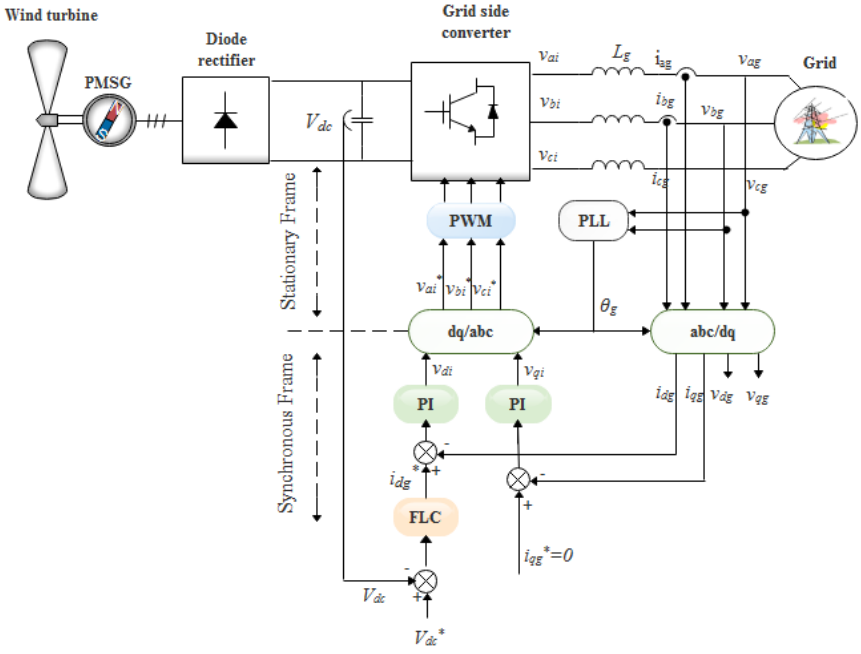

Figure 4. 9. Block diagram of the VOC.

4.6.1.1 Current Controllers

Figure 4.10 represent a typical scheme of dual control using one current regulator (made up of two PI controllers, one for the *d* axis and the other for the *q* axis). The input of the first controller is then the *d*-axis current reference, which represents the active power of the system. It is generated by the control of the DC voltage loop. The input of the second one is the *q-axis* current reference i_{qg}^{*} which can be obtained from

$$i_{qg}^{*} = \frac{Q_g^{*}}{-1.5v_{dg}} \tag{4.23}$$

where Q_g^{*} is the reactive power reference, which can be set to zero for a unity power factor operation, a negative value for leading power factor operation, or a positive value for lagging power factor operation.

4.6.1.2 Fuzzy-PI (F-PI) based DC link voltage control

The control of V_{dc} is necessary since the DC link is mainly formed by a capacitor. Thus, the active power flow through the rotor must cross the DC link and then it should be transmitted to the grid. Therefore, by only controlling the V_{dc} variable to a constant value, this active power flow through the converters is ensured, together with a guarantee that both grid and generator side converters keep available the required DC voltage to work properly [27]. As seen in Figure 4.11, the controller for the DC link voltage generates the reference for the d-axis current (i_{dg_ref}) according to the operating condition of the inverter. The DC link voltage V_{dc} at the input of the inverter is regulated to a fixed value set by its reference V_{dc_ref}. This task can be performed by using the proposed F-PI controller [2, 3].

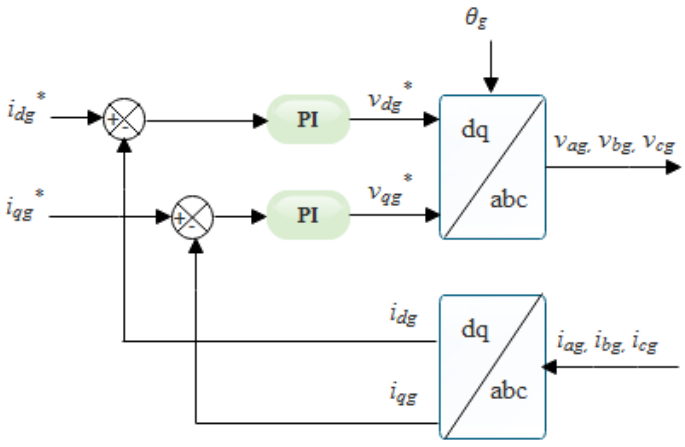

Figure 4. 10. Dual current control scheme.

The proposed PI-based FLC is illustrated in Figure 4.11. The voltage error and its derivative are the two input signals of the FLC. These inputs, defined as in equation (4.24), are first fuzzified and converted to fuzzy membership values used in the rule base in order to execute the related rules so that the d-axis current, i_{dg_ref} can be generated.

$$\begin{cases} e[k] = V_{dc\_ref}[k] - V_{dc}[k] \\ \Delta e[k] = e[k] - e[k-1] \end{cases} \tag{4.24}$$

where e[k] and Δe[k] denote the DC link voltage error and its change at the sampling instant (t_k), respectively. Both variables are normalized by the scaling factors K_1 and K_2,
V_{dc}[k] and V_{dc}[k-1] indicate the DC link voltage at the sampling instants (t_k) and (t_{k-1}), respectively.

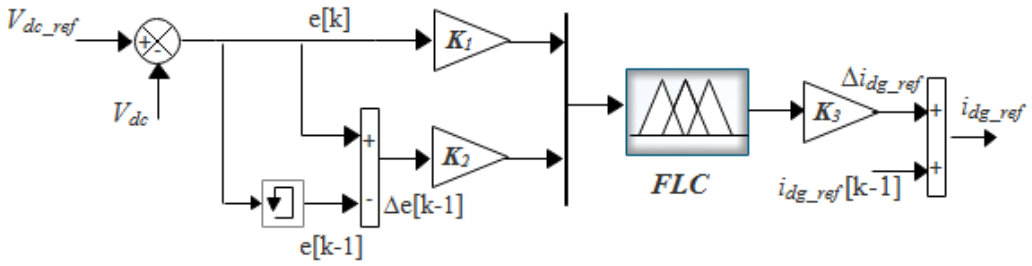

Figure 4. 11. F-PI control structure.

The change in the d-axis current Δi_{dg_ref} is used as an output of the proposed FLC. To design the fuzzy sets of the inputs and output variables, triangular symmetrical membership functions are used to yield more sensitivity to small signals illustrated in Figure 4.12 [28]. Input and output variables, i.e. e[k], Δe[k] and Δi_{dg_ref} are represented by linguistic variables such as **PB** (Positive Big), **PS** (Positive Small), **Z** (Zero), **NB** (Negative Big), and **NS** (Negative Small) using basic fuzzy subsets. Control rules are derived from the experience and knowledge on the control system. The fuzzy mapping of the input variables to the output is given in Table 4.2.

Mamdani type reasoning is applied to the inference mechanism [29]. The defuzzification is performed using the Centroid Of Area (COA) of final combined fuzzy set. The final combined fuzzy set is defined by the union of all rule output fuzzy sets using the maximum aggregation method [28]. Thus, the change of the d-axis current (Δi_{dg_ref}) is determined. The COA method is expressed as follows:

$$\Delta i_{dg\_ref}[k] = \frac{\sum_{i=1}^{n} \mu\left(\Delta i_{dg\_ref\,i}\right) \times \Delta i_{dg\_ref_i}}{\sum_{i=1}^{n} \mu\left(\Delta i_{dg\_ref_i}\right)} \tag{4.25}$$

Table 4. 2. Set of fuzzy rules.

e/Δe	NB	NS	Z	PS	PB
NB	NB	NB	NB	NS	Z
NS	NB	NS	NS	Z	PS
Z	NS	NS	Z	PS	PS
PS	NS	Z	PS	PS	PB
PB	Z	PS	PS	PB	PB

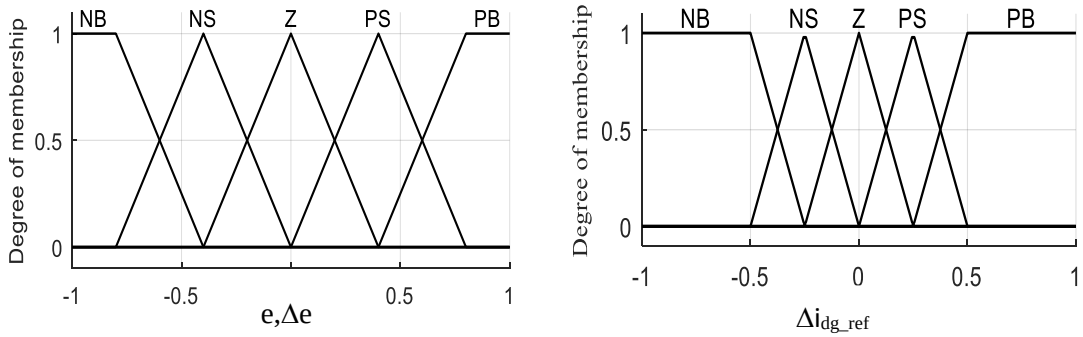

Figure 4. 12. Inputs/Output membership functions of the F-PI controller.

The output Δi_{dg_ref} [k] from the fuzzy reasoning block is added to the previous value of the control signal to obtain the new value i_{dg_ref} [k]. This procedure gives an integral action to the FLC as:

$$i_{dg\_ref}[k] = i_{dg\_ref}[k-1] + \Delta i_{dg\_ref}[k] \tag{4.26}$$

4.6.13 Adaptive fuzzy based DC link voltage control

The AFLC-PI is a conventional PI controller strengthened by a fuzzy logic algorithm. On the one hand, it has adaptive ability which enables it to automatically identify the controlled process parameters, set control parameters and adapt the process parameters variation. On the other hand, it also has the advantages of the PI controller, such as simple structure, high reliability, and familiarity to practical engineering-design personnel [30-32].

The AFLC-PI is shown in Figure 4.13. The DC-link voltage control loop consists of one conventional PI controller and one fuzzy inference calculation. The calculation part is a FLC.

The PI parameters are modified by using the fuzzy rules, and then the AFLC-PI is constructed.

The design process for the AFLC-PI consists of four parts: (i) determining of inputs and outputs, (ii) reasoning of fuzzification and fuzzy logic rules, (iii) defuzzification, (iv) parameters tuning of PI controller.

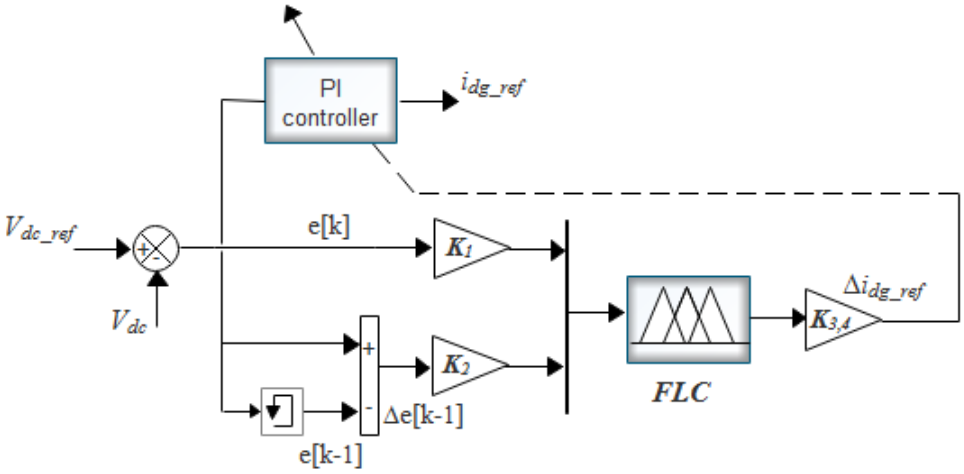

Figure 4. 13. AFLC-PI control structure.

a. Inputs and outputs determining

The FLC inputs are the DC link voltage error ($e=V_{dc\_ref} - V_{dc}$) and its change (Δe). The inputs are continuously checked and calculated by the FLC, and then the parameters of the *PI* controller are adjusted by using the fuzzy logic rules in order to achieve optimal parameters.

As shown in Figure 4.14, the input universes are defined in the interval {–1, 1}, where each one of the universes of $e(k)$ and $\Delta e(k)$ is partitioned into seven regions namely NB, NM, NS, Z, PS, PM, and PB. Triangular-type membership functions are used for partitioning the crisp universes into fuzzy subsets. The change in control signal (Δi_{dg_ref}) is defined in the interval {0,1} and it is partitioned into two regions as Small (**S**) and Big (**B**) represented by a *gaussian* membership function.

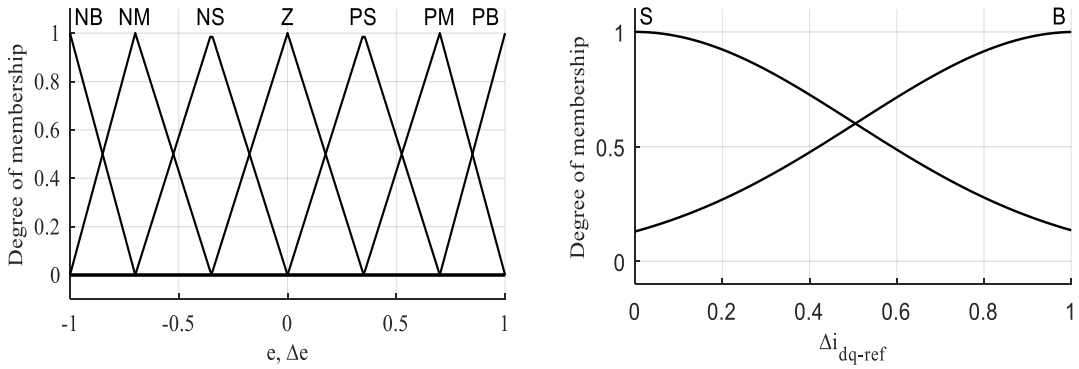

Figure 4. 14. Inputs/Output membership functions of the AFLC-PI.

b. The Inference and fuzzy reasoning

Fuzzy reasoning is the evaluation of the rules to yield fuzzy conclusions from fuzzy inputs–fuzzy rules interactions. Since the number of the subsets in the universes of $e(k)$ and $\Delta e(k)$ are seven, a rule base with 49 rules can be generated as in Table 4.3.

Table 4. 3. Set of fuzzy rules.

e/Δe	NB	NM	NS	ZR	PB	PM	PS
NB	B	B	B	B	B	B	B
NM	S	B	B	B	B	B	S
NS	S	S	B	B	B	S	S
ZR	S	S	S	B	S	S	S
PB	S	S	B	B	B	S	S
PM	S	B	B	B	B	B	S
PS	B	B	B	B	B	B	B

c. Defuzzification

Mamdani fuzzy reasoning algorithm with the COA defuzzification method is used to yield the change in the control signal Δi_{dg_ref} [33].

d. Parameters adaptation of the PI controller

The proposed PI parameters adaptation seeks to find out the fuzzy relationship between the two parameters of PI and the inputs of the FLC [34]. To implement the FLC of the grid-connected in a closed-loop, the DC-link voltage (V_{dc}) is sensed and then compared with the reference DC-link voltage (V_{dc_ref}). The inputs e and Δe are continuously checked and

calculated by the FLC, and then the parameters of the PI controller are adjusted by using the fuzzy rules in order to achieve an excellent dynamic and static performance of the WECS. Tuning of the Parameters is based on the fuzzification results processing, the fuzzy reasoning and the defuzzification. The parameter regulation formula of the AFLC-PI is:

$$\begin{cases} K_{pF} = K_p \times k_3 \cdot \Delta i_{dg\_ref} \\ K_{iF} = K_i \times k_4 \cdot \Delta i_{dg\_ref} \end{cases} \tag{4.27}$$

where K_{pF} and K_{iF} are the fuzzy PI parameters, k_3 and k_4 are the scaling factors and, Δi_{dg_ref} is the fuzzy output signal. The final control signal is obtained as:

$$i_{dg\_ref} = K_{pF} e + K_{iF} T_S e(k) \tag{4.28}$$

T_S is the sampling period.

4.6.2 VOC with decoupled Controller

To further investigate the VOC scheme, the state equation for the grid-side circuit of the inverter in the *abc* stationary reference frame can be expressed as [4, 35]:

$$\begin{cases} \dfrac{di_{ag}}{dt} = \left(v_{ag} - v_{ai}\right) / L_g \\ \dfrac{di_{bg}}{dt} = \left(v_{bg} - v_{bi}\right) / L_g \\ \dfrac{di_{cg}}{dt} = \left(v_{cg} - v_{ci}\right) / L_g \end{cases} \tag{4.29}$$

The above equations can be transformed into the *dq* synchronous reference frame as:

$$\begin{cases} \dfrac{di_{dg}}{dt} = \left(v_{dg} - v_{di} + \omega_g L_g i_{qg}\right) / L_g \\ \dfrac{di_{qg}}{dt} = \left(v_{qg} - v_{qi} + \omega_g L_g i_{dg}\right) / L_g \end{cases} \tag{4.30}$$

where v_{di}, v_{qi} are the *d*-*q* axis voltages of the inverter, ω_g is the speed of the synchronous reference frame, which is also the angular frequency of the grid, $\omega_g L_g i_{qg}$ and $\omega_g L_g i_{dg}$ are the induced speed voltages.

The above equations clearly show that there is a relationship between the derivative of the *d*-axis and *q*-axis currents with both *d*-axis and *q*-axis variables. This means that the system control is cross-coupled, which may lead to difficulties in the controller design and unsatisfactory dynamic performance [36]. To tackle this problem, a decoupled controller shown in Figure 4.15 can be implemented.

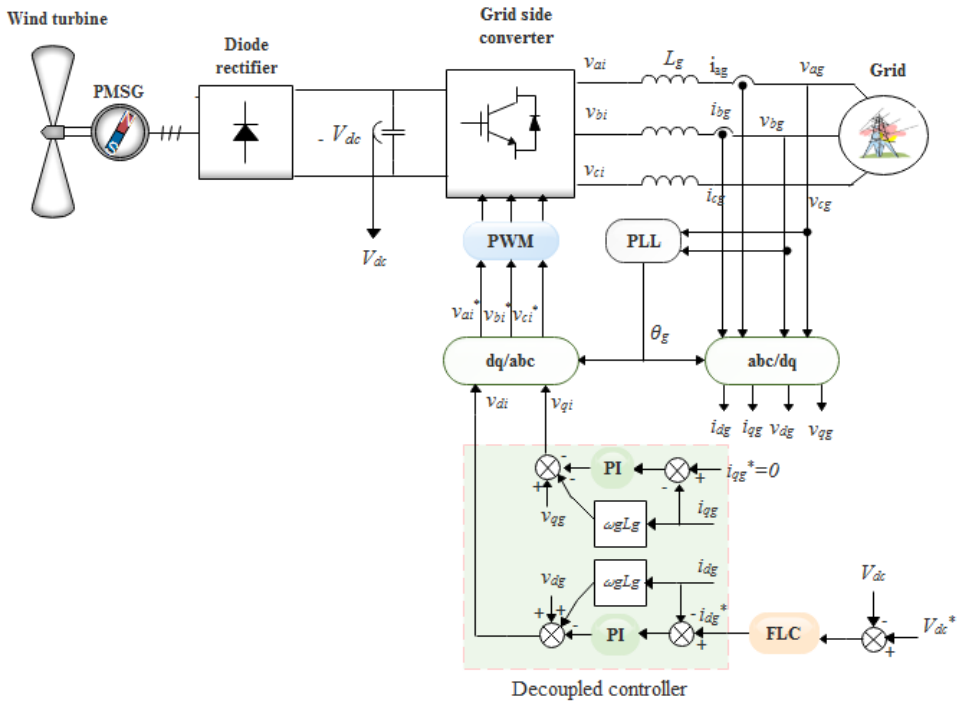

Figure 4. 15. VOC with a decoupled controller.

The output of the decoupled controller can be expressed as:

$$\begin{cases} v_{di} = -\left(K_p + K_i / S\right)\left(i_{dg}^{*} - i_{dg}\right) + \omega_g L_g i_{qg} + v_{dg} \\ v_{qi} = -\left(K_p + K_i / S\right)\left(i_{qg}^{*} - i_{qg}\right) - \omega_g L_g i_{dg} + v_{qg} \end{cases} \tag{4.31}$$

Substituting (4.31) into (4.30) yields:

$$\begin{cases} \dfrac{di_{dg}}{dt} = \left(K_p + K_i / S\right)\left(i_{dg}^{*} - i_{dg}\right) / L_g \\ \dfrac{di_{qg}}{dt} = \left(K_p + K_i / S\right)\left(i_{qg}^{*} - i_{qg}\right) / L_g \end{cases} \tag{4.32}$$

The above equations indicate that a decoupled control between the *dq*-axis currents is obtained. This makes the design of the PI controllers more convenient, and also the system is more easily stabilized.

4.7 Energy management algorithm for BESS

The proposed control strategy is to balance the power flow between the generation and the load irrespective of the variable wind speed, the low battery storage, and the variable load demand. Therefore, the proposed control strategy is based on the following features:

i. The control strategy is based on the power balance demand-generation mismatch $P_{opt} - P_L$, and on the state of charge (SOC) of the battery,

ii. The wind is operated with FMAPT scheme under varying wind speed,

iii. The operating limits of the battery are based on the SOC, which is selected in the range (30-90) % for a longer life cycle,

iv. The negative current means charging the battery and vice versa.

The proposed control strategy is explained in Figure 4.16.

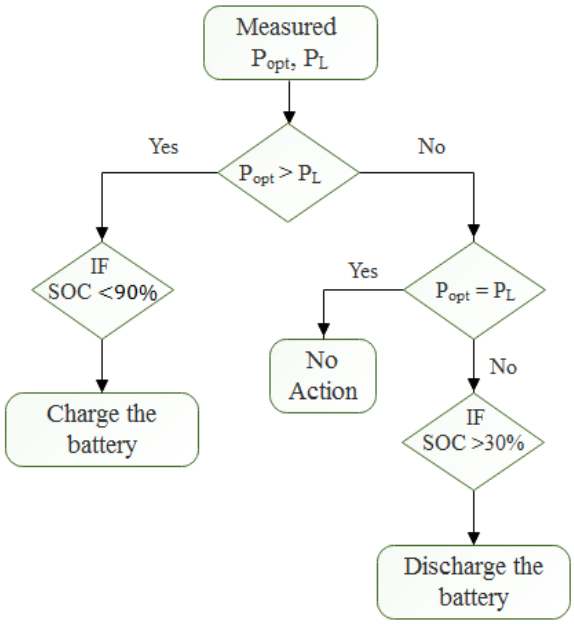

Figure 4. 16. BES control strategy.

If the load demand is less than the generation, then the SOC is checked. The excess energy is utilized in the charging of the the battery if the SOC is less than 90%. If the load demand is more than the generation, hence the power is supplied by the battery providing a SOC greater than 30% or else the grid is activated to supply the load. The control strategy for the battery converter is shown in Figure 4.17.

The battery bidirectional converter is controlled using the demand-generation mismatch, $P_{opt} - P_L$ and the SOC information. The input signal to the energy management algorithm is selected according to the demand-generation mismatch to generate the reference battery current $i_{bat\text{-}ref}$. The current $i_{bat\text{-}ref}$ is compared to the measured battery current $i_{bat\text{-}mes}$ in order to generate the gating signals for the IGBT switches. This control is realized by the PI controller. Besides, the battery status is also incorporated though the SOC enables to identify the charging and discharging stages. If the SOC is greater than 30 %, then the battery is eligible for discharging the current or supplying the deficit power. Similarly, if SOC is less than 90 % then the battery is eligible for charging or consuming the excess power.

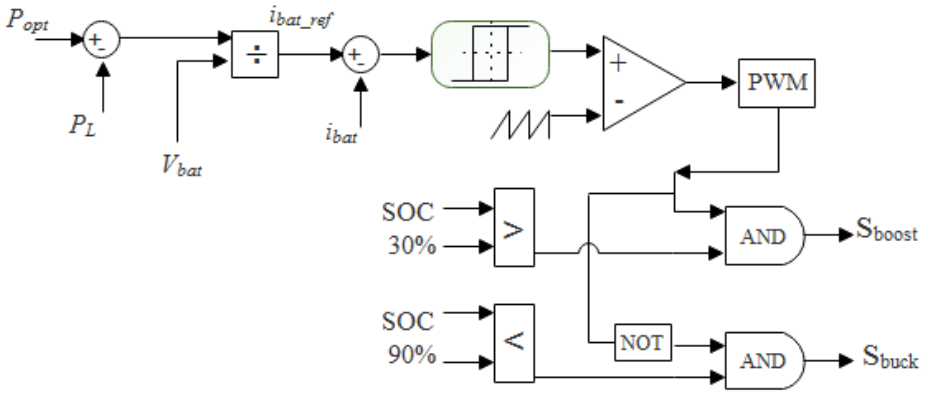

Figure 4. 17. Battery converter control strategy.

4.8 Results and discussion

Numerical simulations are performed in the Matlab/Simpower system software for a grid-connected wind energy system using the proposed FLC for the DC link voltage. The grid-connected system has been simulated for the wind speed profile depicted in Figure 4.18.

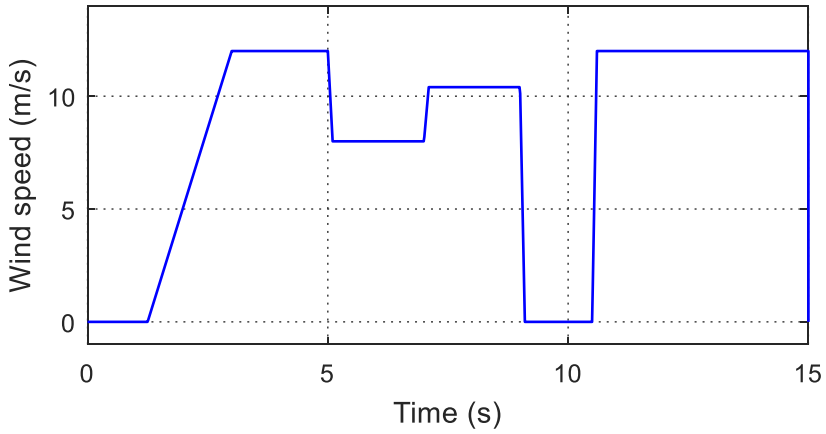

Figure 4. 18. Wind speed profile.

The performance of the proposed power management control strategy for a wind/battery system is investigated under (a) fluctuating wind speed conditions and (b) variable load. In this regard, the simulated behavior of the power flow between the generation and load is examined.

Figure 4.19 illustrates the DC link voltage V_{dc}. The simulation results show that the control effect of the FLCs is neatly highlighted. Therefore, it can be noted that F-PI has a faster response especially in comparison with the PI controller. It tracks the reference voltage of 600V perfectly (±1‰) with a good transient performance and insensitivity to wind fluctuations and load variation.

The comparison between the three controllers has been made at the rated wind speed of 12 m/s as tabulated in Table 4.4. The data reveal that the rise time and the settling time with the FLCs are less than for those of the PI controller. The overshoot is almost alike with the conventional PI and AFLC-PI controllers. Conversely, the F-PI controller provides a zero overshoot, a rise time, and a response time around 30% lower than that of the PI controller.

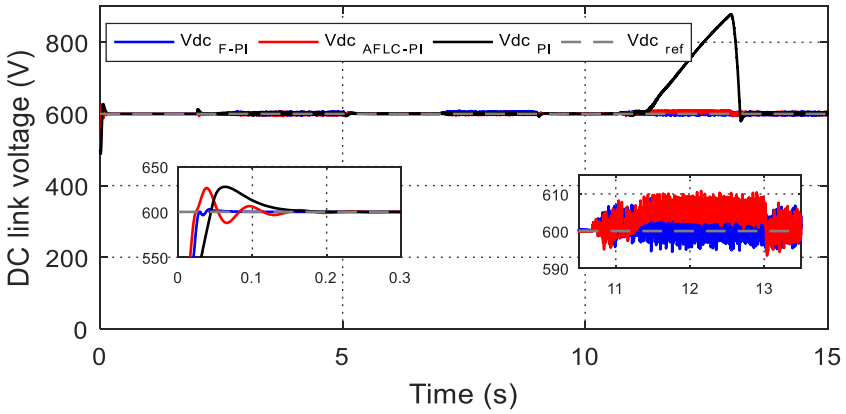

Figure 4. 19. DC-link voltage.

The *dq* grid currents are shown in Figures 4.20 and 4.21, respectively. The *d*-axis current magnitude is proportional to the wind speed, while, the *q*-axis current is forced to zero in order to achieve the unity power factor on the grid-side control. It is observed that *d*-axis current follows fairly its reference obtained by the F-PI voltage controller under varying wind speed and load demand.

Figures 4.22 and 4.23 both show that the GSC control objective is achieved. The grid voltage waveforms are perfectly sinusoidal with a constant magnitude of 311V line-to-line. The inverter AC output frequency is kept almost constant at 50 Hz under operating conditions.

The battery storage current is shown in Figure 4.24. The negative current of the battery means that the power flows from the DC link bus to the BESS, and hence charging the battery. The positive current from the battery through the converter (bidirectional inverter) to the AC load means that the battery is discharging.

From Figure 4.26, the results are simplified into two scenarios: (i) variable wind speed, and (ii) variable load demand.

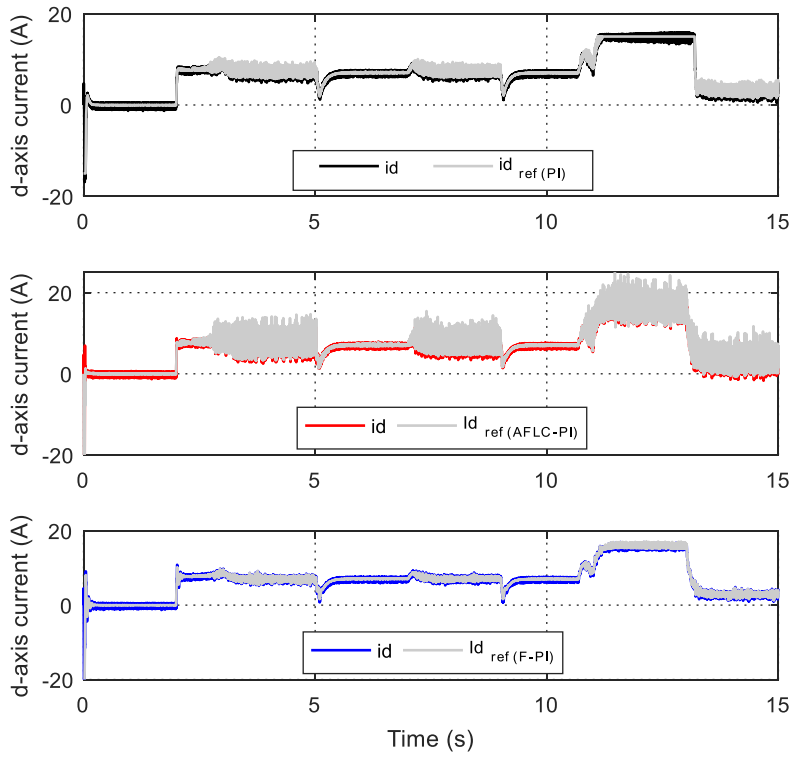

Figure 4. 20. *d*-axis grid currents.

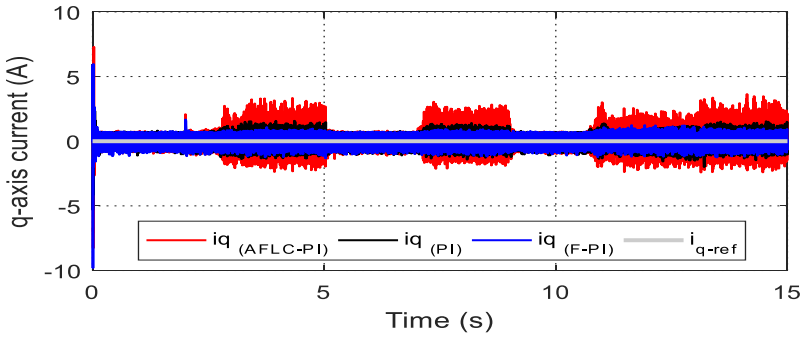

Figure 4. 21. q-axis grid currents.

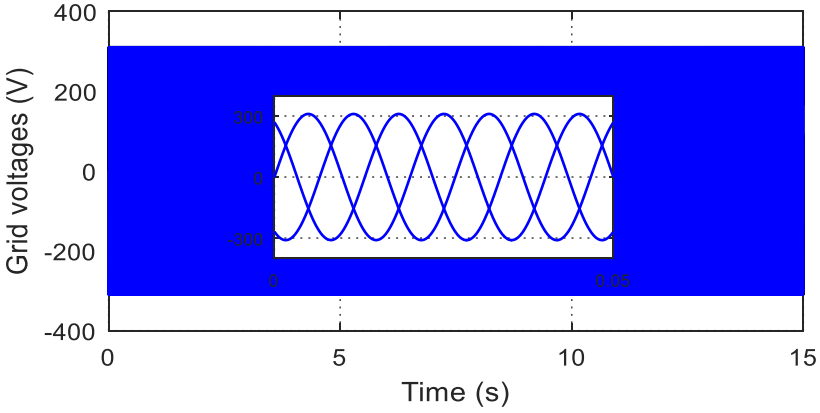

Figure 4. 22. Grid voltages.

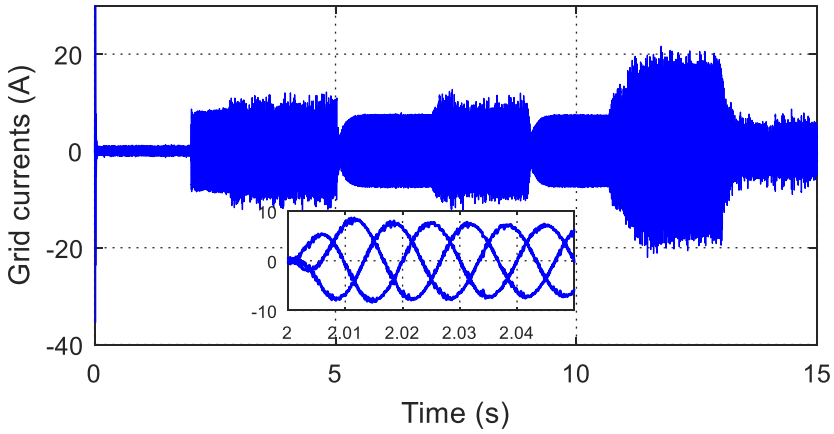

Figure 4. 23. Grid currents.

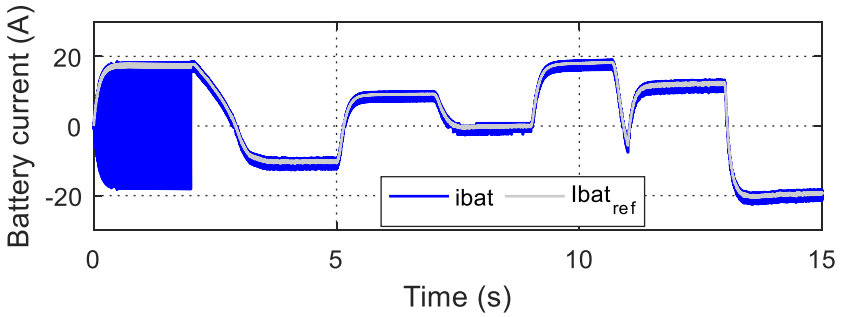

Figure 4. 24. Currents of battery storage.

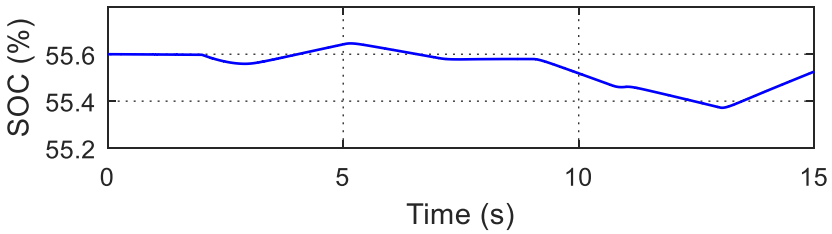

Figure 4. 25. SOC of battery.

i) Variable Wind Speed

Under this scenario, the wind speed is varying, but the load demand is constant. The wind speed is varied as a step change within a small period of 11 s. The wind output power rises and falls in proportion to the variable wind speed. The fluctuating power output affects the power balance between the generation and the load.

At the start t=(0 - 2)s, as the wind turbine and battery are disconnected, the grid matches the load demand perfectly. At t=(2 - 3)s, the battery is connected. Once the wind speed is sufficient to provide the power, the grid participation decreases continuously. At t=(3 - 5)s, the generation power is more than the load demand; the battery is consuming the excess

energy as SOC is lower than 90 % and hence starts charging (negative current flow to the battery). At t=(5 - 7)s, the generation is lower than the load demand; therefore, the required energy is supplied by the battery, as shown in Figure 4.24 (positive current), hence the SOC is falling down. At t=(7 - 9)s, the load demand is solely met by the wind power. Therefore, both the battery and the grid are inactive. At t=(9 - 11)s, the source is disconnected, hence the battery is supplying the energy as SOC is still higher than 30% to match the load demand.

ii) Variable load demand

Under this scenario, the AC load is varied with constant wind speed. At t=(11 - 13)s, the load demand is more than the maximum wind power extraction, therefore, the battery (discharging mode) and grid supplement the maximum wind power generation to provide the demanded power. At t=(13 - 15)s, the load demand is less than the wind power production; as a result, the battery is charged by the excess power provided by the wind (positive current).

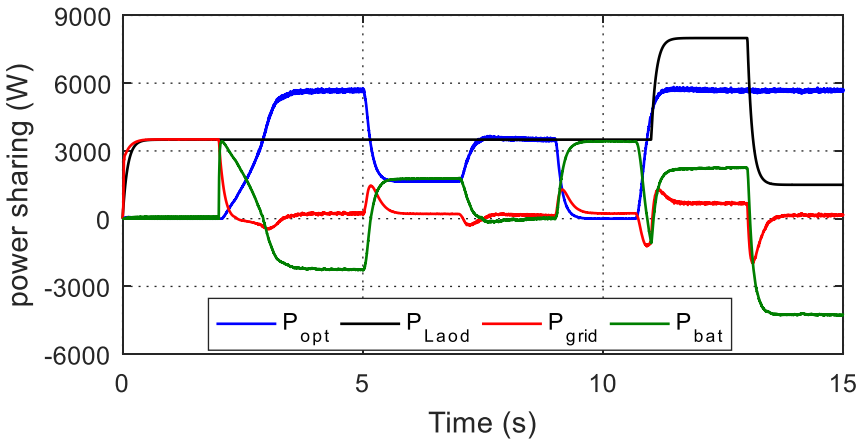

Figure 4. 26. Power-sharing of WECS.

Table 4. 4. Comparison performances at rated wind speed for the different controllers.

	PI	F-PI	AFLC-PI
Rising time (s)	0.028	0.019	0.015
Settling time (s)	0.036	0.022	0.018
Overshoot (%)	4.8	0	4.7
Steady-state error (%)	0	0	0

4.9 Conclusion

In this Chapter, the study is extended to the grid-connected wind system with BESS. Special focus is paid to the dynamic behavior and control of the grid side and BES systems.

The FMAPT algorithm based WECS developed in chapter three has been adapted to create and implement a grid-connected simulation model, to perform computer-based simulations. The vector control strategy for the GSC was studied. This control strategy enables one to fulfill the two main objectives of the GSC: control of the DC link voltage and control of the active and reactive powers exchanged bidirectionally between the PMSG and the grid. For the DC-link voltage regulation, the FL-based control has been developed to replace the conventional PI controller to assure a reliable tracking regardless the wind speed variation. Two FLC schemes have been proposed and simulated, namely a F-PI and an AFLC-PI controller. Thus, the designed control strategies are assumed to be simple in implementation, efficient and do not require the knowledge of the system parameters. These control schemes have been suggested to mitigate the effects of the system variability with convincing outcomes. Simulation results point out that the AFLC-PI scheme discloses an enhanced performance than the one with the traditional controller PI, enabling to enhance the transmission of power through the converter. The F-PI controller gives more elevated output energy and presents a good transient performance and insensitivity to wind fluctuations and load variation than when considering the PI and AFLC-PI.

The coordinated control strategy for a wind source along with the battery with its own dedicated DC-DC converter is proposed. The control strategy is designed for a wind source to balance the power flow to the load irrespective of fluctuating wind conditions and load demand. It has been shown that the proposed coordinated control strategy can provide several attractive features for a wind/battery system connected to the grid.

References

[1] M. Merai, M. W. Naouar, and I. Slama-Belkhodja, "An Improved DC-Link Voltage Control Strategy for Grid Connected Converters," *IEEE Transactions on Power Electronics*, vol. 33, no. 4, pp. 3575–3582, Apr. 2018.

[2] Asri, Y. Mihoub, S. Hassaine, P.-O. Logerais, and T. Allaoui, A. Amiar"An adaptive fuzzy proportional integral method for maximum power point tracking control of permanent magnet synchronous generator wind energy conversion system," 2018.

[3] A. Asri, Y. Mihoub, S. Hassaine, P.-O. Logerais, and T. Allaoui, "Intelligent maximum power tracking control of a PMSG wind energy conversion system," *Asian Journal of Control*, vol.21, pp. 1980-1990, Feb. 2019.

[4] B. Wu, Y. Lang, N. Zargari, and S. Kouro, *Power Conversion and Control of Wind Energy Systems*. John Wiley & Sons, 2011.

[5] S. Mondal, P. K. Gayen, and K. Gupta, "Study on Impact of LC-Filter Parameters Under Variable Loading Conditions of Three-Phase Voltage Source Inverter," in *2018 IEEE Electron Devices Kolkata Conference (EDKCON)*, 2018, pp. 132–136.

[6] B. Babes and L. Rahmani, "Commande prédictive de la machine synchrone à aimant permanent utilisée dans un système éolien," phd, Université Ferhat Abbas faculté de Technologie département d'électrotechnique, Sétif, 2018.

[7] G. Abad, J. Lopez, M. Rodriguez, L. Marroyo, and G. Iwanski, *Doubly fed induction machine: modeling and control for wind energy generation*, vol. 85. John Wiley & Sons, 2011.

[8] R. Esmaili, L. Xu, and D. K. Nichols, "A new control method of permanent magnet generator for maximum power tracking in wind turbine application," in *IEEE Power Engineering Society General Meeting*, 2005, pp. 2090-2095 Vol. 3.

[9] M. Chowdhury, "Modelling and control of direct drive variable speed wind turbine with Interior Permanent Magnet Synchronous Generator.," p. 221, 2014.

[10] Z. Roumila, D. Rekioua, T. Rekioua "Energy management based fuzzy logic controller of hybrid system wind/photovoltaic/diesel with storage battery", in International Journal of Hydrogen Energy, July 2017,Vol 42, p.19525-19535.

[11] M. Singh and A. Chandra, "Control of PMSG based variable speed wind-battery hybrid system in an isolated network," in *2009 IEEE Power Energy Society General Meeting*, 2009, pp. 1–6.

[12] D. Linden and T. Reddy, *Handbook of Batteries*. McGraw Hill Professional, 2001.

[13] B. Meghni, D. Dib, and A. T. Azar, "A second-order sliding mode and fuzzy logic control to optimal energy management in wind turbine with battery storage," *Neural Comput & Applic*, vol. 28, no. 6, pp. 1417–1434, Jun. 2017.

[14] R. Mittal, K. S. Sandhu, and D. K. Jain, "Battery energy storage system for variable speed driven PMSG for wind energy conversion system," in *2010 Joint International Conference on Power Electronics, Drives and Energy Systems 2010 Power India*, 2010, pp. 1–5.

[15] M. Yin, G. Li, M. Zhou, and C. Zhao, "Modeling of the Wind Turbine with a Permanent Magnet Synchronous Generator for Integration," in *2007 IEEE Power Engineering Society General Meeting*, 2007, pp. 1–6.

[16] R. Sarrias, L. M. Fernández, C. A. García, and F. Jurado, "Coordinate operation of power sources in a doubly-fed induction generator wind turbine/battery hybrid power system," *Journal of Power Sources*, vol. 205, pp. 354–366, 2012.

[17] R. Aissou, T. Rekioua, D. Rekioua, and A. Tounzi, "Application of nonlinear predictive control for charging the battery using wind energy with permanent magnet synchronous generator," *International journal of hydrogen energy*, vol. 41, no. 45, pp. 20964–20973, 2016.

[18] K. Ameur, A. Hadjaissa, A. Cheknane, and N. Essounbouli, "DC-Bus Voltage Control Based on Power Flow Management Using Direct Sliding Mode Control for Standalone Photovoltaic Systems," *Electric Power Components and Systems*, vol. 45, no. 10, pp. 1106–1117, Jun. 2017.

[19] I. M. Syed, B. Venkatesh, B. Wu, and A. B. Nassif, "Two-layer control scheme for a Supercapacitor Energy Storage System coupled to a Doubly Fed Induction Generator," *Electric Power Systems Research*, vol. 86, pp. 76–83, May 2012.

[20] M. Hussein, T. Senjyu, M. Orabi, M. Wahab, and M. Hamada, "Control of a Stand-Alone Variable Speed Wind Energy Supply System," *Applied Sciences*, vol. 3, no. 2, pp. 437–456, Apr. 2013.

[21] J. Dai, D. Xu, and B. Wu, "A Novel Control Scheme for Current-Source-Converter-Based PMSG Wind Energy Conversion Systems," *IEEE Transactions on Power Electronics*, vol. 24, no. 4, pp. 963–972, Apr. 2009.

[22] S. Yang, Q. Lei, F. Z. Peng, and Z. Qian, "A Robust Control Scheme for Grid-Connected Voltage-Source Inverters," *IEEE Transactions on Industrial Electronics*, vol. 58, no. 1, pp. 202–212, Jan. 2011.

[23] F. Blaabjerg, R. Teodorescu, M. Liserre, and A. V. Timbus, "Overview of control and grid synchronization for distributed power generation systems," *IEEE Transactions on industrial electronics*, vol. 53, no. 5, pp. 1398–1409, 2006.

[24] A. D. Hansen and G. Michalke, "Multi-pole permanent magnet synchronous generator wind turbines' grid support capability in uninterrupted operation during grid faults," *IET Renewable Power Generation*, vol. 3, no. 3, pp. 333–348, Sep. 2009.

[25] R. M. Linus and P. Damodharan, "Maximum power point tracking method using a modified perturb and observe algorithm for grid connected wind energy conversion systems," *IET Renewable Power Generation*, vol. 9, no. 6, pp. 682–689, Mar. 2015.

[26] S. Rajendran, U. Govindarajan, and D. S. P. Sankar, "Active and reactive power regulation in grid connected wind energy systems with permanent magnet synchronous generator and matrix converter," *IET Power Electronics*, vol. 7, no. 3, pp. 591–603, Sep. 2013.

[27] A.-R. Youssef, A. I. M. Ali, M. S. R. Saeed, and E. E. M. Mohamed, "Advanced multi-sector P&O maximum power point tracking technique for wind energy conversion system," *International Journal of Electrical Power & Energy Systems*, vol. 107, pp. 89–97, May 2019.

[28] I. H. Altaş, *Fuzzy Logic Control in Energy Systems with Design Applications in MATLAB®/Simulink®*. Institution of Engineering and Technology, 2017.

[29] B. K. Bose, "Expert system, fuzzy logic, and neural network applications in power electronics and motion control," *Proceedings of the IEEE*, vol. 82, no. 8, pp. 1303–1323, Aug. 1994.

[30] L. Reznik, O. Ghanayem, and A. Bourmistrov, "PID plus fuzzy controller structures as a design base for industrial applications," *Engineering Applications of Artificial Intelligence*, vol. 13, no. 4, pp. 419–430, Aug. 2000.

[31] M. Cheng; Q. Sun and E. Zhou, "New self-tuning fuzzy PI control of a novel doubly salient permanent-magnet motor drive," *IEEE Transactions on Industrial Electronics*, vol. 53, no. 3, pp. 814–821, Jun. 2006.

[32] W. Li, "Design of a hybrid fuzzy logic proportional plus conventional integral-derivative controller," *IEEE Transactions on Fuzzy Systems*, vol. 6, no. 4, pp. 449–463, Nov. 1998.

[33] M. M. Algazar, H. AL-monier, H. A. EL-halim, and M. E. E. K. Salem, "Maximum power point tracking using fuzzy logic control," *International Journal of Electrical Power & Energy Systems*, vol. 39, no. 1, pp. 21–28, Jul. 2012.

[34] N. J. Patil, R. H. Chile, and L. M. Waghmare, "a new approach to adaptive fuzzy pi controller using output scaling factor and reference models," *Mechatronic Systems and Control (formerly Control and Intelligent Systems) 2013*, vol. 41, no. 1, Jan. 2013.

[35] F. Kendouli, K. Abed, K. Nabti, H. Benalla, and B. Azoui, "High performance PWM converter control based PMSG for variable speed wind turbine," in *2012 First International Conference on Renewable Energies and Vehicular Technology*, 2012, pp. 502–507.

[36] N. K. Jena, K. B. Mohanty, H. Pradhan, and S. K. Sanyal, "A decoupled control strategy for a grid connected direct-drive PMSG based variable speed wind turbine system," in *2015 International Conference on Energy, Power and Environment: Towards Sustainable Growth (ICEPE)*, 2015, pp. 1–6.

I. Conclusions

In this thesis, two modes of operation have been considered: the isolated mode, and the grid-connected mode with BESS. In the isolated mode, a comprehensive analysis of various configurations and MPPT control schemes for PMSG based VSWT have been presented. The objective was to improve the power conversion efficiency. In a grid-connected mode, the GSC and BESS controls have been focused on. The motivation of developing a power management control strategy for a WECS along with a BESS was to improve the stability, the reliability, and the dynamic of the overall wind energy system.

Based on the assessment of the state-of-the-art in wind-turbine generators, power electronic converters, and energy storage technologies, it can be concluded that in terms of efficiency and reliability, the direct-drive PMSG system was found to be the best option. In particular, the direct-drive PMSG with diode rectifier was found to be currently the most preferred topology for small-scale WECS, due to the decrease in the number of switching devices, and therefore making both the size and the cost of the power conversion system smaller in comparison with the direct-drive PMSG with back to a back converter. The choice of this topology in this research is motivated also by its simplicity of control and high reliability.

A brief review of the energy storage technologies that are feasible for wind energy integration was also conducted. As a low-cost mature storage technology, offering satisfactory performance, lead-acid battery was selected for storage purposes.

The standalone WECS was briefly explained in order to highlight the contribution of the work. The proposed WECS is operated around the maximum power with two conventional MPPT namely TSR and ORB methods; the first is addressed to operate the wind turbine around the maximum power by regulating the rotational speed of the generator whereas, the second one is aimed to control the DC side rectifier. The MPPT can be achieved by adjusting the duty cycle in such a way that the optimal tip speed ratio λ_{opt} is maintained. A dual-loop control scheme with two PI controllers has been proposed in order to regulate the DC voltage and the generator speed under different wind speed conditions. The main aim of the MPPT algorithm is to track the optimum power point of the variable speed wind turbine. Choosing an appropriate MPPT technique is a tough task. In comparison, the TSR algorithm is very simple and fast. It permitted to acquire the maximum average value of C_p and maintained it at

its maximum even with changes in the wind speed. On the other hand, the ORB method is simple and cheaper, but it is less efficient in maximum wind power. The relationship of this method is difficult to calculate and can vary in real applications.

FLC application in WECS aims to operate the wind turbine around the maximum power by controlling the duty cycle of the DC-DC boost converter. The core interest of FLCs is their ability to incorporate experience, intuition and heuristics into the system instead of relying on mathematical models, making them more effective in power system applications where existing models are ill-defined and not reliable enough. Two MPPT control schemes have been modeled and simulated, namely FMAPT and FMEPT. It was shown that the MAPT controller has been employed to derive the optimum rotor speed corresponding to the best power point of the wind turbine based on the variations of measured aerodynamic power and rotor speed. While the FMEPT controller has been designed to track the derived optimum rectified voltage based on the variations of measured electrical DC power and rectified voltage. Hence achieves the maximum electrical energy from the wind generator. The simulation verifications were presented, and the proposed FMAPT and FMEPT were also compared to the conventional MPPT methods. The simulation results together with the comparison explicitly demonstrated that the proposed FMEPT and FMMPT provide the highest MPPT efficiencies as compared to the conventional control method. It was also deduced that the FMEPT and FMMPT not only provide very good responses to sudden variations in the wind speed, but also are simpler and lower-cost compared to the conventional ones because there is no need of an anemometer. The proposed FMAPT control strategy has a higher overall control efficiency and can be excellently used to more effectively extract the maximum wind energy.

A brief description of the complete structure of PMSG-based WECS including the energy storage system has been presented. The FMAPT algorithm based WECS has been adapted to create and implement a grid-connected simulation model. The grid side control strategy enables one to fulfill the two main objectives of the grid side converter: control of the DC bus voltage and maintaining the amplitude and frequency of the grid. For the DC-link voltage regulation, the FL-based control has been proposed to replace the conventional PI controller to ensure a reliable tracking regardless the wind speed variation and variable load demand. Two fuzzy control schemes have been developed, namely a F-PI and an AFLC-PI controller. Thus, the designed control strategies are assumed to be simple implementation,

efficient and do not require the knowledge of the system parameters. These control schemes have been suggested to mitigate the effects of the system variability with convincing outcomes. Simulation results point out that the AFLC-PI scheme discloses an enhanced performance than the one with the traditional controller PI enabling to enhance the transmission of power through the converter. The F-PI controller gives more elevated output energy and presents a good transient performance and insensitivity to wind fluctuations and load variation than when considering the PI and the AFLC-PI controllers.

The coordinated control strategy for a wind source along with the battery with its own dedicated DC-DC converter is proposed. The control strategy is designed for a wind source to balance the power flow to the load irrespective of fluctuating wind conditions and load demand. It has been shown that the proposed coordinated control strategy can provide several attractive features for a wind/battery system connected to the grid.

II. Recommendations for future work

The following future research works are suggested as an extension to the knowledge presented in this dissertation.

- **Hardware Implementation**

The present work focused on the implementation of efficient and robust control system for power management (extracted and delivered) by the wind hybrid system. To evaluate this work, the experimental results are necessary (with a test bench).

It is also suggested to implement these methods on several proposed wind turbines (small wind farm with high power), with optimization in untreated Points by others as: limiting the power in wind speeds or above par and controlling the AC/DC/AC converters.

- **Advanced Algorithms**

Development of other intelligent control strategies to enhance the performances of the WECS such as: advanced type 2 FLC, NN, Genetic algorithms, etc.

- **Sensorless control of the PMSG in the proposed WECS**

The MPPT control loop requires an anemometer to measure wind speed and a position sensor to measure the rotor speed. However, mechanical sensors increase the capital cost, as well as maintenance costs, and reduce the reliability of the turbine system. A sensorless control algorithm for the PMSG-WECS will bring great benefits to the system.

- **Unbalanced grid fault conditions**

Investigation of PMSG based WECS behavior under unbalanced grid fault conditions and development of new control strategies correspond to very interesting research direction to meet the emerging grid code requirement.

- **Battery storage**

Propose an efficient fuzzy power management algorithm to maintain supply-demand balance.

Explore a methodology to store excess wind power when the BESS is in a state of saturation, there would be more wind power and a decrease in the demand.

PMSG parameters

Rated Power	6 kW
Rated Torque	40 Nm
Rated Current	12 A
Rated Speed	153 rad/s
Number of the pairs of poles	5
Armature resistance	0.425 Ω
Stator dq-axis inductance	8.4 mH
Magnetic flux linkage	0.433 Wb
Friction coefficient	0.001189 N.m/s

Hybrid Wind/Battery system parameters

Rated power of wind turbine	8.5 kW
Maximum power at base wind speed p.u	0.8
Base rotational speed p.u	1
Base wind speed	12 m/s
Radius	3.24 m
Total inertia of the system (PMSG+WT)	0.01197 $kg.m^2$
Rated battery capacity	6.5 Ah
Nominal DC link voltage	200 V
Capacitor across boost converter input	840 µF
Capacitor across the DC link	3000 µF
Inductor for the boost converter	1 mH
Switching frequency of boost converter	10 kHz
Switching frequency of inverter	15 kHz
Filter inductance	20 mH
Filter resistance	1.15 Ω
Rated grid phase voltage	220 V